Design, Simulation and Fabrication of Photonic Crystal Slab Waveguide Based Polarization Processors

by

Khadijeh Bayat

A thesis
presented to the University of Waterloo
in fulfillment of the
thesis requirement for the degree of
Doctor of Philosophy
in
Electrical and Computer Engineering

Waterloo, Ontario, Canada, 2009

I hereby declare that I am the sole author of this thesis. This is a true copy of the thesis, including and required final revisions, as accepted by my examiners.

I understand that my thesis may be made electronically available to the public.

Abstract

The Photonic Crystal (PC) is a potential candidate for a compact optical integrated circuit on a solid state platform. The fabrication process of a PC is compatible with CMOS technology; thus, it could be potentially employed in hybrid optical and electrical integrated circuits.

One of the main obstacles in the implementation of an integrated optical circuit is the polarization dependence of wave propagation. Our goal is to overcome this obstacle by implementing PC based polarization controlling devices. One of the crucial elements of polarization controlling devices is the polarization rotator. The polarization rotator is utilized to manipulate and rotate the polarization of light.

In this thesis, we have proposed, designed and implemented an ultra-compact passive PC based polarization rotator. Passive polarization rotator structures are mostly composed of geometrically asymmetric structures. The polarization rotator structure consists of a single defect line PC slab waveguide. The geometrical asymmetry has been introduced on top of the defect line as an asymmetric loaded layer. The top loaded layer is asymmetric with respect to the z-axis propagation direction. To synchronize the power conversion and avoid power conversion reversal, the top loaded layer is alternated around the z-axis periodically. The structure is called periodic asymmetric loaded PC slab waveguide.

Due to the compactness of the proposed structure, a rigorous numerical method, 3D-FDTD can be employed to analyze and simulate the final designed structure. For the quick preliminary design, an analytical method that provides good approximate values of the structural parameters is preferred. Coupled-mode theory is a robust and well-known method for such analyses of perturbed waveguide structures. Thus, a coupled-mode theory based on semi-vectorial modes was developed for propagation modeling on square hole PC structures. In essence, we wish to develop a simple yet closed form method to carry out the initial design of the device of interest. In the next step, we refined the design by using rigorous but numerically expensive 3D-FDTD simulations. We believe this approach leads to optimization of the device parameters easily, if desired.

To extend the design to a more general shape PC based polarization rotator, a design methodology based on hybrid modes of asymmetric loaded PC slab waveguide

was introduced. The hybrid modes of the structure were calculated utilizing the 3D-FDTD method combined with the Spatial Fourier Transform (SFT). The propagation constants and profile of the slow and fast modes of an asymmetric loaded PC slab waveguide were extracted from the 3D-FDTD simulation results. The half-beat length, which is the length of each loaded layer, and total number of the loaded layers are calculated using the aforementioned data. This method provides the exact values of the polarization rotator structure's parameter.

The square hole PC based polarization rotator was designed employing both coupled-mode theory and normal modal analysis for THz frequency applications. Both design methods led to the same results. The design was verified by the 3D-FDTD simulation of the polarization rotator structure. For a square hole PC polarization rotator, a polarization conversion efficiency higher than 90% over the propagation distance of 12 λ was achieved within the frequency band of 586.4-604.5 GHz corresponding to the normalized frequency of 0.258-0.267.

The design was extended to a circular hole PC based polarization rotator. A polarization conversion efficiency higher than 75% was achieved within the frequency band of 600-604.5 GHz. The circular hole PC polarization rotator is more compact than the square-hole PC structure. On the other hand, the circular hole PC polarization rotator is narrow band in comparison with the square hole PC polarization rotator. In a circular hole PC slab structure, the Bloch modes (fast and slow modes) couple energy to the TM-like PC slab modes. In both square and circular hole PC slab structures with finite number of rows, and the TM-like PC slab modes are extended to the lower edge of the bandgap. In bandgap calculation using PWEM, it is assumed that the PC structure is extended to infinity, however in practice the number of rows is limited, which is the source of discrepancy between the bandgap calculation using PWEM and 3D-FDTD. In an asymmetric loaded circular hole PC slab waveguide, the leaky TM-like PC slab modes are extended deep inside the bandgap and overlapped with both the slow and fast Bloch modes; whereas, in an asymmetric loaded square hole PC slab waveguide, the leaky TM-like PC slab modes are below the frequency band of slow and fast modes. Therefore, TM-like PC slab modes have significantly more adverse effect on the performance of the circular-hole based polarization rotator leading to a narrow band structure.

SOI based PC membrane technology for THz application was developed. The device layer is made of highly resistive silicon to maintain low loss propagation for THz wave. The PC slab waveguide and polarization rotators were fabricated employing this technology.

Finally, an a-SiON PC slab waveguide structures were also fabricated at low temperature for optical applications. This technology has the potential to be implemented on any substrate or CMOS chips.

Index Terms: Photonic crystal, Polarization rotator, Silicon-on-Insulator (SOI), Finite-Difference Time Domain (FDTD) method, polarization, Photonic crystal slab waveguide, coupled-mode theory, low temperature, amorphous silicon, amorphous silicon oxinitride, integrated optics, nanophotonics, fabrication, nano-fabrication, Terahertz, THz waveguide.

Acknowledgements

I would like to express my sincere appreciation and deepest gratitude to my supervisors Professor Sujeet K. Chaudhuri and Professor Ali Safavi-Naeini for their generosity in their time, knowledge and experience during our valuable discussions. I am also very thankful for their encouragement, support, and guidance during the course of my study.

I would like also to thank my committee members for their valuable time: Prof. Marko Loncar, Prof. Dayan Ban, Prof. Hamed Majedi, and Prof. Mustafa Yavuz.

Financial support during this study was provided by the Natural Science and Engineering Research Council of Canada (NSERC) and Research in Motion (RIM). Their contribution is greatly appreciated.

Many thanks to IIRPG and G2N group members for their help and support and friendship they offered. I will always carry the great memories which I have made with my friend and colleagues such as Leila Yousefi, Mina Askari, Masoumeh Roadafshani, Mona Mojdeh, Mohaddesseh Azimlu, Dr. Maryam Moradi, Bahareh Sadegh-Makki, Nasim Paryab, Marzieh Rezaee, Farhad Riazi, Fariborz Rahimi, Babak Alavi-kia, Mohammad Neshat, George Shaker, Dr. Mohammad Fakharzadeh, Dr. Majid Gharghi, Dr. Mohammad Esmaeili-Rad and Dr. Daryoosh Saeedkia. I am really grateful to Richard Barber for his support and help. Also, I would like to thank Mark Fisher for teaching me how to work with the equipment and his valuable technical support during my work in NFC at the University of Minnesota.

I would like to extend my greatest appreciation and thanks to my mother, Maryam Ghasemi, and my father, Kheirolah Bayat, for their endless love, support, sacrifice and patient. I will never forget their kindness and support. Also, my extended thanks go to my siblings for their love, support and friendship. Last but not the least, I would like to thank my love and my husband, Mahdi Farrokh Baroughi for his collaboration, enthusiasm and support. I am really grateful for his insightful discussions, support and help. This work is dedicated to my parents and my husband.

Dedication

To my devoted parents

and to my husband

Contents

List of Tables

List of Figures

Chapter 1

Introduction

Integration of all photonic components on a single solid state platform has long been a main issue for optical community [1-10]. One of the most promising techniques for optical integrated circuit is the Photonic Crystal (PC) technology. It is worth mentioning that emerging compatible PC technology with Complementary Metal-Oxide Semiconductor (CMOS) technology has paved the way for implementation of an integrated hybrid optics and electronic circuit [11-12]. Using PC, compact optical elements can be implemented on a solid state platform. The bottleneck of this technology and in general optical integrated circuit is the strong polarization dependence of wave propagation [13-16]. Thus, the performance and optical characteristics of the integrated circuit elements is polarization independent. The main topic of this thesis is to provide solutions to the polarization sensitivity of a PC integrated photonic circuit by proposing PC based polarization controlling devices.

1.1 Motivations

Our goal is to overcome the polarization sensitivity of PC integrated circuit by introducing integrated PC based polarization controlling devices that are capable of controlling and manipulating of the polarization of the propagating wave. The most crucial polarization controlling device in an optical integrated circuit is the polarization rotator [17-20]. The focus of this thesis is to propose, design and fabricate a PC based polarization rotator. The objective of this thesis is to take advantage of the strong guiding

characteristics and the compactness of a PC slab structure to implement an ultra-compact polarization rotator. Thus, the polarization of the input signal can be manipulated and adjusted to the desired one. This is the main goal of the proposed thesis. To accomplish this goal, we have not only introduced and designed a novel device using rigorous analytical and numerical methods, but also developed new technologies that have led us toward integrated optical and electronic circuits. Since, this is a multidisciplinary project that deals with theory, material and technology development; the objectives of this thesis are categorized accordingly. Generally speaking, this project consists of two phases including theory and fabrication.

The first phase consists of studying the PC structures thoroughly using rigorous electromagnetic numerical methods. Most of the conducted studies on the PC slab waveguide structures use a two-dimensional analysis employing effective index method in vertical direction. There is an issue that the polarization dependent guiding of a PC slab waveguide structure strongly depends on the structure thickness that is overlooked in the 2D analysis. To compensate, we have conducted a thorough study using 3D Plane Wave Expansion Method (PWEM) and 3D Finite-Difference Time Domain (3D-FDTD) method on the thickness dependency of the guiding characteristics of a PC slab waveguide. We proposed a design methodology for polarization selective PC slab waveguide structure that is very useful for the design of the polarization controlling devices.

In continuation to the first phase of the thesis, a new PC based polarization rotator structure was proposed. The passive polarization rotator structures rely on the geometrical asymmetry of the structure such as a slanted waveguide polarization rotator [19-21]. We have introduced a periodic asymmetric loaded PC slab waveguide based polarization rotator that is several wavelengths long. To design and analyze the structure, rigorous analytical and numerical methods are employed as opposed to the previous polarization rotator structures that can not be analyzed using these methods due to their huge sizes.

The second phase of the project consisted of two-folds that included material development and fabrication. The PC structures usually are implemented on a silicon-on-insulator (SOI) wafer [22-25]. Even though the process fabrication of SOI based PC

structures is compatible with CMOS technology, the integration of the PC circuit with CMOS technology requires many changes and adjustments, which is not cost effective or practical [26-32]. More importantly, a very small percentage of CMOS Integrated Circuits (ICs) are implemented on SOI substrate that makes the integration even more challenging. As a part of this thesis, our goal is to introduce a new technique that is cost effective and does not require any change or adjustment to the existing CMOS technology. Having said that, we developed and introduced a low temperature a-SiON based PC technology that could be implemented on top of any CMOS circuit.

Finally, we have extended the fabrication process to cover the THz frequency band by developing a novel Si based PC membrane technology. Intrinsic silicon is a low loss medium for the THz wave, making Si based PC slab waveguides good candidates for THz waveguide structures [33]. The recent advances in THz generation and detection, has the trend leaning towards integrating THz sources, detectors and all other intermediate components on a single chip [34-36]. This makes the PC a promising technology for these applications [37]. We developed a low loss integrated PC membrane technology. Waveguides, resonators and polarization rotator structures were fabricated in this technology.

1.2 Organization of the Thesis

This thesis is organized as follows:

Chapter 2 gives an overview on analysis and design of the PC structures including the analysis and simulation methods used. Included in this chapter is a literature review on polarization rotators.

Chapter 3 provides with a thorough study on the guiding mechanisms in a PC slab waveguide structures using 3D-FDTD and PWEM. The design methodology for polarization selective PC slab waveguide is presented here.

In chapter 4, a periodic asymmetric loaded PC slab waveguide is introduced for polarization rotation application. The design methodology is two-folded. The first part, involves the optimization of the asymmetric loaded PC slab structure using PWEM to provide the maximum overlap between x-polarized and y-polarized waves. While the

second part, is to design a periodic asymmetric loaded PC slab waveguide using the coupled mode theory. A coupled mode theory based on the semi-vectorial modes is developed for the square hole PC structure. The design is verified and refined using 3D-FDTD. Another design methodology is developed based on the hybrid modes. The vector-propagation characteristics of the hybrid modes are calculated employing 3D-FDTD combined with Spatial Fourier Transform (SFT). The design is extended to the circular hole PC structure. Circular and square hole PC based polarization rotators are then compared in terms of loss characteristics and bandwidth.

In chapter 5, the SiON based CMOS compatible PC technology is presented. The first part of the chapter deals with the material development. The low temperature SiON material system is developed using Plasma Enhanced Chemical Vapor Deposition (PECVD). The refractive indices and chemical compositions of the layers are measured using ellipsometry and Rutherford Back Scattering (RBS) methods. By adding a-Si to the developed material system, a wide range of refractive indices has been achieved. The PC slab waveguide structures are fabricated on glass substrate in the optical frequency bands.

The fabrication process of the SOI based PC structure in THz frequency band is presented. Moreover, the fabrication technique for the periodic asymmetric loaded PC slab waveguide as polarization rotator is discussed and the Scanning Electron Microscopy (SEM) of the fabricated samples are presented.

Finally, we draw conclusions and present topics for future research in Chapter 6.

Chapter 2

Background

2.1 Introduction

Photonic Crystal (PC) has attracted a lot of attention in the last couple of decades, and was proposed as material that could localize light and inhibit spontaneous emission [38]. They are formed by creating a periodic variation in the dielectric constant on a scale that is comparable to the operating wavelength of interest. Due to this periodicity there are frequency bands over which the propagation of the light in certain directions is forbidden. These frequency bands are called the stop bands or the Photonic Band Gap (PBG).

PCs are classified into three categories, one dimensional, two-dimensional and three-dimensional crystals. Fabricating the 3D PC is difficult; although, various technologies have been developed to fabricate 3D PCs in recent years [39-44]. A 3D PC has three dimensional band gaps where no electromagnetic propagation exists in any direction.

An alternative system for the PCs is the photonic crystal slab [45], shown in Figure 2.1. PC slabs are usually fabricated on a substrate made of a semiconductor or an insulator. Their fabrication process is much easier than that of 3D PCs [22-25]. In practice, PC slabs are more of interest. A PC slab has only 2D periodicity and uses index-guiding to confine light in the third dimension (*z*-direction in Figure 2.1) [22]. The smallest unit of the periodicity is called a unit cell and the length of the spatial period that is called a lattice constant is depicted by '*a*' in Figure 2.1. PC slabs approximate many of the properties of a true photonic crystal. Optical components with the size of at least one order of magnitude less than the conventional devices can potentially be realized by employing PC slab.

Figure 2.1 Photonic crystal slab with triangular lattice of holes in dielectric slab [14]

In this chapter, first a brief review on the analysis methods of the PC structures is presented. Section 2.2 introduces various methods for 2D PC and PC slab structure analysis including PWEM and Finite-Difference Time Domain (FDTD) method. In section 2.3, PC slab waveguides are introduced, the guiding mechanism and the important parameters of the PC slab waveguide are assessed. Section 2.4 surveys the polarization dependency behavior of the 2D PC and the PC slab. Finally, a review on the passive polarization rotator structures is given and possible configurations for a PC based polarization rotator are discussed.

2.2 Analysis of PC structures

To study the PC structure, frequency and time-domain methods are utilized in a complementary way. The most dominant frequency domain analysis method is the Plane-Wave Expansion Method (PWEM) based on the time-harmonic decomposition of the eigenmodes and the dielectric constant. In PWEM, it is assumed that the structure is periodic in all directions and the periodicity is extended to infinity [46-47]. Short range disorders or defects can be handled in PWEM, but, PWEM is not applicable to structures with long range distortion, or quasi-periodic structures. On the other hand, FDTD method can be used for any structure, and there is no restriction except for the required computational resources. In the following subsections, PWEM and FDTD are explained.

2.2.1 Plane wave expansion method for modal analysis of PCs

The most common frequency domain analysis of PC structures is PWEM. The output of a PWEM analysis is the band structure or band diagram that is the plot of the normalized frequency, a/λ, where a is the lattice constant and λ is the free space wavelength of the guided modes versus the wave vector. Here, the PWEM is described for a 2D PC and a 2D PC slab structures.

2.2.1.1 PWEM for 2D PC

For a 2D PC where no variation in the dielectric constant of the vertical direction exists, this leads to $\partial/\partial z = 0$. Therefore, $\vec{k}$, wave vector, does not have any component in the vertical z direction, in the structure shown in Figure 2.1. By applying these assumptions to the Maxwell's equation, the Maxwell's equations can be written in terms of only E_z or H_z components as the follows [48]:

$$-\frac{1}{\varepsilon(r)}\left\{\frac{\partial^2}{\partial x^2}+\frac{\partial^2}{\partial y^2}\right\}\vec{E}_z(r)=\frac{\omega^2}{c^2}\vec{E}_z(r) \qquad (2.1.a)$$

$$\left\{\frac{\partial}{\partial x}\frac{1}{\varepsilon(r)}\frac{\partial}{\partial x}+\frac{\partial}{\partial y}\frac{1}{\varepsilon(r)}\frac{\partial}{\partial y}\right\}\vec{H}_z(r)=\frac{\omega^2}{c^2}\vec{H}_z(r) \qquad (2.1.b)$$

Where:

$$\vec{r} = x\hat{a}_x + y\hat{a}_y \qquad (2.1.c)$$

These two equations represent two independent polarizations, one is the *H* or TM polarization where the magnetic field is parallel to the *z* axis, and the other one is called the *E* or TE polarization where the electric field is parallel to the *z* axis.

Assuming that the PC is an infinite periodic structure, according to the Bloch theory the periodicity of the medium manifests itself in the modes. Thus, the modes of such structures are periodic. Any periodic wave can be Fourier expanded. In Eq. (2.1.a), $1/\varepsilon(\vec{r})$ is also periodic. Therefore, $1/\varepsilon(\vec{r})$ can be Fourier expanded. Substituting the Fourier expansion of the electric fields and $1/\varepsilon(\vec{r})$ in Eq. (2.1.a) results to an eigenvalue equation in which the eigenfunctions are the modes of the structure and the eigenvalues are the corresponding propagation constants. In the following paragraph the mathematical details of finding the eigenvalue equation are given.

$\varepsilon(\vec{r})$ is periodic in the 2D PC, so is $1/\varepsilon(\vec{r})$, because of the periodicity in the *x*-*y* plane, the inverse dielectric function can be Fourier expanded in the form of [48]:

$$\frac{1}{\varepsilon(r)} = \sum_G \kappa_G \exp(j\vec{G}.\vec{r}),\ \kappa_G = \frac{1}{A}\iint_S \frac{1}{\varepsilon(r)}\exp(-j\vec{G}.\vec{r})dS \qquad (2.2)$$

Where *S* and *A* are the unit cell and the area of the unit cell respectively. $\vec{G}$ is called the reciprocal lattice vector (Fourier spatial frequencies) and is defined so to meet the following condition:

$$\exp(j\vec{G}.\vec{a}) = 1 \qquad (2.3)$$

Where $\vec{a}$ is the unit cell vector defined in section 2.2.1. From Eq. (2.2) we note that the reciprocal lattice vector is the Fourier transform variable of the unit cell. For a square lattice, $\vec{G}$ is given by:

$$\vec{G} = g_1\hat{x} + g_2\hat{y} = \frac{2\pi m}{a}\hat{x} + \frac{2\pi n}{a}\hat{y} \qquad (2.4.a)$$

And $\vec{a}$ for a 2D PC square lattice is given by:

$$\vec{a} = a\hat{x} + a\hat{y} \qquad (2.4.b)$$

The primitive reciprocal lattice is defined by setting *n=m=1*. Figures 2.2(a) and (b) show the reciprocal lattice for a 2D square and triangular lattice, respectively [48]. For a square lattice with the lattice vector of $a_1 = a\hat{x}$ and $a_2 = a\hat{y}$, the primitive reciprocal lattice vectors are given by: $b_1 = \frac{2\pi}{a}\hat{x}$ and $b_2 = \frac{2\pi}{a}\hat{y}$. For a triangular lattice where the lattice vectors are $a(\hat{y} + \hat{x}\sqrt{3})/2$ and $a(\hat{y} - \hat{x}\sqrt{3})/2$, the primitive reciprocal lattice vectors are: $(2\pi/a)(\hat{y} + \hat{x}\sqrt{3})/2$ and $(2\pi/a)(\hat{y} - \hat{x}\sqrt{3})/2$.

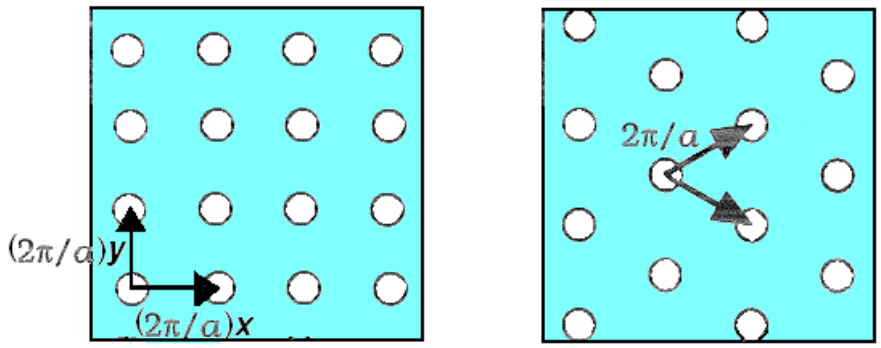

(a) (b)

Figure 2.2 The reciprocal lattice of (a) the square (b) the triangular lattice 2D PC [48].

In an infinite periodic photonic crystal, according to Bloch's theorem which is equivalent to the Floquet theorem [45], $\vec{H}_z$ and $\vec{E}_z$ can be expanded as a sum of the infinite number of the plane waves [48]:

$$\vec{H}_z(\vec{r}) = \sum_G h_{G,k} \exp(i(\vec{k} + \vec{G}).\vec{r}) = \exp(i\vec{k}.\vec{r}) \sum_G h_{G,k} \exp(i\vec{G}.\vec{r}) = \exp(i\vec{k}.\vec{r}) u_k(\vec{r}) \tag{2.5}$$

$$\vec{E}_z(\vec{r}) = \sum_G e_{G,k} \exp(i(\vec{k} + \vec{G}).\vec{r}) = \exp(i\vec{k}.\vec{r}) \sum_G e_{G,k} \exp(i\vec{G}.\vec{r}) = \exp(i\vec{k}.\vec{r}) v_k(\vec{r}) \tag{2.6}$$

Where $\vec{k}$ is the wave vector of the plane wave, these modes are called "Bloch modes", consisting of a plane wave multiplied by a periodic function, which follows the periodicity of the lattice as the follows [45]:

$$u_k(\vec{r}) = u_k(\vec{r} + \vec{a})$$
$$v_k(\vec{r}) = v_k(\vec{r} + \vec{a}) \qquad (2.7)$$

By substituting Eqs. (2.1), (2.5) and (2.6) into the Eqs. (2.1.a) and (2.1.b), the following eigenvalue equations are obtained [45]:

$$-\sum_{G'} \kappa_G(\vec{G} - \vec{G}')(\vec{k} + \vec{G}') \times \left\{(\vec{k} + \vec{G}') \times \vec{E}_{z,kn}(\vec{G}')\right\} = \frac{\omega_{kn}^2}{c^2} \vec{E}_{z,kn}(\vec{G}) \qquad (2.8)$$

$$-\sum_{G'} \kappa_G(\vec{G} - \vec{G}')(\vec{k} + \vec{G}') \times \left\{(\vec{k} + \vec{G}') \times \vec{H}_{z,kn}(\vec{G}')\right\} = \frac{\omega_{kn}^2}{c^2} \vec{H}_{z,kn}(\vec{G}) \qquad (2.9)$$

Where ω_{kn} denotes the eigen-frequency of $\vec{E}_{z,kn}(r)$ and $\vec{H}_{z,kn}(r)$. Equations (2.8) and (2.9) have an infinite number of eigenvalues and eigenfunctions, which are distinguished by subscript *n*. By solving one of these two sets of equations, the photonic band structure can be obtained. In solving the eigenvalue equations, the summation is truncated at a large number,*N,* of $\vec{G}'$, and the eigenvalue problem for a given $\vec{k}$ is solved. In order to improve the convergence, *N* must be a large number.

To solve this system, we restrict *k* values to a limited interval called the first Brillouin zone. To define the first Brillouin zone let's look at the Bloch modes introduced by Eq. (2.5) or (2.6). By looking at these equations, it is obvious that a mode with a wave vector of $\vec{k}$ and a mode with a wave vector of $\vec{k} + \vec{G}$ are the same modes. Therefore, *k* can be restricted to the first reciprocal lattice in which all values of *k* are less than *G*. This zone is called the first Brillouin zone, *[-π/a, π/a]*. Figures 2.3(a) and 2.3(b) show the first Brillouin zone for the 2D PC square and triangular lattices, respectively. There are highly symmetric points in the first Brillouin zone. For example, square lattice points are defined by: the *Γ* point, *(0,0)*, the *X* point, *(π/a ,0)* and the *M* point *(π/a, π/a)*. Therefore, to calculate the band structure, *k* moves from the *Γ* point to the *X* point and from the *X* point to the *M* point and then moves back toward the *Γ* point. This path covers all the possible *k* values in the first Brillouin zone.

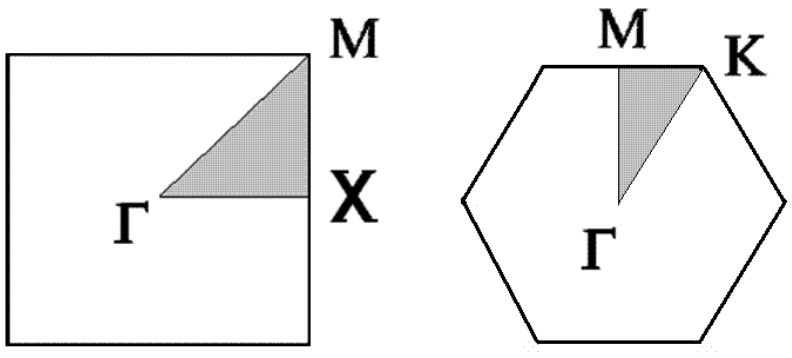

(a) (b)

Figure 2.3 (a) The first Brilluion zone for (a) a square (b) a triangular based 2D PC [48].

The PWEM is a well-known method for the band structure calculation. Here, the band structure of a 2D triangular PC is presented. Figure 2.4 shows the band structure for the 2D triangular PC with $r/a=0.48$, $\varepsilon_r=13$, for both TE and TM polarizations. The substrate is a high dielectric material. The TE polarization for a 2D PC structure where (x,y) is the planar PC surface is defined by the following components: E_z, H_x and H_y. The TM polarization for the same structure is defined by the following components: H_z, E_x and E_y. While a wide band gap is observed for TM polarization, no band gap exists for TE polarization. The band gap lies within the normalized frequency band, a/λ, of 0.43 to 0.52.

One of the important parameters of a 2D PC is the ratio of the radius of the hole and the lattice constant, r/a. To assess the importance of this parameter, the crystal's gap map for both polarizations is constructed from GaAs with $\varepsilon_r=11.4$ and is shown in Figure 2.5. Gap map graphs bandgap versus frequency. This figure shows that the PBG increase with r/a.

For the TE polarization, several thin gaps may be noted. For large hole sizes, an overlap between the PBG of the two polarizations is observed which can be useful for some applications. Noticing that, by using a triangular lattice with large air holes, a complete band gap for both TE and TM polarizations can be achieved.

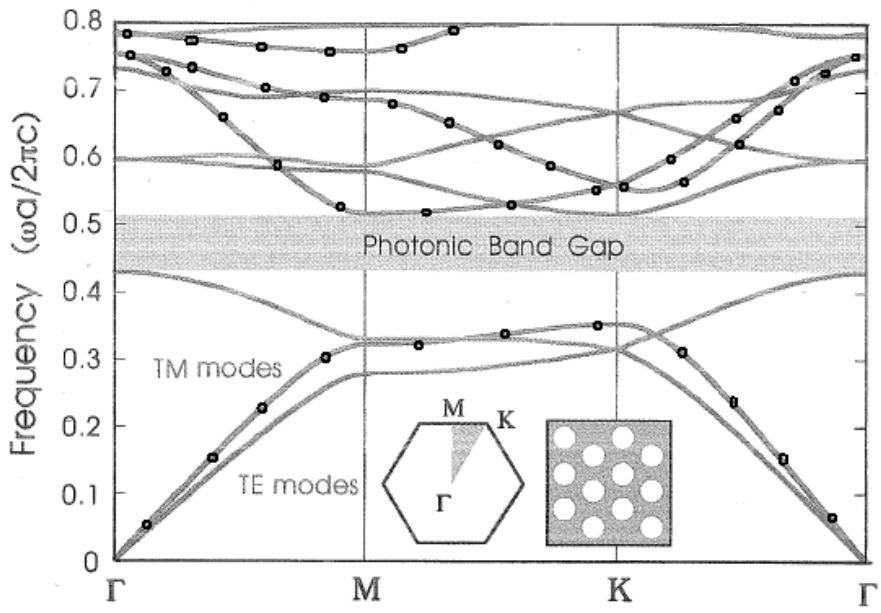

Figure 2.4 The band diagram of the triangualr air columns drilled inside a high dielectric material $\varepsilon_r=13$ for TE/TM polarization [48].

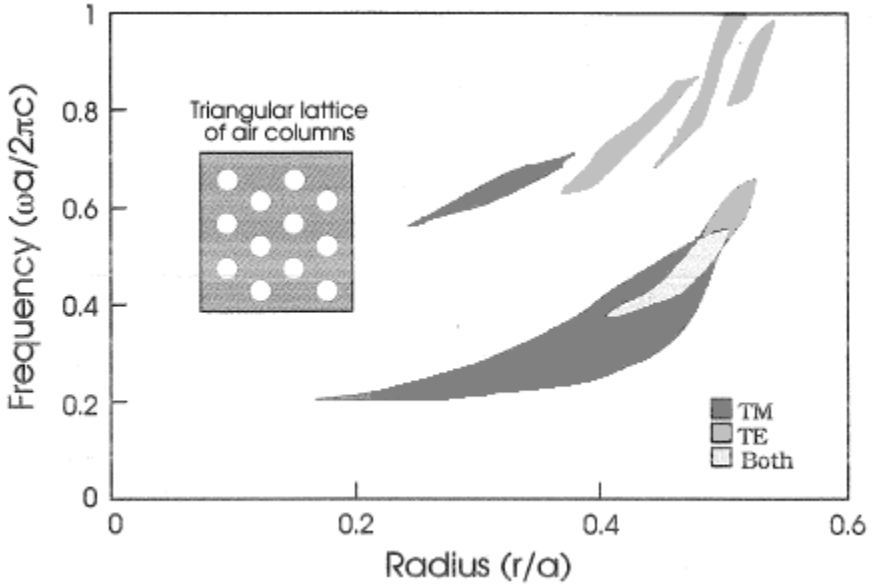

Figure 2.5 Gap map for triangular lattice of air holes inside GaAs, $\varepsilon_r=11.4$ [48].

It is useful for some applications to have a 2D PC that has an overlapping band gap for both polarizations and is easy to fabricate. The gap maps for different kinds of PCs show that the overlap occurs only with triangular lattice when $r=0.475a$. Thus, this

structure has very thin dielectric veins of a *0.05a* width between the air columns. Fabricating such a structure with a band gap at λ=1.5 μm would require a feature size of 0.035 μm, which would be very difficult to achieve Therefore it is quite challenging to achieve a complete band gap employing a 2D PC.

2.2.1.2 PWEM for PC slab

In practice, the third dimension of the 2D PC is not infinite, therefore, 3D analysis is required. In this section, the PWEM has been extended for the PC slab structure. Inclusion of the third dimension makes the band structure calculation more complicated. In order to be able to employ the PWEM, the structure must be periodic in all dimensions, but the PC slab has only a two-dimensional periodicity. To employ the three-dimensional PWEM, we can impose a third (vertical) dimensional periodicity by introducing a periodic sequence of slabs separated by a sufficient amount of air as a background region to ensure electromagnetic isolation. This is called the super-cell technique [49-50]. For example, the super-cell for a triangular PC slab is shown in Figure 2.6. The guided modes are localized within the PC slab; therefore, changing the vertical (out-of-plane) period of the slabs beyond a sufficiently large separation will not change the guided eigen-modes. As a result, the guided modes can be determined by conventional PWEM with the super-cell technique, however, the leaky modes, which lie above the light line, are extended infinitely in the cladding region outside the slab. Thus, the conventional PWEM is not appropriate. To overcome this drawback, the concept of Perfectly Matched Layers (PMLs) has been applied in the vertical direction to absorb the radiation from the slab [51].

In the following derivation, a periodic boundary condition is applied in all directions. To drive the PWEM formulation for the PC slab, the Fourier expansion of the inverse function of dielectric constant is calculated. Having imposed periodicity in all direction, the inverse dielectric function can be expanded in the form of [51]:

$$\frac{1}{\varepsilon(r)} = \sum_{G} \kappa_G \exp(i\vec{G}.\vec{r}) \qquad (2.10)$$

Where κ_G is the Fourier coefficients given by [51]:

$$\kappa_G = \frac{1}{V}\int_V \frac{1}{\varepsilon(r)}\exp(-i\vec{G}.\vec{r})dv \qquad (2.11)$$

Where V is the volume of the unit cell. $\vec{G} = m_1\vec{g}_1 + m_2\vec{g}_2 + m_3\vec{g}_3$ is the reciprocal lattice vector. The first Brillouin zone for triangular PC slab is shown in Figure 2.7. In the in-plane direction, the reciprocal lattice looks like the reciprocal lattice of the 2D triangular PC.

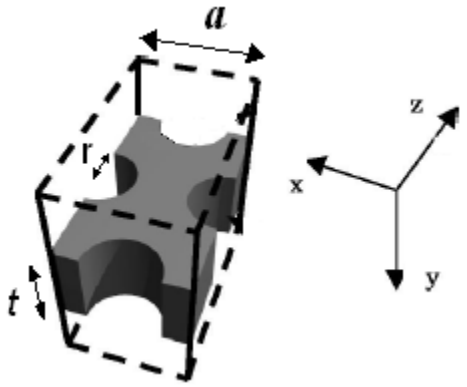

Figure 2.6 The super-cell for triangular PC slab [47].

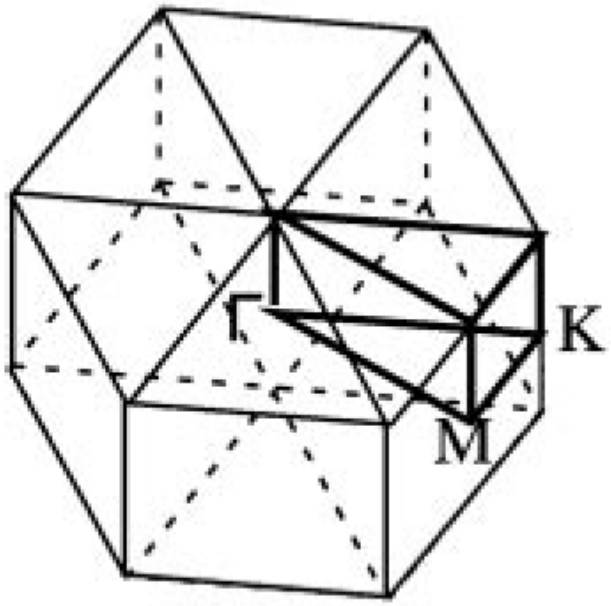

Figure 2.7 The first Brillouin zone of triangular based PC slab [48]

For 3D analysis, the following eigenvalue equation for $\vec{H}$ is used:

$$\nabla \times \left\{ \frac{1}{\varepsilon(r)} \nabla \times \vec{H}(r) \right\} = \frac{\omega^2}{c^2} \vec{H}(r) \tag{2.12}$$

Again, because of the periodicity of the structure, the Bloch modes can be expressed as:

$$\vec{H}(r) = \sum_G h_{G,k} \exp(i(\vec{k} + \vec{G}).\vec{r}) = u_k(r) \exp(i\vec{k}.\vec{r}) \tag{2.13}$$

Substituting (2.10) and (2.13) into (2.12) leads to the following eigenvalue equation:

$$-\sum_{G'} \kappa(\vec{G} - \vec{G}')(\vec{k} + \vec{G}') \times \left\{ (\vec{k} + \vec{G}') \times \vec{H}_{kn}(\vec{G}') \right\} = \frac{\omega_{kn}^2}{c^2} \vec{H}_{kn}(\vec{G}) \tag{2.14}$$

Where ω_{kn} denotes the eigenfrequency of $\vec{H}_{kn}(r)$. By solving above equation, the photonic band structure can be calculated. In order to simplify the equation (2.14), given Faraday's equation, $\vec{H}_{kn}(r)$ is perpendicular to $\vec{k} + \vec{G}$, so it can be expressed as the combination of two orthogonal vectors, $\hat{e}_{G1}$ and $\hat{e}_{G2}$:

$$\vec{H}_{kn}(\vec{G}) = h_{kn}^{G1} \hat{e}_{G1} + h_{kn}^{G2} \hat{e}_{G2} \tag{2.15}$$

$\left\{ \hat{e}_{G1}, \hat{e}_{G2}, \vec{k} + \vec{G} \right\}$ are perpendicular to each other. Then, the following equation can be derived from equation (2.14) [51]:

$$\sum_{G'} \left| \vec{k} + \vec{G} \right\| \vec{k} + \vec{G}' \left| \kappa(\vec{G} - \vec{G}') \begin{bmatrix} \hat{e}_{G2}.\hat{e}_{G_2'} & -\hat{e}_{G2}.\hat{e}_{G_1'} \\ -\hat{e}_{G1}.\hat{e}_{G'2} & \hat{e}_{G1}.\hat{e}_{G_1'} \end{bmatrix} \begin{bmatrix} h_{kn}^{G'1} \\ h_{kn}^{G'2} \end{bmatrix} = \frac{\omega^2}{c^2} \begin{bmatrix} h_{kn}^{G1} \\ h_{kn}^{G2} \end{bmatrix} \right. \tag{2.16}$$

This is a standard eigenvalue problem and can be solved using numerical methods. For example, the band structure of the triangular PC slab which is suspended in air with *r/a=0.3*, ε_r*=11.56, t=0.6a* is illustrated in Figure 2.8 for TM-like polarization. The base material is silicon. For the structure shown in Figure 2.6, the TM-like mode is defined by H_y, E_z and E_x components. The TE-like mode is defined by E_y, H_z and H_x components. By changing the type of the mirror symmetry of the axial component with respect to the in-

plane, even (TE-like) or odd (TM-like) eigen modes of the PC has been selected. No band gap is observed for TE-like modes.

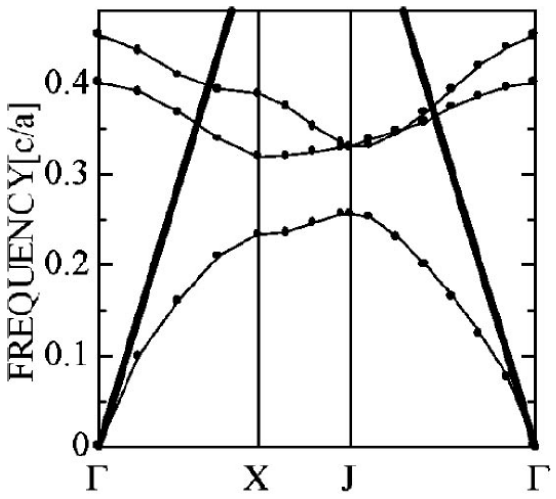

Figure 2.8 Band diagrams for TM-like modes of a triangular lattice PC slab. X and J in this figure are equivalent of K and M points in Figure 2.8 [48].

2.2.2 FDTD method

FDTD is a rigorous numerical solution of the Maxwells equations. This method provides the exact solution in any structure and does not have any theoretical approximations. This method is widely used to simulate integrated optic elements, and there is no limitation in using this method. On the other hand, other numerical methods such as Beam Propagation Method (BPM), is not capable of simulating of PC structures [52-53].

2.2.2.1 FDTD Algorithm

In a source free environment, the Maxwell's curl equations are represented by six scalar equations in Cartesian coordinates as follows [54]:

$$\frac{\partial H_x}{\partial t} = -\frac{1}{\mu}\left(\frac{\partial E_y}{\partial z} - \frac{\partial E_z}{\partial y}\right), \frac{\partial H_y}{\partial t} = -\frac{1}{\mu}\left(\frac{\partial E_z}{\partial x} - \frac{\partial E_x}{\partial z}\right), \frac{\partial H_z}{\partial t} = -\frac{1}{\mu}\left(\frac{\partial E_x}{\partial y} - \frac{\partial E_y}{\partial x}\right)$$

$$\frac{\partial E_x}{\partial t} = -\frac{1}{\varepsilon}\left(\frac{\partial H_z}{\partial y} - \frac{\partial H_y}{\partial z}\right), \frac{\partial E_y}{\partial t} = -\frac{1}{\varepsilon}\left(\frac{\partial H_x}{\partial z} - \frac{\partial H_z}{\partial x}\right), \frac{\partial E_z}{\partial t} = -\frac{1}{\varepsilon}\left(\frac{\partial H_x}{\partial y} - \frac{\partial H_y}{\partial x}\right) \qquad (2.17)$$

According to the above equations, the variation of the electric field in time depends on the space variation of the magnetic field and vise versa. To solve the Maxwell's curl equation, these equations must be discretized in both time and space domain.

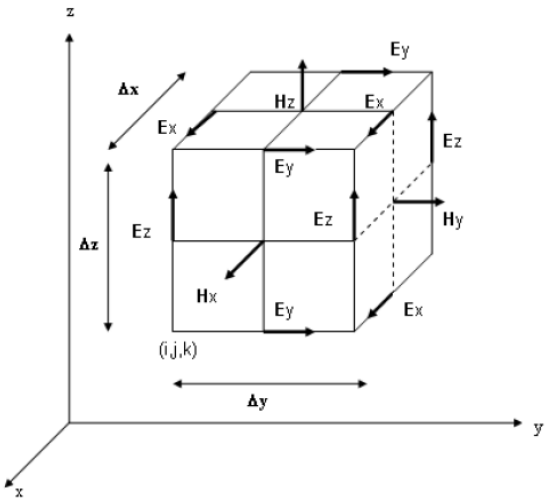

Figure 2.9 Three-dimensional Yee cell for FDTD

Yee solved above equation using finite-difference approach [55] by discretizing in space. Figure 2.9 shows the Yee cell where the grid point at space is denoted as:

$(i, j, k)=(i\Delta x, i\Delta y, i\Delta z)$

E and H are computed at the grid points. Grid points corresponding to H are shifted one-half grid spacing with respect to the E grid points. The discretized functions in space and time are expressed as follows [54]:

$$F(i\Delta x, i\Delta y, i\Delta z, n\Delta t)=F^n(i, j, k) \qquad (2.18)$$

Where the time steps are denoted by Δt. E filed is computed at $t=n\Delta t$; where as, H field is computed at $t=(n+1/2)\Delta t$. The finite difference equations corresponding to equation (2.17) are as follows [54]:

$$H^{n+1/2}_{x(i,j,k)} = H^{n-1/2}_{x(i,j,k)} + \frac{\Delta t}{\mu\Delta z}\left(E^n_{y(i,j,k)} - E^n_{y(i,j,k-1)}\right) - \frac{\Delta t}{\mu\Delta y}\left(E^n_{z(i,j,k)} - E^n_{z(i,j-1,k}\right) \qquad (2.19.a)$$

$$E^n_{x(i,j,k)} = E^n_{x(i,j,k)} + \frac{\Delta t}{\varepsilon\Delta y}\left(H^{n+1/2}_{z(i,j+1,k)} - H^{n+1/2}_{z(i,j,k)}\right) - \frac{\Delta t}{\varepsilon\Delta y}\left(H^{n+1/2}_{y(i,j,k+1)} - H^{n+1/2}_{z(i,j,k)}\right) \qquad (2.19.b)$$

The PML is used as the boundary condition in FDTD simulations. This technique is based on using an absorbing layer without any reflection of the electromagnetic waves.

2.2.2.2 The stability criteria

The grid size must be a fraction of the wavelength to make sure that the field does not change significantly over space increments. The size of the grid is usually λ/10, where λ is the wavelength in the material. For constant ε and μ, the stability criteria can be stated as follows [55-56]:

$$c\Delta t < \frac{1}{\sqrt{(1/\Delta x^2 + 1/\Delta y^2 + 1/\Delta z^2)}} \qquad (2.20)$$

Where c is the velocity of the light, the accuracy of FDTD method depends on the discrete time and space steps. As a rule of thumb, the minimum wavelength must at least contain 10 grid points.

2.3 PC slab waveguide

A waveguide in a PC slab can be created by removing one or more rows of holes along the propagation direction [57]. For example, Figure 2.10 shows a waveguide created by removing one row of holes along ΓK direction in a triangular PC slab suspended in air. The parameters of this structure are: *r/a=0.3*, *ε=11.56, t=0.6a*. To calculate the band structure of the waveguide using PWEM, the super cell technique was used. Figure 2.11 shows the super cell mapped onto the computational domain. The propagation direction is in the *x*-direction.

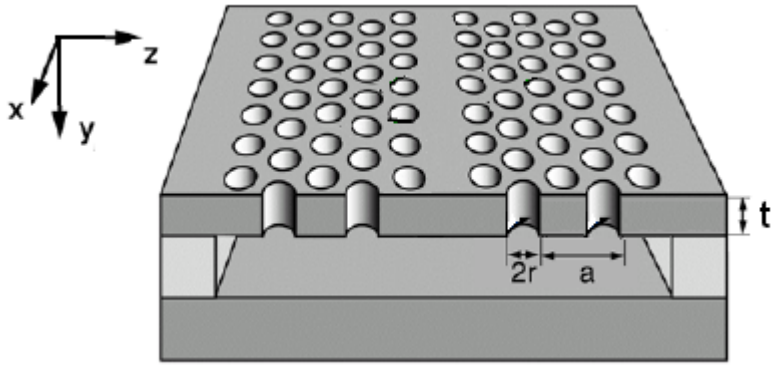

Figure 2.10 PC slab waveguide suspended in air [58]

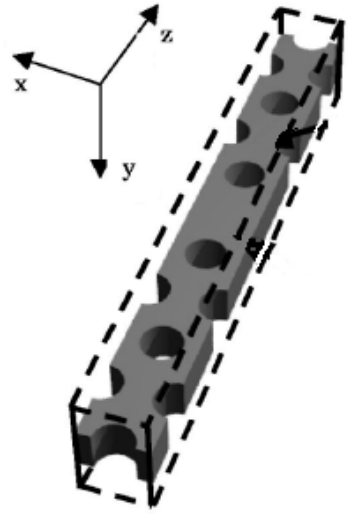

Figure 2.11 The super-cell for band calculation of the triangular based PC slab waveguide shown in Figure 2.10 [59].

Fig. 2.12 shows the band structure of the waveguide for TM-like polarization. In this figure, the vertical axis equals to a/λ, normalized frequency. By default, any frequency inside the PBG can not propagate in the PC, however, by creating a defect line, some frequencies or modes can propagate along the defect line due to the constructive interference caused by the reflected lights from the PC boundaries. This guiding mechanism is called PBG based guiding. These modes are called defect modes or Bloch modes. Figure 2.12 shows that introducing the defect line have induced two defect modes inside the PBG of the PC slab. An important concept in 2D PC slab waveguide is the

light line. In this case that the cladding is air, the light line is simply the wave vector divided by the free space index. For a periodic cladding, the boundary is the lowest band of the corresponding 2D PC calculated by 2D PWEM. Any mode that lies below the light line is a guided mode and has a real propagation constant, while the modes that lie above the light line have complex propagation constant and are called leaky modes [60-61].

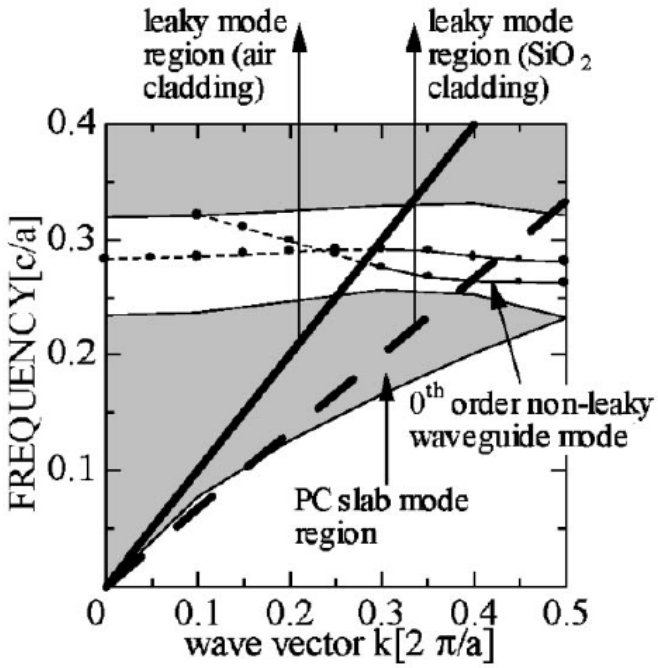

Figure 2.12 band diagram of the TM-like mode for a triangular based PC slab waveguide [59].

The guiding mechanism in the in-plane direction is based on the PBG mechanism, whereas in the vertical direction is based on total internal reflection. There are so many complexities in the guiding mechanism of PC slab waveguide. Numerous studies have been conducted to explore the guiding mechanisms of PC slab waveguide [60-63]. One of the most important issues of the PC slab waveguide is the out-of-plane loss. The propagating field in the PC slab will interact with the air holes where there is no refractive index contrast in the vertical direction. These air holes can be the cause of radiation leakage from the slab to the cladding due to the scattering of light. This is called out-of-plane loss and is caused by the coupling of the propagation field to the leaky modes [64-65]. There has been some research done to avoid the leaky modes by improving the design of the PC slab. For example, in Figure 2.12 over the normalized

frequency band of 0.27 to 0.28 no leaky mode exists and there is only the fundamental guided mode. The next higher order mode lies over the normalized frequency band of 0.28 to 0.29. By operating the waveguide in the frequency range of the fundamental and the next higher order mode, the leaky mode will be avoided. Nonetheless, finding the perfectly guiding mode is an issue in PC slab waveguide.

In the previous paragraph, the Bloch modes were assessed. The Bloch modes exist for TM-like polarization in a triangular lattice PC slab waveguide. On the other hand, no band gap exists for TE-like mode. Thus, no TE-like guiding would be expected in the PBG, yet TE-like guiding in the frequency band of the PBG has been observed. This TE-like guiding was associated with the index guiding mechanism, because of the index contrast between the PC area and the core, in the in-plane direction and index contrast between the core and the cladding in the vertical direction [62]. Since the TE-like and TM-like guide is based on a different mechanism, a significant difference in the guiding characteristics of the two polarizations was observed. This is an important property that can be utilized for the designing of polarization processor using PC slab waveguide which is discussed in the next section.

2.4 Polarization controlling devices

It has been recently shown that PC based devices can be employed to realize the polarization controlling devices [66-69]. Heuristically speaking, the strong polarization dependence of the wave propagation inside the PC can be associated with the geometrical anisotropy. According to the TE/TM definition in 2D PC slab, the electric field of the TE and TM polarizations are perpendicular and parallel to the plane of the periodicity, respectively. Thus, the Fresnel coefficients will be different at each material interface, this leads to the polarization dependence of the band gap characteristics such as: the center frequency, the width and the shape [70-71]. It is worthwhile to note that the polarization-dependent properties of the PCs are not limited to the characteristics of the

band gaps. This strong polarization dependence behavior is also observed in the transparent region, too [72].

One of the most crucial elements of polarization controlling devices in an integrated optic circuit is the polarization rotator structure that is capable of manipulating and rotating the input polarization to an arbitrary angle. No one has reported a PC based integrated polarization rotator. Li employed 2D PC consisted of 16 rows of metallic rods in microwave frequency to implement quarter wave plates [67]. The large birefringence in PC structure leads to a small optical path difference between the two polarizations which can be many times smaller than that of the conventional wave plates. The polarization rotation takes place at a transparent frequency band.

In this thesis, we are interested in an integrated polarization rotator structure that can easily be implemented and integrated with other optical elements. The following subsections will review the waveguide based polarization rotator structures, and briefly discuss their principle of operation.

2.4.1 Waveguide based passive polarization rotator

Passive polarization rotator structures are mostly composed of geometrically asymmetric structures. The symmetry of the structure must be some how disturbed so that two orthogonal polarizations could be coupled to each other. Several structures of longitudinally variable passive polarization rotators have been reported in literature including: a periodic asymmetric loaded rib waveguide [73], periodic tilted waveguiding section [74], periodically loaded strip waveguide [75] and cascaded bend waveguides [76-79].

Periodic asymmetric loaded rib waveguide was experimentally demonstrated by Shani [73]. The asymmetric loading of the waveguide would perturb the axes of the primary waveguide. By periodically alternating the loaded layer in longitudinal direction, as shown in Figure 2.13 (a), the polarization conversion or rotation will be accumulated coherently. The total length of the device was more than 3 mm. Shani himself was not able to explain the operating mechanism of the structure. Huang and Mao employed coupled mode theory based on scalar modes to analyze the structure theoretically [80]. Later on, Obayya and et al. employed full vectorial analysis based on the Versatile Finite

Element Beam Propagation Method (VFEBPM) to improve the design and reduce the polarization conversion length to 400 μm at operating wavelength of 1.55 μm [81]. Due to the huge size of the device, the design could not be verified with the aid of rigorous numerical methods.

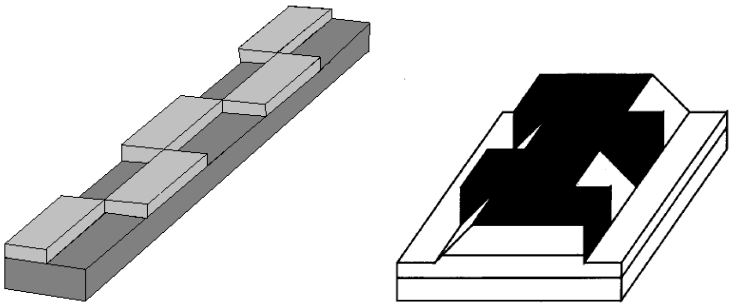

(a) (b)

Figure 2. 13 The sketch of periodic asymmetrical loading of rib waveguide (b) periodic tilted waveguide for polarization rotation application.

Based on the same idea, the tilted waveguiding polarization converter was introduced first by Heidrich [74]. The sketch of the device is shown in Figure 2.13(b). The first device was implemented by laterally tilting the InP/GaInAsP rib waveguide on a stepped substrate. The total length of the device was more than 7 mm at λ=1.55 μm [74]. Later on, by improving the design using coupled mode theory and BPM, a more compact device with the total length of 0.9 mm was implemented by Van der Tol [76]. Besides being bulky, the device undertakes huge coupling losses at the junctions between the adjacent periodic sections. To eliminate the loss, single section devices were proposed [82]. By increasing the optical rotation angle to 45^o, a 90^o rotation can be realized only by one section [82-84]. By using angled single section waveguides in the InP/InGaAs material system, another type of short polarization rotator was designed and fabricated [85]. The optical rotation angle will be discussed in the next section where the principle of operation for the geometrical asymmetric polarization rotator is discussed.

Silicon based polarization rotators are more attractive in the sense that the fabrication process is more compatible with the Complementary Metal-Oxide Semiconductor (CMOS) technology. Chen and et al. introduced a silicon slanted rib waveguide for polarization rotation [86]. Deng and et al. implemented a slanted wall in Si by wet etching of Si; thus, the side wall angle (52^o) was not a flexible parameter. The

total length of the fabricated device was more than 3 mm which is very long [87]. Moreover, the fabrication process of slanted-wall ridge waveguide is not compatible with planar optics circuit.

Recently, Wang and Dai proposed a Si nanowire based polarization rotator with asymmetrical cross section, depicted in Figure 2.14. The side wall is vertical, so it could be realized utilizing dry etching, reactive ion etching (RIE) [88]. They were able to design an asymmetric Si nanowire device as small as 10 μm. Single mode guiding is required to avoid multimode interface that leads to lower polarization conversion efficiency. The Si single mode silicon nanowires are so small that the fabrication of the rotator is very difficult and challenging. The fabrication tolerance is very small, as a result the proposed structure is not a robust device and a small fabrication error could diminish the performance of the device. Moreover, to achieve a compact polarization rotator, the height of the loading (h) is 240 nm that is almost half of the thickness of the nanowire (H=500 nm) leading to a huge coupling loss.

Having reviewed all the reported passive polarization rotator structures, there is an urgent need for a compact and low loss polarization rotator structure that can potentially be integrated with the in planar optical integrated circuit. We have taken advantage of the strong guiding in characteristics of the PC slab waveguide to implement a compact polarization rotator. The fabrication process of the PC based polarization rotator is compatible with integrated PC and planar optic circuits.

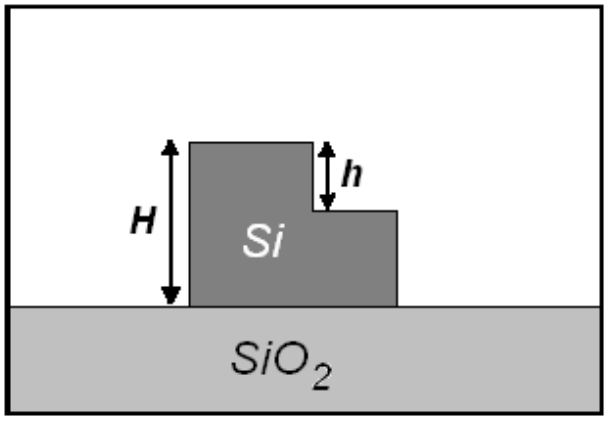

Figure 2.14 The sketch of the cross section of an asymmetric Si nanowire for polarization rotation application [88].

All passive polarization rotator structures are composed of geometrically asymmetric structures. Thus, geometrical asymmetry must be imposed to the PC structures for polarization rotation application.

2.5.1 Principle of operation of geometrically polarization rotator

Imposing asymmetry into a symmetric waveguide structure leads to a perturbation in the primary waveguide axes, as depicted in Figure 2.16 (a). E_f and E_s are projected fields on the fast and slow axes called fast and slow hybrid modes. They travel with different speeds resulting in a phase delay between the two components. For the phase delay of 180^o, the power conversion between the two components has reached to its maximum and the propagating distance is called the half-beat length L_π, defined as [89]:

$$L_\pi = \frac{\pi}{\beta_s - \beta_f} = \frac{\pi}{(n_s - n_f)k_0} = \frac{\lambda}{2(n_s - n_f)} \tag{2.21}$$

Where β_s and β_f are the propagation constants of the slow and fast modes, respectively. The process of polarization rotator in geometrically asymmetric structure can be explained with more details as following. According to Figure 2.15 (a), the transverse component of the hybrid modes (for example the asymmetric loaded rib waveguide in Figure 2.13a) can be expressed as follows:

$$E_s = \cos\varphi\hat{x} - \sin\varphi\hat{y} \tag{2.21.a}$$

$$E_f = \sin\varphi\hat{x} + \cos\varphi\hat{y} \tag{2.21.b}$$

Assuming that the input wave is x-polarized, it can be expressed as the combination of E_s and E_f as follows:

$$E_i = \cos\varphi\, e^{-j\beta_s z}E_s + \sin\varphi\, e^{-j\beta_f z}E_f \tag{2.22}$$

At half-beat length long, the slow and fast modes become out of phased resulting in destructive interference between the two modes. Thus, at $z=L_\pi$, the total field become:

$$E_{o1} = \cos\varphi E_s - \sin\varphi E_f \tag{2.23}$$

Substituting equation (2.21) into equation (2.23) results in:

$$E_{o1} = \cos 2\varphi\hat{x} - \sin 2\varphi\hat{y} \tag{2.24}$$

Thus, at $z=L_\pi$ the input wave has been rotated by 2φ with respect to the x-axis, as depicted in Figure 2.15(b). To avoid the reversal of power conversion and synchronize

the power conversion, where $\varphi<45^{o}$, the top loaded layer must be inverted w.r.t the center of the rib waveguide, Figure 2.13(a), at $z=L_{\pi}$ where z is the propagation direction. At the end of the next top loaded layer, the polarization of the input signal has been rotated by 4φ, as depicted in Figure 2.15(c). The top loaded layers will be arranged periodically and repeated until the total phase shift becomes 90^{o} [90].

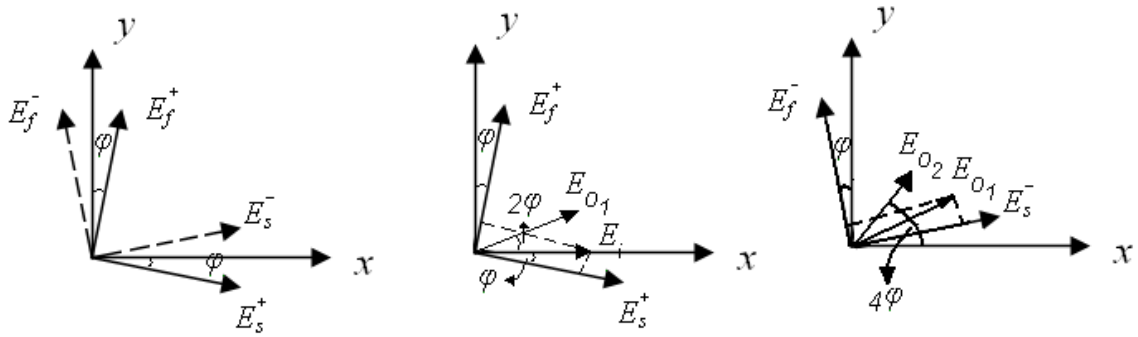

(a) (b) (c)

Figure 2.15 The sketch of the normal modes of a geometrically asymmetric structure (a) perturbed optical axis (b) sketch of the input electrical field and the rotated output field after propagation distance of L_{π} (c) sketch of the output field after $2L_{\pi}$ (E_s and E_f are the slow and fast modes, respectively).

In single section polarization rotator structures, φ is adjusted to 45^{o}; so that, a 90^{o} polarization rotation could be achieved by only one section.

Chapter 3

Design and Analysis of polarization selective PC slab waveguide

3.1 Introduction

The building block of an integrated photonic circuit is a waveguide. In other words, all other components of an integrated photonic circuit can be built using waveguide structure. As it has been pointed out in the introduction section, the focus of this thesis is to implement integrated PC based polarization selective devices. Depending on the application, the PC slab waveguide structure is designed to guide only one or both polarizations. For example a TE-polarizer only guides TE wave, whereas, a polarization rotator structure must be guiding both TE and TM waves.

This chapter will outline the design methodology for the polarization selective waveguide structure. In Section 3.2, a design methodology based on optimizing the thickness of the PC slab waveguide using full-wave 3D-FDTD simulation was presented.

We have shown that by varying the thickness of the PC slab waveguide the overlap between TE and TM guiding can be adjusted.

3.2 PC slab waveguide

An optical waveguide is constructed by introducing a defect line in a perfect PC. The guided modes of a PC slab waveguide are either index-guided modes or Bloch modes. The defect modes induced inside the bandgap are Bloch modes [91]. The confinement mechanism of the Bloch modes are based on Bloch reflection from the PC walls in the in-plane direction and total internal reflection in the vertical direction [47-49]. On the other hand, the confinement mechanism of the index-guided modes are based on the total internal reflection from both in-plane and vertical direction. The unique properties of the PC waveguide modes such as low-loss guiding through sharp bends are the manifestation of the Bloch modes [92]. Index-guided modes would experience the same loss as the modes of conventional waveguides.

Here, using 3D modal analysis along with spectral index method we have determined the guided modes for a PC slab waveguide. The thickness of the slab, *t* depicted in Figure 3.1, plays an important role on the loss characteristics of the PC slab waveguide [25]. Figure 3.1 shows the schematic of the 2D PC slab waveguide suspended in the air where *a*, *r* and *t* are the lattice constant, radius of the holes and the thickness of the PC slab, respectively. Knowing the propagation direction, z-axis, the dominant electric field component of TE-like wave is parallel to PC walls, E_y. The axial component of electric field is non-dominant. Similarly, the dominant component of magnetic field of TM-like wave is parallel to the PC walls, H_y and the axial component of magnetic field is non-dominant. In literature for 2D PC (in our Chapter-II), the convention used is such that for TE-like and TM-like waves the dominant components of electric field (E_x, E_z) and magnetic field (H_x, H_z) are in PC plane, respectively. For PC slab-waveguides, we have changed the convention to make it compatible with the definition of TE-like and TM-like waves used for conventional waveguides in optical and microwave community.

We have determined the thickness and polarization dependent guiding of the PC slab waveguide so that the overlap between TE-like and TM-like guiding can be adjusted by designing the thickness of the PC slab for the desired application. For example, simultaneous TE-like and TM-like guiding are desirable for some polarization processing devices such as a Polarizing Beam Splitter (PBS) and a polarization mode converter [93]. Single polarization guiding is desirable for polarizer structure [94]. In literature, 3D analysis of the PC slab waveguide has mostly been replaced by 2D analysis, and the effect of the finite thickness has been introduced through modification of the dielectric constant. In fact, the effect of the finite thickness of the slab was approximated by using effective refractive index of the fundamental guided mode of the PC slab waveguide [95]. The optimal thickness was usually chosen based on the photonic band gap size so that the optimum thickness of the slab produces the largest band gap size [59]. For example, a silicon based PC slab with r/a=0.29 and n_{Si}=3.4, where r, a and n_{Si} are the radius of the air holes, the lattice constant (see Figure 3.1) and refractive index of silicon slab, the maximum band gap size occurs for the thickness (t) of 0.6a [47]. In [49], the optimum thickness was estimated from the following formula:

$$t \approx \frac{1}{2\omega_{gap-bottom}\sqrt{\bar{\varepsilon}}}, \tag{3.1}$$

Where, $\bar{\varepsilon}$, t and $\omega_{gap\text{-}bottom}$ are the average dielectric constant, thickness of the slab and the radial frequency of the lowest edge of the PBG, respectively. This equation predicts optimal thickness of 0.7a, compared to the computed gap maximum at 0.*6a*.

Through rigorous numerical analysis, we have shown that the size of the gap is not the only criteria in selecting the slab thickness, but, the loss characteristics of the waveguide strongly depend on the thickness of the PC slab waveguide.

In the following section, a design methodology for polarization selective waveguide is presented.

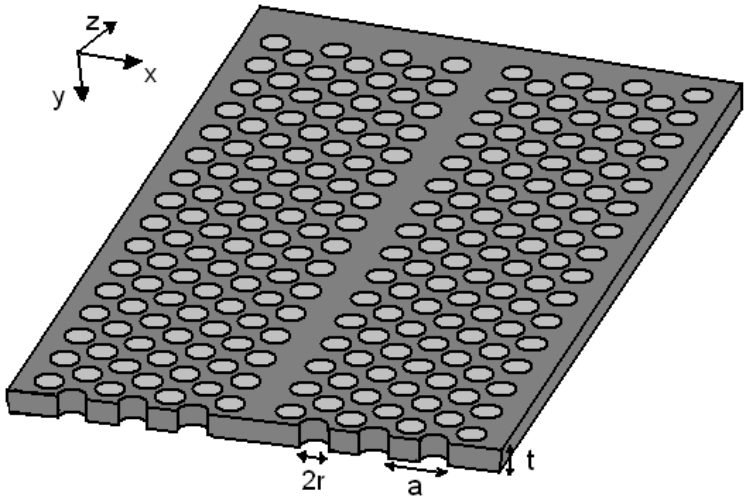

Figure 3.1 Schematic of a PC slab waveguide suspended in air.

3.3 Proposed Design Methodology

In this section, the design methodology for the polarization selective PC slab waveguide is explained. In the proposed design methodology, the variable parameter is the thickness of the Si PC slab waveguide membrane. In the first step, the modes of the PC slab are assessed to acquire the desired range of thickness needed, to provide the wide band gap. Thus, the study is limited to the aforementioned range of the thicknesses. Next, the dispersion diagram of the single defect line PC slab waveguide for both TE-like and TM-like polarizations are obtained and compared. Assuming that the TE-like and TM-like guiding mechanisms are based on the index-guiding and PBG guiding, the effective index method [96] and PWEM [51] are employed to obtain the dispersion diagrams, respectively. It is observed that by changing the thickness of the PC slab waveguide, the overlap between the TE-like and TM-like guiding varies. This allows one to find the thickness which provides the maximum overlap between the two polarizations. Finally, to verify the hypothesis made based on dispersion diagrams, 3D-FDTD simulations are carried out for the entire PC slab waveguide structure within the frequency band of the band gap. The loss diagrams obtained by 3D-FDTD simulations verify the hypothesis made in the previous steps.

3.3.1 Modes in PC slab

We start with the Plane Wave Expansion Method (PWEM) calculation of the PC slab's band diagram. For the calculation the PC slab's band diagram, the unit cell of the structure is mapped on the computational domain as shown in Figure 2.6. The PC slab has periodicity in the *x-z* plane and the propagation direction is in the *z* direction. The dominant (major) components of TM-like mode (H_y, E_z and E_x) have even symmetry with respect to y=0 plane as opposed to the non-dominant (minor) components (H_x, E_y and H_z) which have odd symmetry w.r.t y=0 plane. Similarly, the dominant components of TE-like mode (E_y, H_z and H_x) have even symmetry w.r.t. y=0 plane as opposed to the non-dominant components (H_y, E_z and E_x) which have odd symmetry w.r.t y=0 plane. Due to the opposite symmetry of the components of TE-like and TM-like waves, they can be decoupled from each other and studied separately. Since we are studying the t guiding properties and its thickness dependency for the 2D PC slab waveguide, it would be useful to graph the band gap size versus the slab thickness. Figure 3.2 shows the gap map of the triangular lattice PC slab, it showed the plot of PBG and the size of the PBG versus the PC slab waveguide's thickness for TM-like wave polarization. The graphs are generated by PWEM analysis. In this structure, the radius of the air holes and the lattice constant are r=123 nm and a=410 nm (r/a=0.3), while the refractive index of Si is assumed to be n_{Si}=3.48. An even symmetry is imposed on the H_y, E_z and E_x components w.r.t. y=0 plane. The simulation results give a band gap map for the TM-like modes of the PC slab. Band gaps do not exist for the TE-like modes. Figure 3.2 shows that the stop band moves toward lower frequencies as the thickness increases which is easily understandable. For thick slabs, higher order modes can be created with little energy, such modes lie only slightly above the lowest-order mode, preventing any gap. For too thin slabs, the slab provides a weak perturbation on the background dielectric constant, resulting in the existent of weakly guided modes [49].

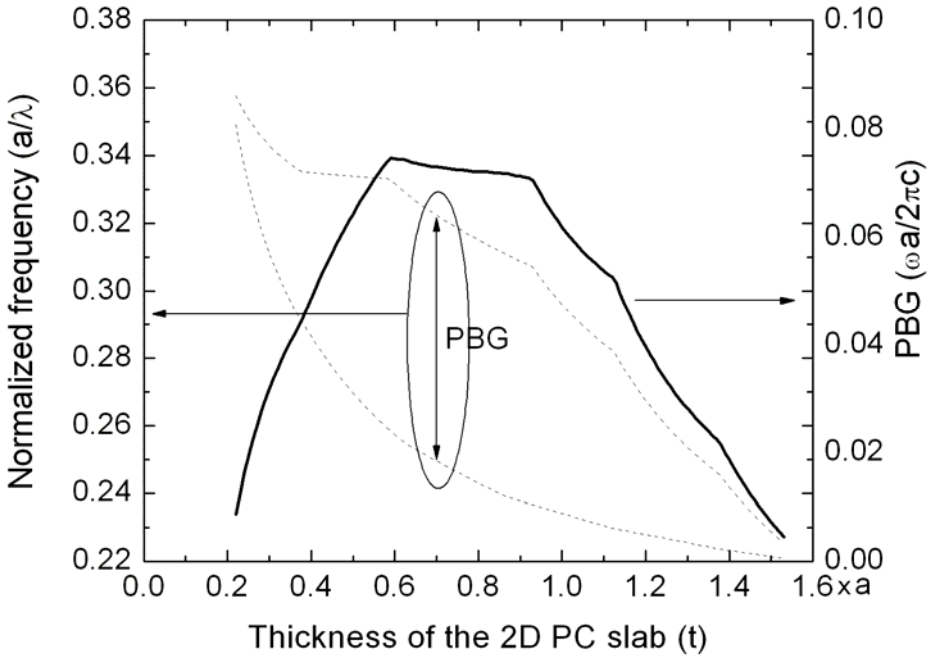

Figure 3.2 The Gap map and PBG size for the TM-like wave of the triangular based PC slab versus the thickness of the slab

3.3.2 PC slab waveguide with single defect-line

In this section, we study the propagating modes for both TE-like and TM-like polarizations along the defect line in the PC slab waveguide shown in Figure 3.1. TM-like modes are either index-guided or Bloch modes as opposed to the TE-like modes that are only index-guided. We are interested in the Bloch modes of the TM-like wave, because the Bloch modes have unique properties such as low-loss guiding through sharp bends. This makes our study limited to the TE-like index-guided modes and the TM-like Bloch modes.

To determine the TE-like modes of the PC slab waveguide, the effective index method is used. Although, TE-like modes do not have band gap, they still can be guided due to the index-guiding (in-plane as well as out-of-plane directions) [61-62]. In order to determine the appropriate thickness of the slab, we have employed the effective index method in both in-plane and out-of-plane directions to obtain the cut-off frequency of the fundamental mode. To employ the effective index method, the PC slab waveguide is

replaced by a conventional slab waveguide as shown in Figure 3.3, where n_{Si}, n_C and n_0 are the film, cladding and free space refractive indices, respectively. The width of the film layer (as depicted by W_0 in Figure 3.3) of the equivalent conventional slab waveguide is $W_0=a$. In fact, the missing row of air holes is replaced by the film layer of the equivalent slab waveguide. The following relation approximates the cladding refractive index for the TE-like polarization for which the electric field is parallel to the air cylinders in the PC pattern [97]:

$$n_c = \frac{\pi r^2}{a^2} n_0 + (1 - \frac{\pi r^2}{a^2}) n_{Si} \qquad (3.2)$$

Since, n_c represents the average refractive index of the cladding structure, the problem is simplified to finding the effective refractive index of the fundamental guided mode of the effective structure shown in Figure 3.3 for the TE-like polarization.

For TM-like polarization, the guiding mechanism for the in-plane direction is based on Bloch reflection and in the vertical dimension is based on total internal reflection. Though, the TM-like wave also has index-guided modes, but we are only interested in TM-like Bloch modes. The TM-like modes are calculated with the PWEM, which uses the concept of super-cell, depicted by the dashed line in Figure 3.4. The propagation direction of the waveguide is in the z direction. The periodic boundary conditions have been applied in all three directions.

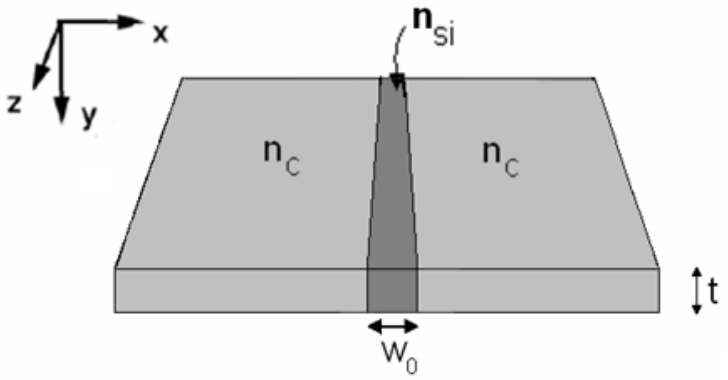

Figure 3.3 The effective slab waveguide of the PC slab waveguide, n_C, n_{Si}, t and w_0 are the refractive indices of the cladding and film (silicon) layers, thickness of the slab waveguide and the width of the film layer ($W_0=a$), respectively.

Finally, after obtaining the cut-off frequency of the TE-like mode and the spectrum of the TM-like modes, the cut-off frequency of the fundamental TE-like mode is compared with the frequency of the defect modes (TM-like modes) in the PBG.

To verify the modal analysis performed in previous steps, the 3D-FDTD simulation is carried out to obtain the transmission loss associated with the TE-like and TM-like polarizations within the frequency range of the band gap. For the 3D-FDTD simulations we have used the FullWAVE and BandSOLVE tools of the RSOFT package, version 5.1.8.2.

The simulated structure (Figure 3.1) consists of 100 rows of holes along the propagation direction (z-direction) and 11 rows of holes (including the defect row) in x-direction, however, only 50 rows in the middle of the structure, where the electromagnetic field distribution has become stable and all evanescent modes have vanished, are selected for loss calculation. Thus, the coupling loss has been excluded from the loss calculation. The mesh sizes along the x, y and z-directions (Δx, Δy and Δz) are $\Delta x=\Delta y=\Delta z=20.5$ nm. Hence, the 20×20 mesh cells describe the PC unit cell in the in-plane (x-z plane) direction. The 3D-FDTD simulations are repeated for three thicknesses, $t=0.5a$, $0.75a$ and a.

The Perfectly Matched Layer (PML) boundary condition is applied for all three directions. Time waveforms in the 3D_FDTD simulation have been chosen as a single frequency sinusoid with normalized frequency within the frequency band of the PBG. The spatial distribution of the incident field follows the symmetry of the mode, such as, the fundamental TM-like mode, where a spatial Gaussian distribution has been used as the incident field to excite this mode. Whereas, the spatial distribution of the next higher order TM-like mode's incident field has an odd symmetry with respect to the (z-y) plane bisecting the middle of the defect line.

To determine the transmission loss from the 3D-FDTD simulation results, the net power crossing at several cross sections (x-y planes) are calculated by integrating the Poynting vectors across each cross section. This allows, the axial power flow to be plotted along the propagation direction, z-axis. The errors due to the FDTD simulation lead to the fluctuation of the power along the propagating direction. To eliminate this fluctuation, Least Square method has been employed to fit the power to a power

transmission equation. To facilitate the calculation of the transmission loss in db/mm, the transmission loss equation is chosen in the form of, $T \propto 10^{-\alpha z}$, with this model, α directly gives the transmission loss in dB/mm, assuming that the unit of z in the transmission loss equation is in mm.

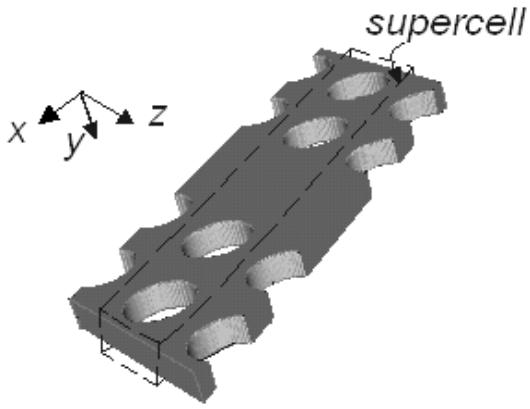

Figure 3.4 The super-cell for band calculations of the waveguide. The propagation direction is along z-axis.

3.4 Simulation results

In Figure 3.5, we present the dispersion curves of the TE-like modes of the effective slab waveguide as depicted in Figure 3.3 as a function of the normalized in-plane k vector for three values of the thicknesses, t=0.5a, 0.75a and a. t is the thickness of the PC slab waveguide. Assuming:

$$\vec{k} = \vec{\kappa} + \hat{y}k_y \qquad (3.3)$$

Where, $\vec{\kappa}$ is the in-plane k vector. The light line is plotted by the dashed line in this figure. For this structure with air cladding, the light line is simply the wave number divided by the refractive index of air.

The modes above and below the light line are guided and leaky, respectively. For t=0.5a, the highest normalized cut-off frequency of the fundamental mode (with $\kappa a/2\pi$=0.5) is around 0.33.

Next, we proceed to calculate the TM-like modes spectrum of the structure (t=0.5a). PWEM has been employed to obtain the spectrum of the Bloch modes inside the band gap of the PC slab. The Bloch modes are TM-like. Figure 3.6 (a) shows the

spectrum of the fundamental and the next higher-order Bloch modes (TM-like modes). The light line is represented by the dashed line in the figure. Part of the TM-like mode on the left side of the light line physically does not represent a bounded mode. In this region, the energy is mostly dispersed into the leaky modes without any guidance.

In Figure 3.6(a), the fundamental TM-like mode is placed at the normalized frequency range of 0.28-0.29. Figure 3.6(a) also shows that the next higher-order TM-like mode is placed over a very narrow range of frequency, 0.301-0.302. It is observed that the TM-like modes are below the normalized cut-off frequency of the TE-like polarization of the equivalent slab discussed earlier (see Figure 3.5). Therefore, no TE-like guiding is expected to take place over the frequency band of the TM-like modes.

To verify the aforementioned results, the 3D-FDTD simulations have been carried out for the entire structure (Figure 3.1, t=0.5a). Time waveforms in 3D_FDTD have been chosen as a single frequency sinusoid with normalized frequency in the range of 0.265-0.34. The cross-section of both TE-like and TM-like waves are plotted. Figure 3.7 shows the cross-section of E_x, H_y and E_z components of TM-like wave (dominant components) at normalized frequency of a/λ=0.28. Figure 3.8 shows the dominant components of TE-like wave (H_x, E_y and H_z), displaying even symmetry w.r.t. y=0 plane at a/λ=0.32.

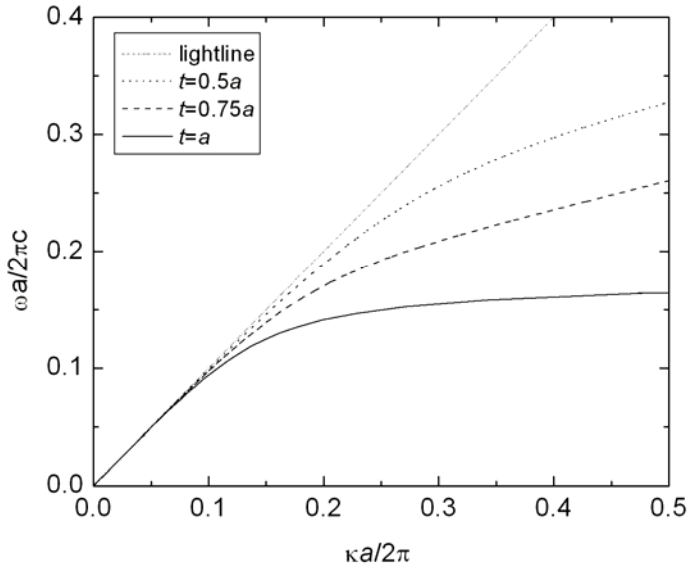

Figure 3.5 The dispersion diagram for the TE-like polarization of the equivalent slab waveguide for three different thicknesses.

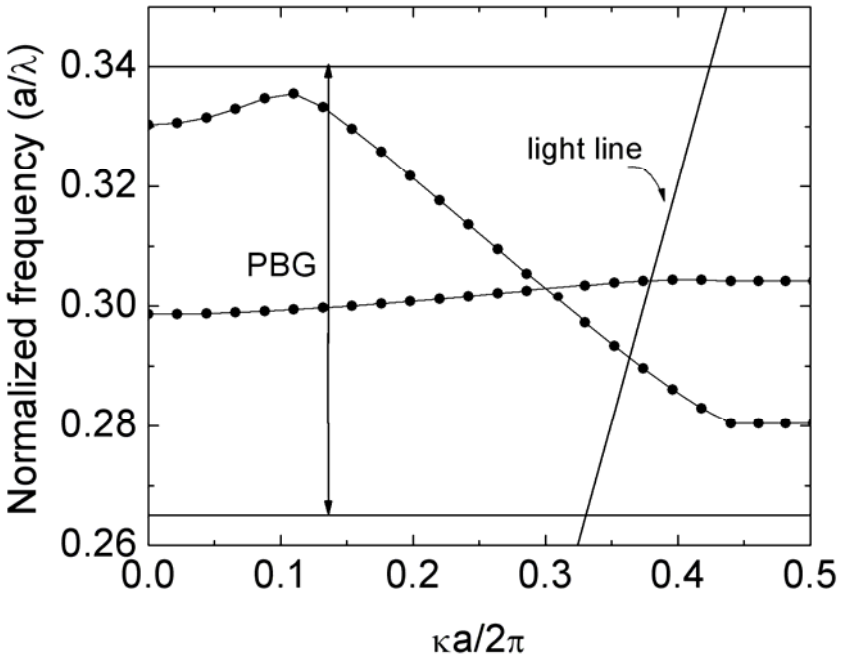

(a)

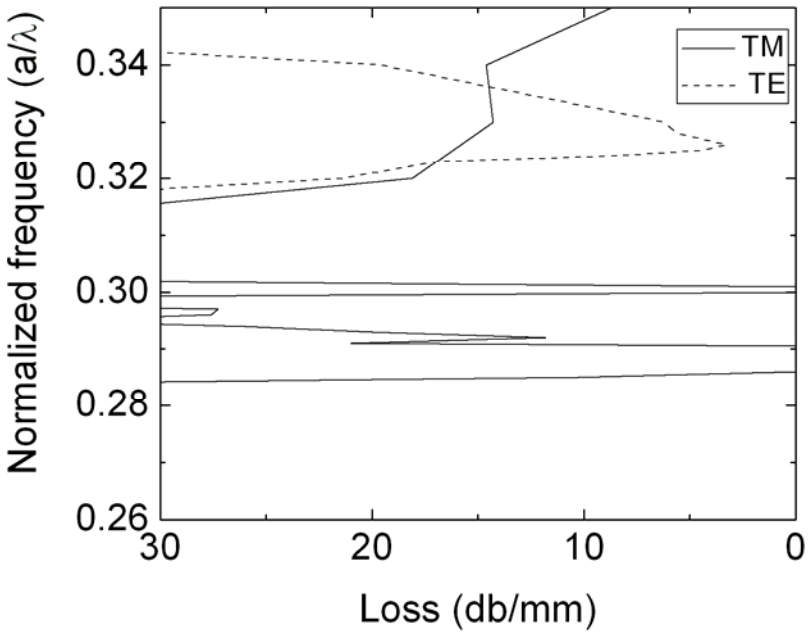

(b)

Fig. 3.6 (a) Band diagrams for TM-like modes and (b) loss as a function of the normalized frequency (*a/λ*) for the triangular based PC slab waveguide with *t*=0.5*a* and *r/a=0.3* (*a=410 nm*). PBG is the band gap size for the PC slab.

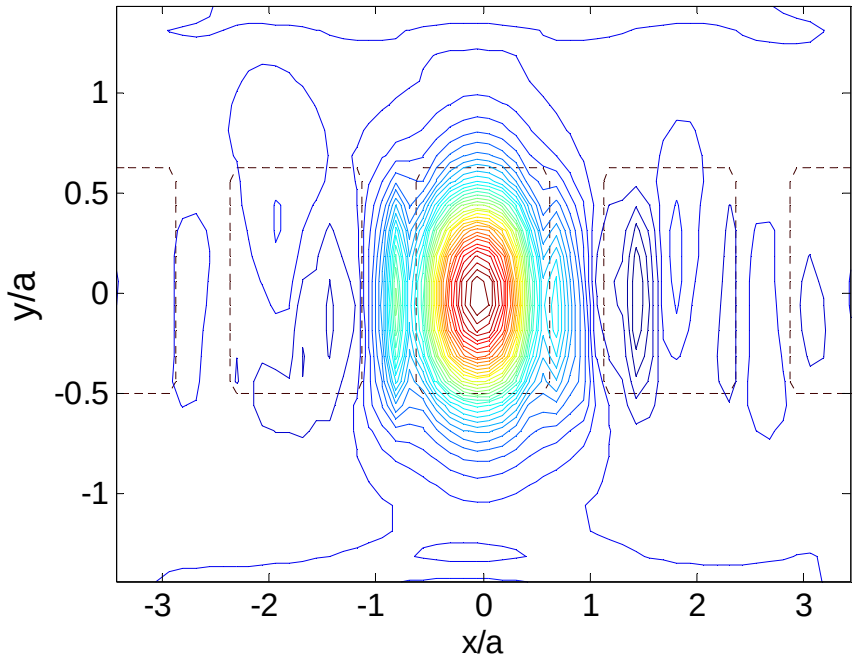

(a)

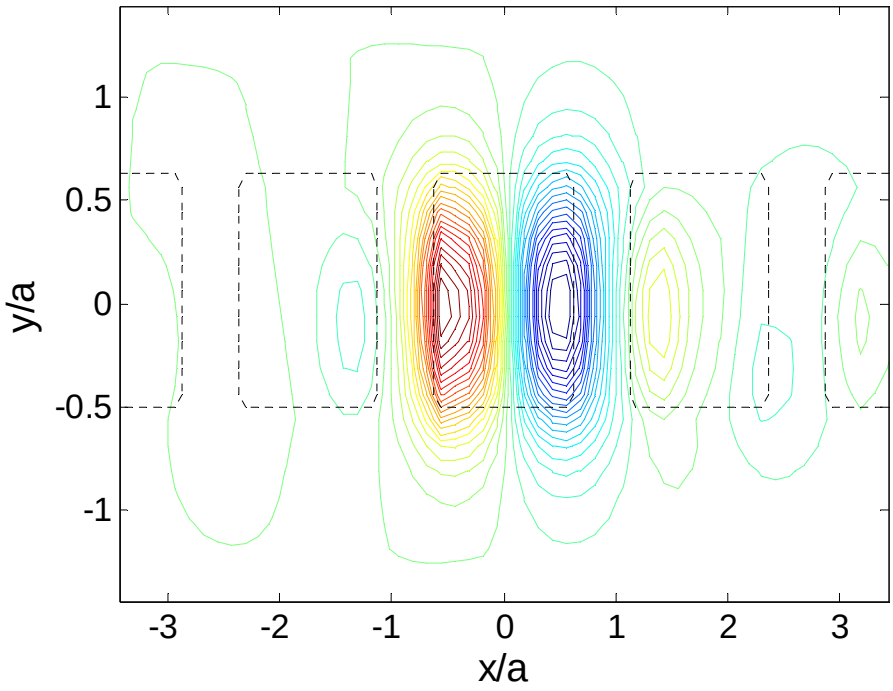

(b)

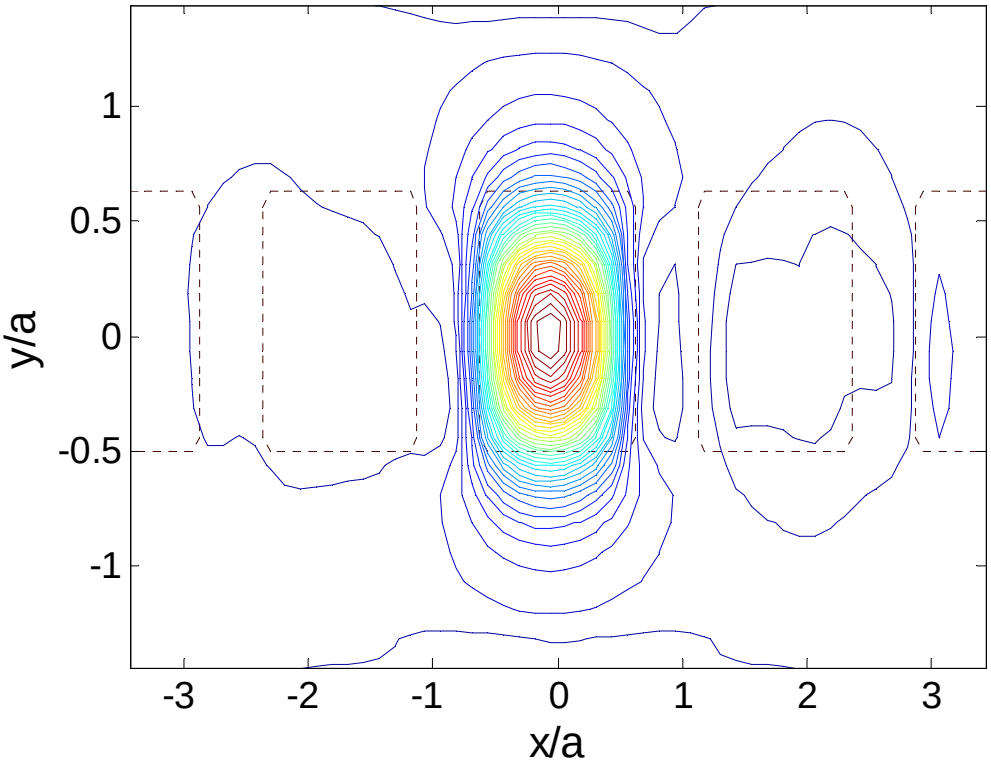

(c)

Figure 3.7 Cross-section of dominant field components of TM-like wave obtained by 3D-FDTD (r=0.3a, t=0.5a, n_{si}=3.48, a=410 nm and a/λ=0.28) (a) E_x (b) E_z (c) H_y.

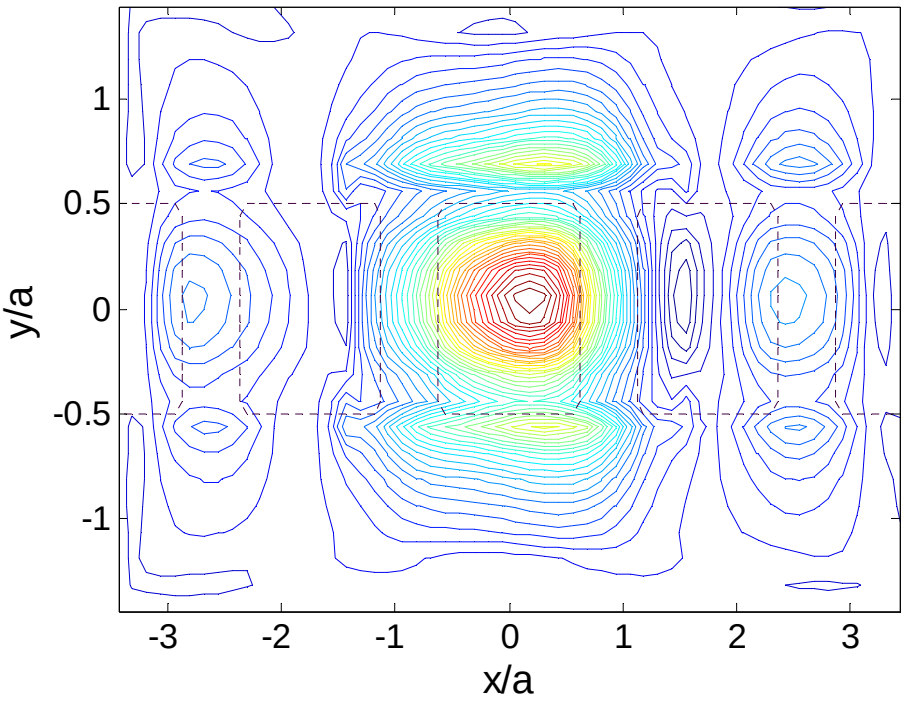

(a)

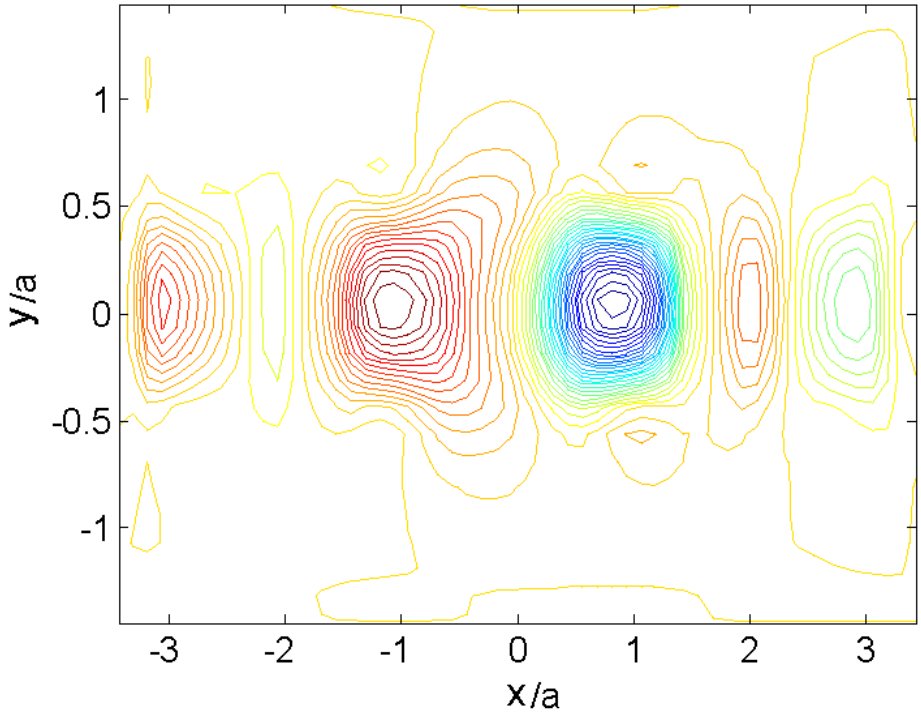

(b)

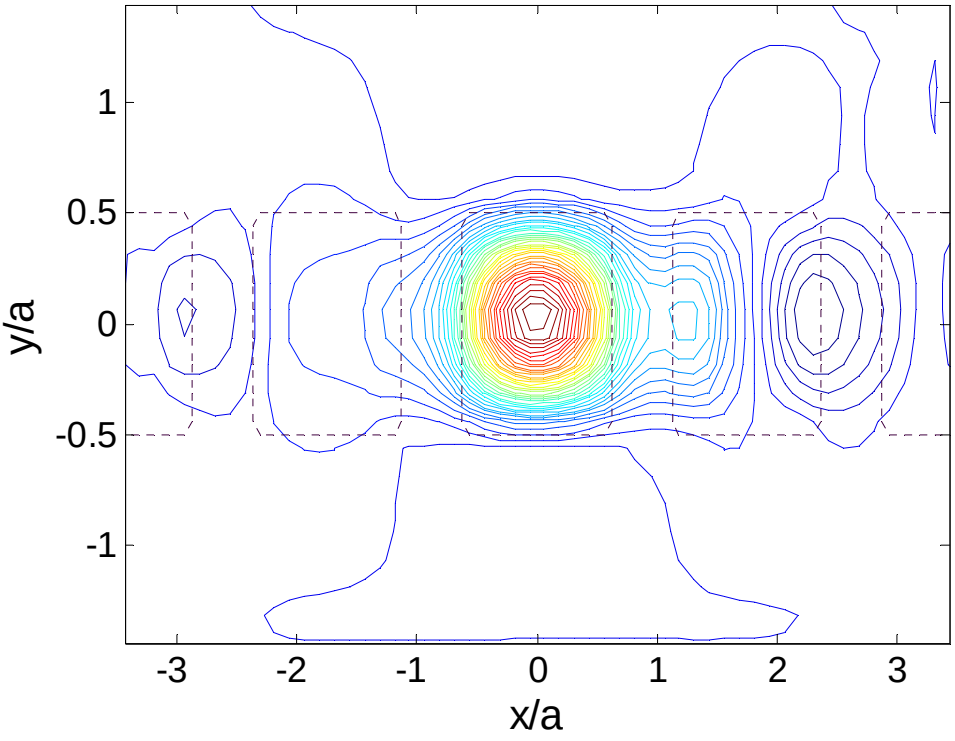

(c)

Figure 3.8 cross-section of field components for TE-like wave at a/λ=0.32 for t=0.5a, r=0.3a, n_{si}=3.48, a=410 nm (a) E_y (b) H_z (c) H_x.

The transmission loss (α) in dB/mm has been calculated and plotted in Figures 3.6(b), 3.9 (b) and 3.11 (b). In Figure 3.6 (b), and in the subsequent plots, the loss is graphed along the horizontal axis to keep the format of the loss diagrams consistent with the format of the band gap diagrams used in this thesis. The TE-like and TM-like modes are shown by a dashed line and a solid line, respectively. Modal propagation is seen for the normalized frequency of 0.285-0.29 and 0.3, which are very close to the modes obtained by the PWEM modal analysis for TM-like mode (see Figure 3.6(a)). Figure 3.6(b) also shows no TE-like modal guiding taking place in the frequency band of the fundamental and the next higher order TM-like modes as expected. Meaning, no overlap between TE-like and TM-like modal guiding exists for t=0.5a. Accordingly, in order to overlap TE-like and TM-like guiding, the cut-off frequency for TE-like mode must take place at frequencies lower than the frequency range of the Bloch modes (TM-like

modes). By increasing the thickness of the PC slab waveguide, the cut-off frequency for TE-like modes moves toward lower frequencies as depicted in Figure 3.5.

When we increased the thickness to t=0.75a, the highest normalized cut-off frequency of the fundamental TE-like mode of the equivalent slab (Figure 3.3) for $\kappa a/2\pi$=0.5 is less than 0.25, which is almost the lower edge of the band gap for TM-like wave. Thus, the cut-off frequency of the TE-like is certainly below the frequency range of the Bloch modes (TM-like modes). To obtain the characteristics of the PC slab waveguide's TM-like modes, the PWEM again was employed. Figure 3.9(a) shows the band structure of the TM-like modes obtained by the PWEM. The fundamental TM-like mode is placed in the frequency range of 0.255-0.27. The next higher-order TM-like mode is a very narrow band mode around the normalized frequency of 0.278. For this case, the frequency band of the TM-like modes are above the normalized cut-off frequency of the TE-like mode of the equivalent slab (Figure 3.3), we expect to have both TE-like and TM-like guiding over the frequency band of the TM-like modes.

To verify these observations, a 3D-FDTD simulation was carried out for the entire structure (t=0.75a, Figure 3.1). Time waveforms in 3D_FDTD have been chosen as single frequency sinusoids with a normalized frequency in the range of 0.23-0.34. Figure 3.9(b) shows the loss per mm versus the normalized frequency for both TE-like and TM-like polarizations obtained by the 3D-FDTD simulations. Modal propagation for both TE-like and TM-like polarizations over the frequency band of the fundamental TM-like mode, i.e. 0.26-0.268, is seen in Figure 3.9 (b). The TE-like polarization appears to experience loss at normalized frequencies higher than 0.275. The loss occurs in the in-plane direction; nevertheless, the TE-like mode is confined in the vertical direction (as per the 3D-FDTD field distribution results).

To comprehend the behavior of the TE-like mode, the dispersion diagram of the laterally even TE-like mode is computed and presented in Fig. 3.10 (depicted by the solid dotted line). The accurate dispersion analysis of the TE-like mode is based on the Spatial Fourier Transform (SFT) of the electromagnetic field distribution in the PC slab waveguide along the propagation direction at any point on the plane normal to the propagation direction (plane y-x) [98]. The electromagnetic field distribution is determined using 3D-FDTD. The peaks of the SFT spectrum describe the propagating

modes of the structure. These peaks are independent of the location, (x,y) and the electromagnetic field components. The spectrum of the field component has one peak in the regions where no PC slab mode exists. This peak is associated with the guided TE-like mode. On the other hand, in regions where the PC slab modes exist, other peaks associated with the PC slab modes are also observed. The dispersion diagram of the TE-like mode is also computed employing the PWEM in regions where no PC mode exists. The results achieved by both methods are similar.

The TE-like guiding takes place below all PC modes depicted by the gray area in Fig. 3.10. This mode is the index-guiding mode that does not see the periodic structure, but the effective material with the refractive index less than n_{Si}. There is no upper limit for this mode since it does not see the periodic PC. This mode is folded back at the zone boundary of the first Brillouin zone ($\kappa a/2\pi=0.5$) [64]. The lower limit of the mode takes place approximately at the normalized frequency of $a/\lambda=0.2$. These modes cross the region where the PC modes exist at $a/\lambda=0.27$ which determines the upper limit since it leaks the energy into the PC. Thus, in the loss diagram, the upper limit is observed for the TE-like mode.

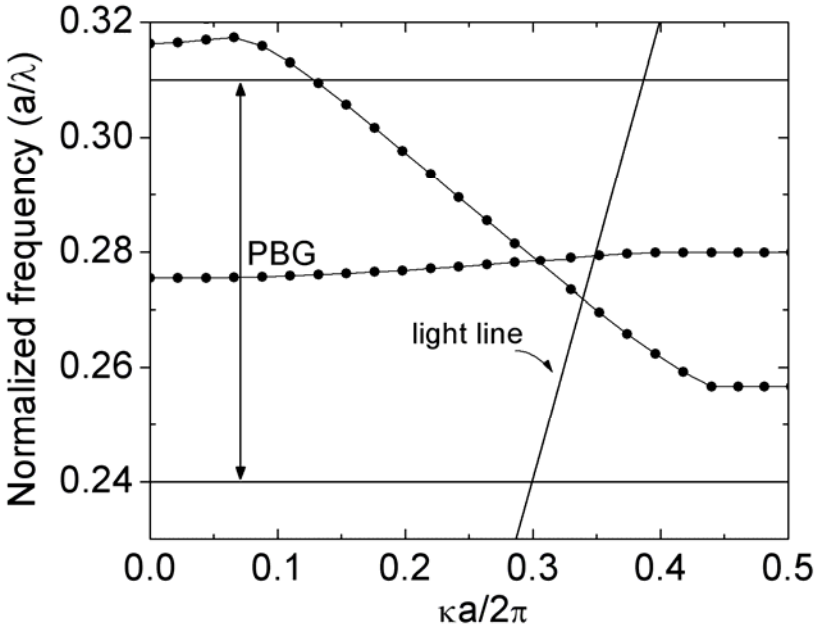

(a)

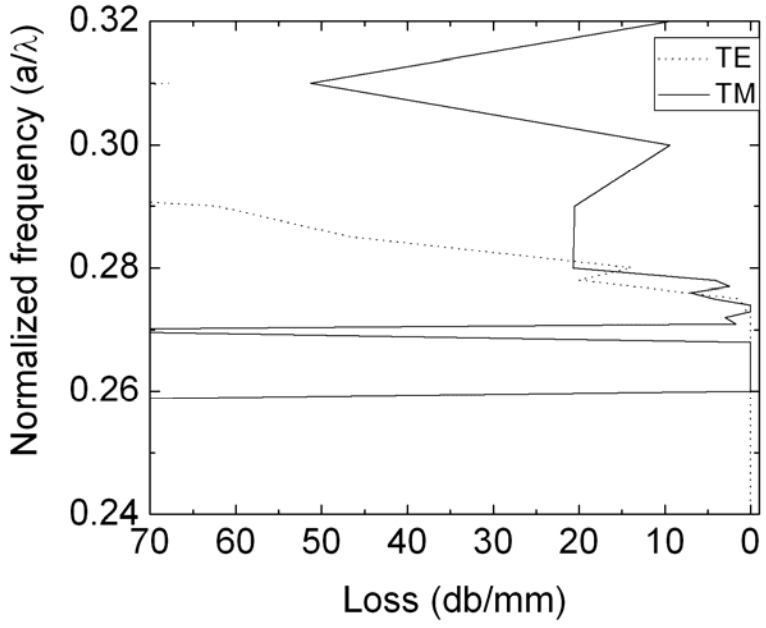

(b)

Fig. 3.9 (a) Band diagrams of the TM-like mode and (b) Loss as a function of the normalized frequency (*a/λ*) with *t=0.75a* and *r/a=0.3* (*a=410 nm*). PBG is the band gap size for the PC slab.

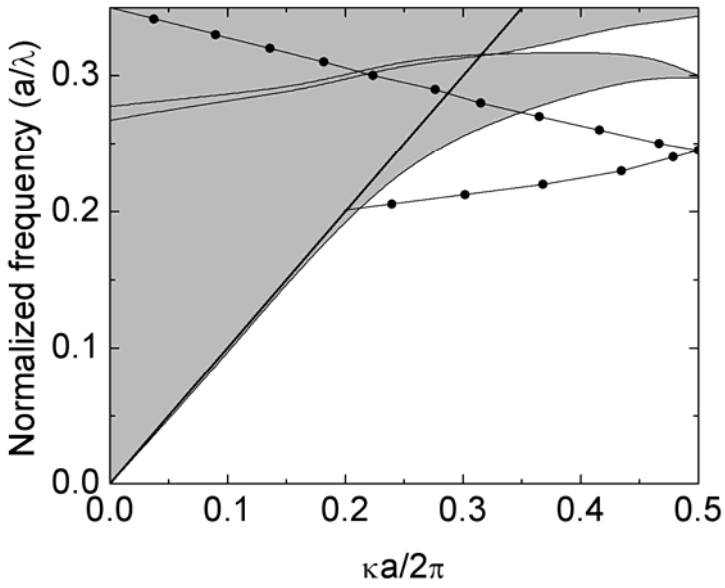

Fig. 3.10 Dispersion diagram for laterally even TE-like mode depicted by solid dotted line with *t=0.75a* and *r/a=0.3* (*a=410 nm*). The solid line represents the light line. Gray region correspond to the PC slab modes.

The simulation results for two different thicknesses suggest that for t=0.75a, lossless propagation for the TM-like polarization over the normalized frequency band of 0.26-0.268 and 0.272-0.273 is achieved in which TE-like guiding is also lossless. In fact, by increasing the thickness to 0.75a, the overlap between TE-like and TM-like modal guiding has been increased in the sense that the cut-off frequency for TE-like modes has been pushed down below the frequency band of the fundamental TM-like mode.

To investigate whether the overlap between the frequency bands of the TE-like and TM-like modes improves by increasing the thickness of the PC slab waveguide the thickness is increased to t=a. For the TE-like mode, the normalized cut-off frequency for t=a is around 0.15 according to Figure 3.5. The fundamental TM-like mode obtained by the PWEM is placed in a normalized frequency range of 0.243-0.26 and the next higher-order TM-like mode is a narrow band mode placed approximately at the normalized frequency of 0.266 (Figure 3.11(a)). Hence, for this case, the TM-like modes are located above the normalized cut-off frequency of the TE-like mode of the equivalent slab (Figure 3.3). So, modal TE-like and TM-like guiding is expected to be seen within the

frequency band of the TM-like modes. Furthermore, the higher order Bloch mode (TM-like mode) is also pushed down inside the PBG.

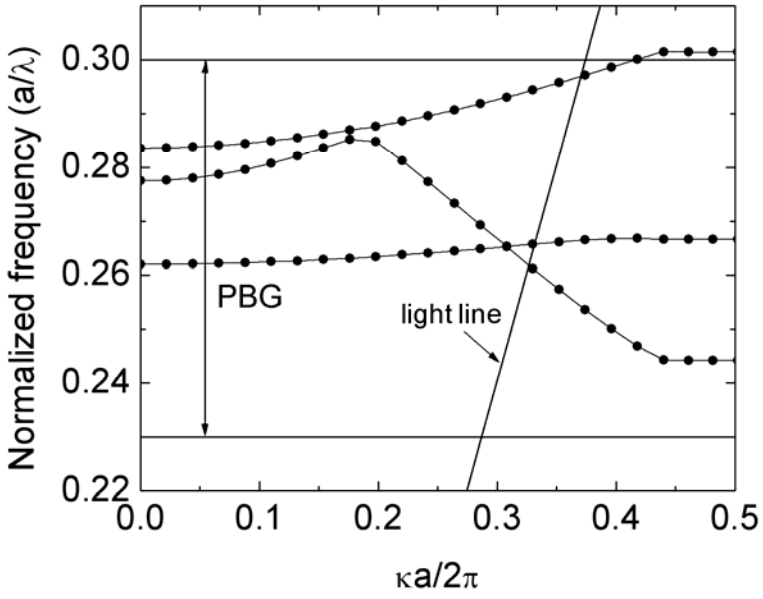

(a)

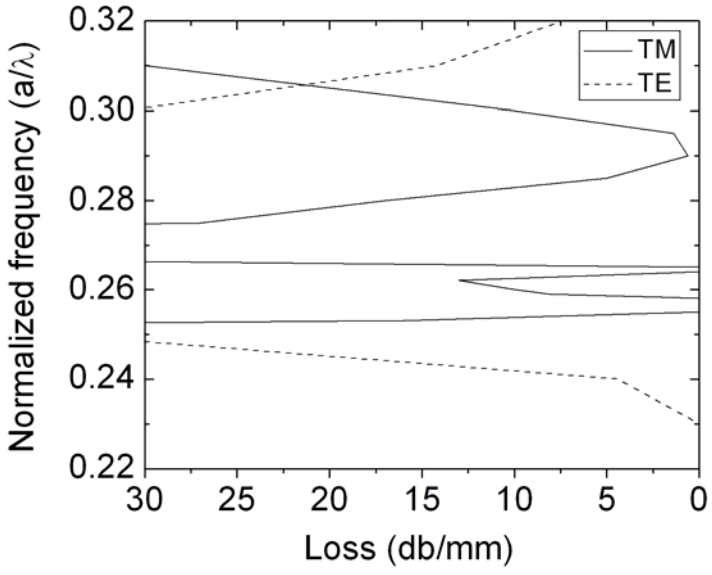

(b)

Fig. 3.11 (a) Band diagrams for TM-like modes and (b) Loss as a function of the normalized frequency (*a/λ*) for the triangular based PC slab waveguide with *t=a* and *r/a=0.3* (*a=410 nm*). PBG is the band gap size for the PC slab.

The 3D-FDTD simulation results for both TE-like and TM-like polarizations are shown in Figure 3.11(b). These 3D-FDTD simulation results for the TM-like mode are depicted by the solid line in Figure 3.11(b). They show a lossless propagation over the frequency range of 0.255-0.258 and 0.264-0.265. The higher order mode is also observed within the band gap. The simulation results for the TE-like mode show that the TE-like guiding is lossless up to the normalized frequency of 0.23. Then, above this frequency the propagation is no longer lossless. The dispersion diagram for the laterally even TE-like mode, Figure 3.12, indicates that at frequencies above a/λ=0.23, the TE-like mode depicted by a dotted solid line in the figure falls into the gray region and leaks the energy to PC slab modes. Therefore, the TE-like polarization is not guided over the frequency range of the fundamental and the next higher-order TM-like modes, and thicker slabs do not necessarily provide wide band lossless propagation for both TE-like and TM-like polarizations.

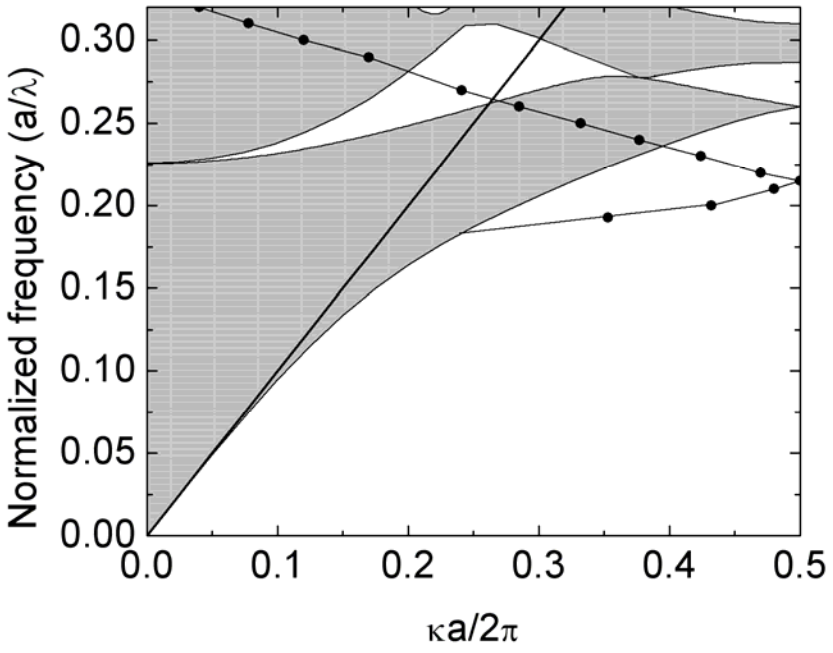

Fig. 3.12 Dispersion diagram for laterally even TE-like mode with *t=a* and *r/a=0.3* (*a=410 nm*). The solid line represents the light line. Gray region correspond to the PC slab modes.

The simulation results suggest that both TE-like and TM-like modal guiding in PC slab waveguide can be achieved by optimizing the thickness of the PC slab waveguide. For a PC slab waveguide to accommodate both TE-like and TM-like modal guiding, it must be thick enough to ensure that the TM-like mode lies above the cut-off frequency of the TE-like mode. A rough estimation can be obtained by using effective index method. For example, the cut-off frequency of the TE-like mode for t=0.5a lies above the TM-like mode frequency, meaning, no overlap between TE-like and TM-like guiding is observed. On the other hand, for thick slabs where the cut-off frequency is well below the frequency band of the bandgap, the TE-like wave has already become lossy at the frequency band of the TM-like mode and lost its energy to the PC slab modes. As a result, no overlap between the modal guiding of the two polarizations exists. The 3D-FDTD simulation results show that t=0.75a is a good choice for maintaining a loss-less TE-like and TM-like guiding, since the upper cut-off frequencies for both TE-like and TM-like waves are almost the same. We can conclude this section by the following statements:

- Although, the PBG frequency band of the TE-like polarization has no overlap with the PBG frequency band of the TM-like polarization, TE-like modes can still be guided in the TM PBG frequency band by means of the index guiding.
- For a very thin PC slab where the cut-off frequency of the fundamental TE-like index guided mode lies above the PBG frequency band of the TM-like mode, no vertical confinement is achieved for the TM-like Bloch modes. Therefore, the out-of-plane loss of the TM-like Bloch modes is quite high.
- For thick PC slabs, the TE and TM polarization can be split, and propagate independently, as a result, the PC slab waveguide can be employed as polarizer that filters one polarization and let the other one through.
- The thickness of the PC slab can be optimized to achieve wide band, loss-less guiding for both TM-like and TE-like waves that can be employed for polarization rotator structures.

3.5 Slow modes of PC slab waveguide

In the previous section, the fundamental index-guided and Bloch modes were studied closely. In plotted Band diagrams, Figures. 3.6(a), 3.9(a) and 3.11(a) show the next higher order Bloch modes were also present. The loss spectrum of the next higher order Bloch mode was included in loss diagrams for all three slab waveguide thicknesses (t=0.5a, 0.75a and a). The next higher order Bloch mode has a very narrow band as the band diagram associated to this mode is flat. Moreover, it has a very small group velocity or in other words, it is very slow. Slow light regime in PC structures has attracted lots of attention recently [99-101]. For example, there is one application to enhance light-matter interaction in non-linear optical systems [102-103]. In all-optical systems, optical nonlinearities are used, however, optical nonlinearities are usually very weak. Thus, a large interaction length or high operation power is required to improve the interaction between the material and light. One way to enhance the interaction length is to utilize slow light. Another application of slow light propagation is in optical delay lines where light is to be slowed down. By operating PCs in their slow light regime, compact delay lines can be realized [104-105].

It is important to note that due to a large impedance mismatch between the slow mode and injected field from a conventional optical waveguide, the coupling efficiency is quit low [106]. Several light injectors are proposed to enhance the injection of light to the PC slab waveguide at slow mode regime [106-108].

In this section, we are only interested on the study of the propagation characteristics of slow mode, where the exact mode is excited inside PC slab waveguide to eliminate coupling loss. Furthermore, we have limited our study to the next higher order Bloch mode and not the band edges.

Figure 3.11 (a) shows that the next higher order mode of the PC slab waveguide with r=0.3a and t=a is sitting within a very narrow normalized frequency band of 0.266-0.267. Figure 3.13 (a), (b) and (c) show the cross-section of the E_x, H_y and E_z components of the TM-like wave at the normalized frequency of a/λ=0.266. The higher order Bloch mode is a TM-like wave; hence, E_x, H_y and E_z have even symmetry w.r.t. y=0 plane while E_x and H_y components have odd symmetry w.r.t. x=0 plane.

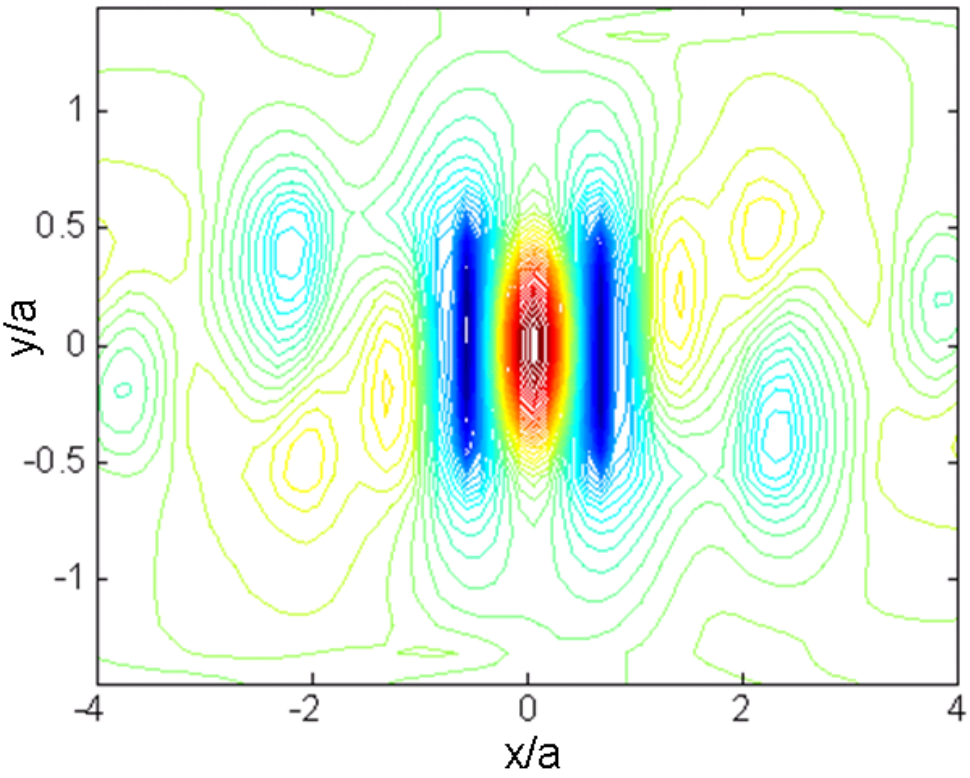

(a)

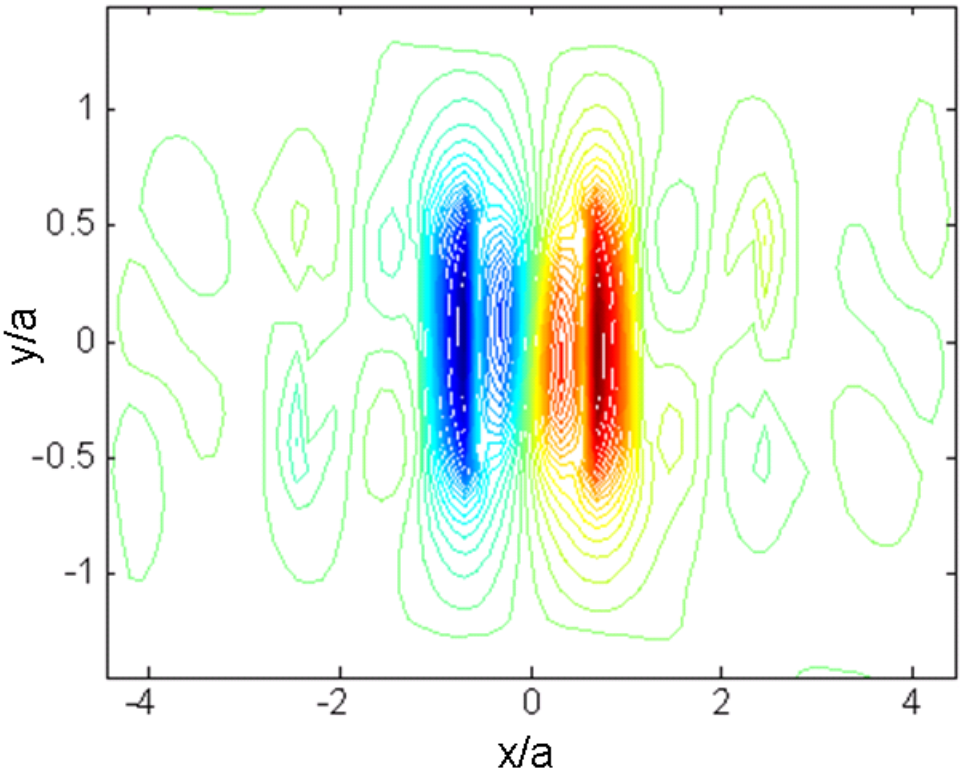

(b)

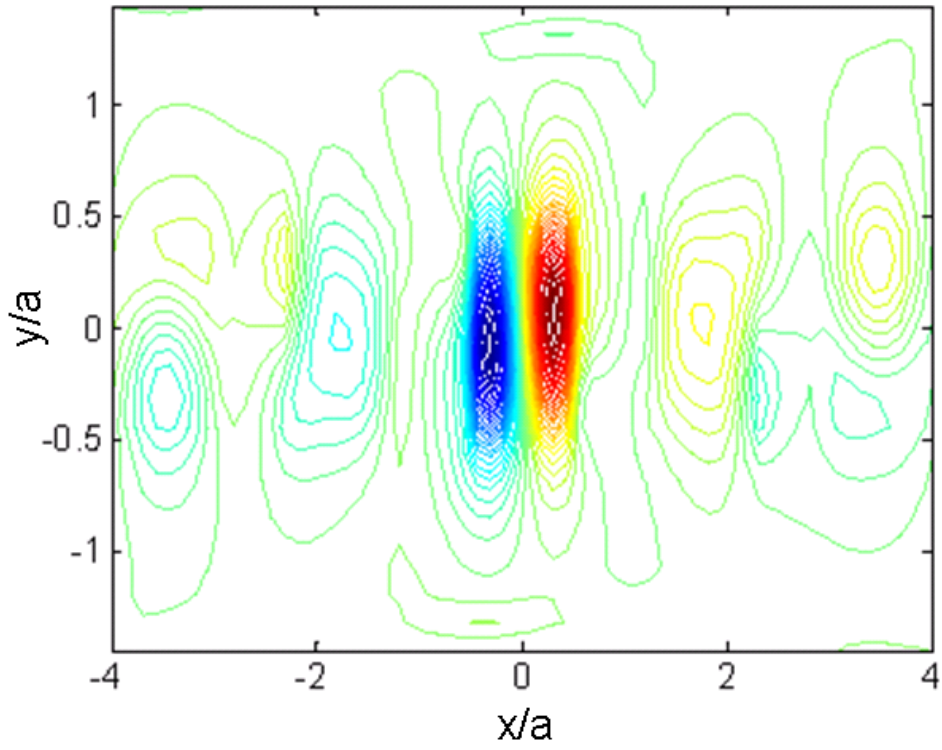

(c)

Figure 3.13 Cross-section of dominant field components of the next higher order Bloch mode for r=0.3a, t=a, n_{si}=3.48, a=410 nm at a/λ=0.266 (a) E_z (b) E_x (c) H_y.

Figure 3.14 shows the top view of the 3D-FDTD simulation of the PC slab waveguide. It is assumed that the unit cell is normalized (a=1 μm). To measure the speed of the light inside the waveguide, three time monitors are placed at the input (z_{in}=7 μm), middle (z=0 μm) and output (z_{out}=-7 μm) of the waveguide. Figure 3.15 displays the H_y signal that is evolving in time. The input signal is a single frequency Continuous Wave (CW). To measure the time that the signal spent to travel from input to output, the rise times at both locations were excluded. The time span is marked in Figure 3.15 and it is CT=300 μm; where C is the velocity of light in free space. Thus, ΔT, time required for the input signal to travel from z_{in}=7 μm to z_{out}=-7 μm is ΔT =1 psec. The speed of light inside the PC slab waveguide can be calculated as following:

$V=(z_{out}-z_{in})/\Delta T=14\times10^{-6}/1\times10^{-12}=14\times10^{6}$ m/sec

Our calculation shows that speed of light inside the PC slab waveguide is 14×10^{6} m/sec that is almost 5% of speed of light in free space, which is very slow.

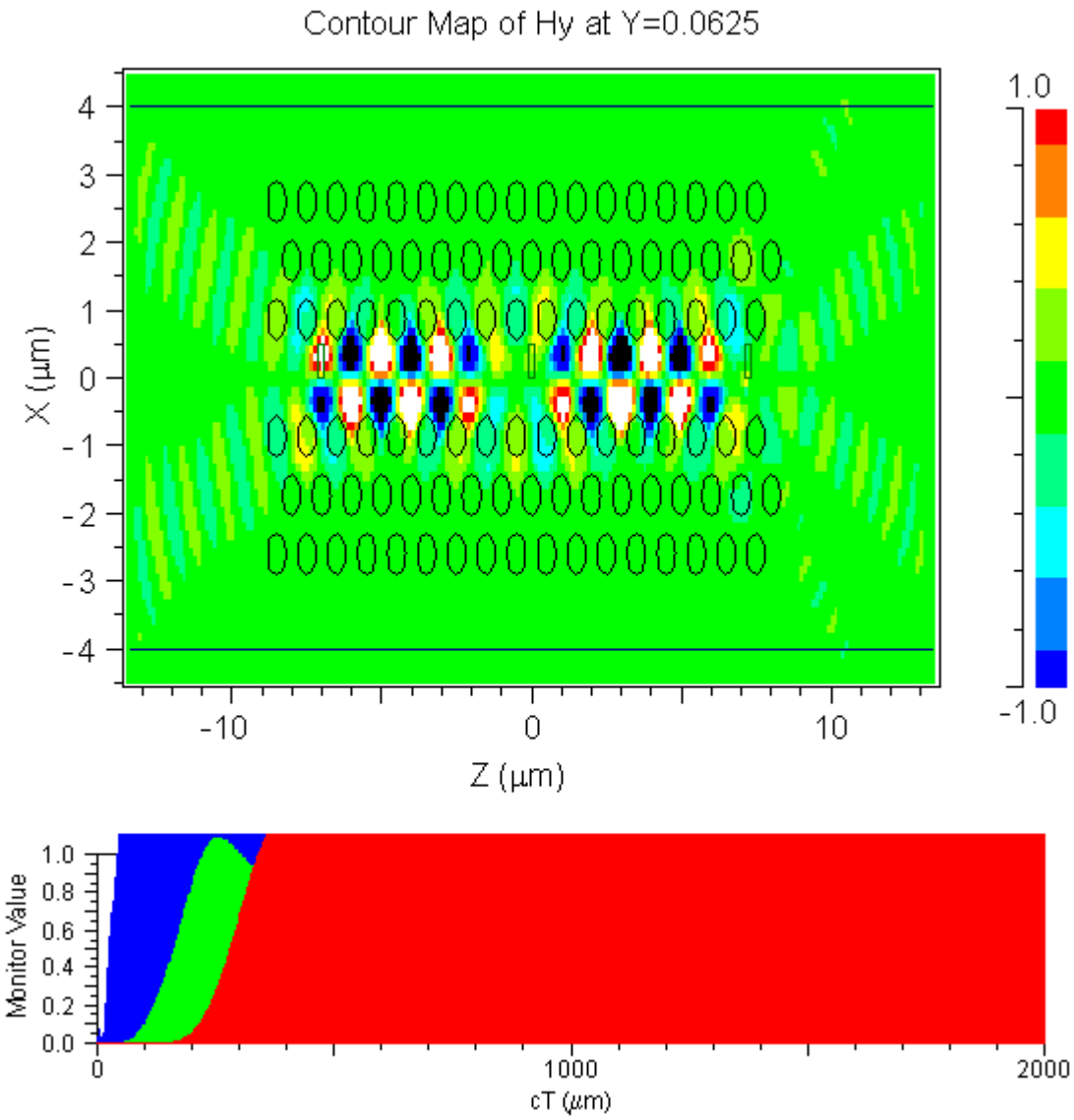

Figure 3.14 Top view of 3D-FDTD simulation of PC slab waveguide of next higher order mode (r=0.3a, t=a, n_{si}=3.48, a/λ=0.266).

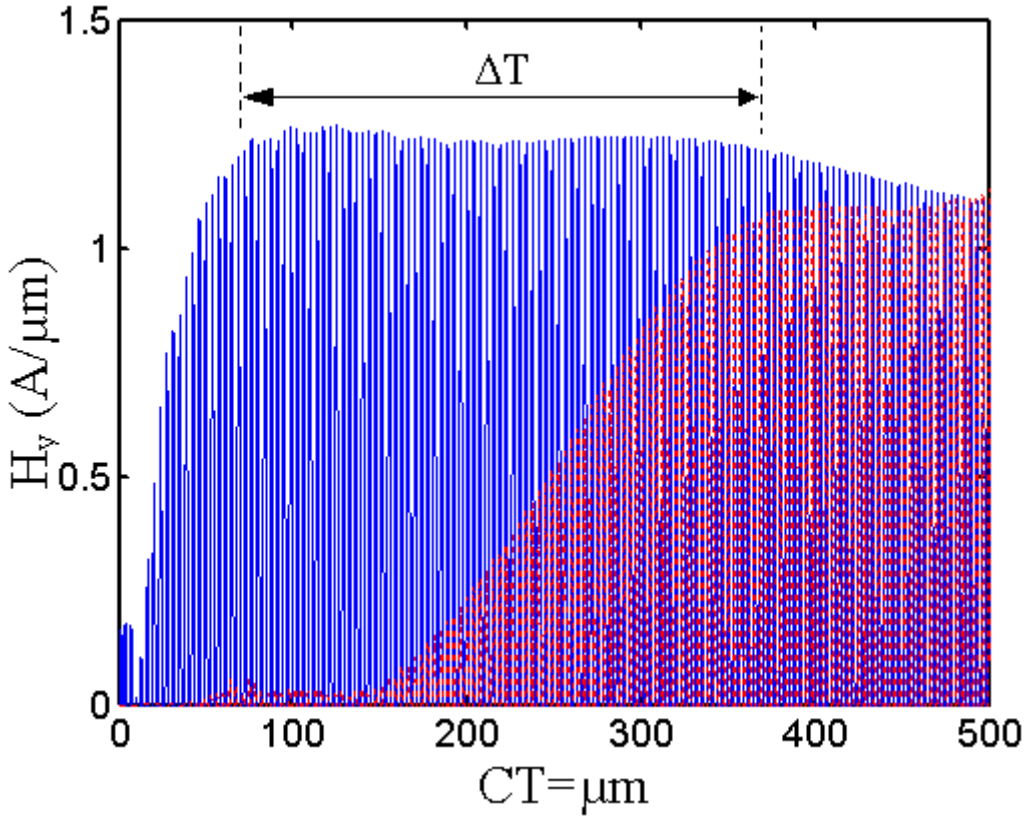

Figure 3.15 H_y signal in time at a/λ=0.266 (r=0.3a, t=a, n_{si}=3.48)

3.6 Square air holes PC slab structures

So far, only circular air hole PC structures were studied. The circular air hole PC structures are dominantly used in the optical community. It seems that fabricating small feature sized square air holes is more challenging, but for THz applications where feature sizes are big (> 25μm), square holes can be easily implemented utilizing standard photolithography. Even for optical application, by employing Electron Beam Lithography (EBL), the high precision small features (in the range of nanometers) can be implemented. So, square shaped air hole PC structures can be implemented for both optical and THz application. It is worthwhile to compare the electromagnetic field propagation in both structures. This section is devoted to comparing square and circular air holes PC slab structures.

3.6.1 Band diagram

Figure 3.16 shows a unit cell of a 2D triangular lattice circular hole PC. The dielectric constants of the hole, unit cell and radius of the circular hole are presented with ε_a, ε_b and ρ, respectively.

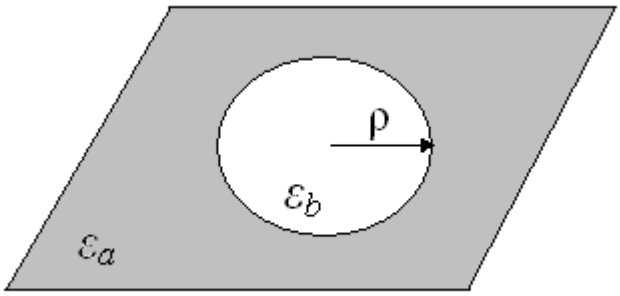

Figure 3.16 Unit cell of triangular lattice circular hole PC

The dielectric function *ε(r)* can be expanded as following:

$$\varepsilon(r) = \sum_G \varepsilon_G e^{-jG.r} \tag{3.4}$$

Using 2D Fourier transform, it can be easily shown that [109]:

$$\varepsilon_G = \varepsilon_b \Delta(G\rho) + (\varepsilon_b - \varepsilon_a)\frac{2\pi\rho^2}{A_U} \times \frac{J_1(G\rho)}{G\rho} \tag{3.5}$$

Where G is reciprocal lattice vector. A_U is the area of the unit cell. Function Δ is defined as following:

$$\Delta(x) = \begin{cases} 1 & x = 0 \\ 0 & x \neq 0 \end{cases} \tag{3.6}$$

At the center of reciprocal lattice where G=0

$$\lim_{x\to 0} \frac{J_1(x)}{x} = \frac{1}{2} \tag{3.7}$$

Thus,

$$\varepsilon_{00} = \varepsilon_b + (\varepsilon_b - \varepsilon_a)\frac{\pi\rho^2}{A_{WSC}} \tag{3.8}$$

By defining the filling factor as following:

$$f \equiv \frac{\pi\rho^2}{A_{WSC}}$$

Equation (3.8) can be simplified as following:

$$\varepsilon_{00} = \varepsilon_b + f(\varepsilon_b - \varepsilon_a) \tag{3.9}$$

Thus, the DC component of Fourier transform is proportional to the filling factor of the PC structure. Having noted that, in the process of changing the shape of the air holes in the PC structures, the filling factor must be kept constant in order for the band diagram to remain the same. Here, an example is presented to verify the above discussion. Starting from a square hole PC structure, PWEM analysis is carried out for the triangular lattice square PC slab with w=0.6a (width of square), t=0.8a and n_{si}=3.48, respectively. The band diagrams corresponding for the square hole PC slab's TE-like and TM-like polarizations are depicted by solid lines in Figures 3.17 (a) and (b), respectively. No bandgap is observed for the TE-like polarization. The normalized frequencies associated with the lower and upper edge of the bandgap of TM-like polarization are 0.238 and 0.33, respectively. The goal is to find the equivalent circular-shaped hole PC in terms of band diagram. Given the conclusion drawn from Equations (3.4)-(3.9), the radius of circle must be the average between w/2 and $\sqrt{w}/2$. The radius of the circular shape air hole is estimated as following:

$$r_{ave} = \alpha(1+\sqrt{2})w \qquad (3.10)$$

The PWEM can be employed to adjust the value of α. After several trial and error it is found that for α=0.47, the bandgap characteristics are the same for both circular and square shaped air holes PC. The band diagram corresponding to the circular hole PC are depicted by dots in Figure 3.17. They follow the graphs corresponding to the square hole PC slab very closely.

The band diagrams for a single defect line PC slab waveguide for both square and circular holes' TM-like polarization are calculated and plotted in Figure 3.18. The band diagrams of the square and circular hole PC slab waveguide are depicted by solid and dotted lines, respectively. The fundamental and next higher order Bloch modes lies within the frequency band of 0.247-0.278 and 0.281-0.282 for both structures.

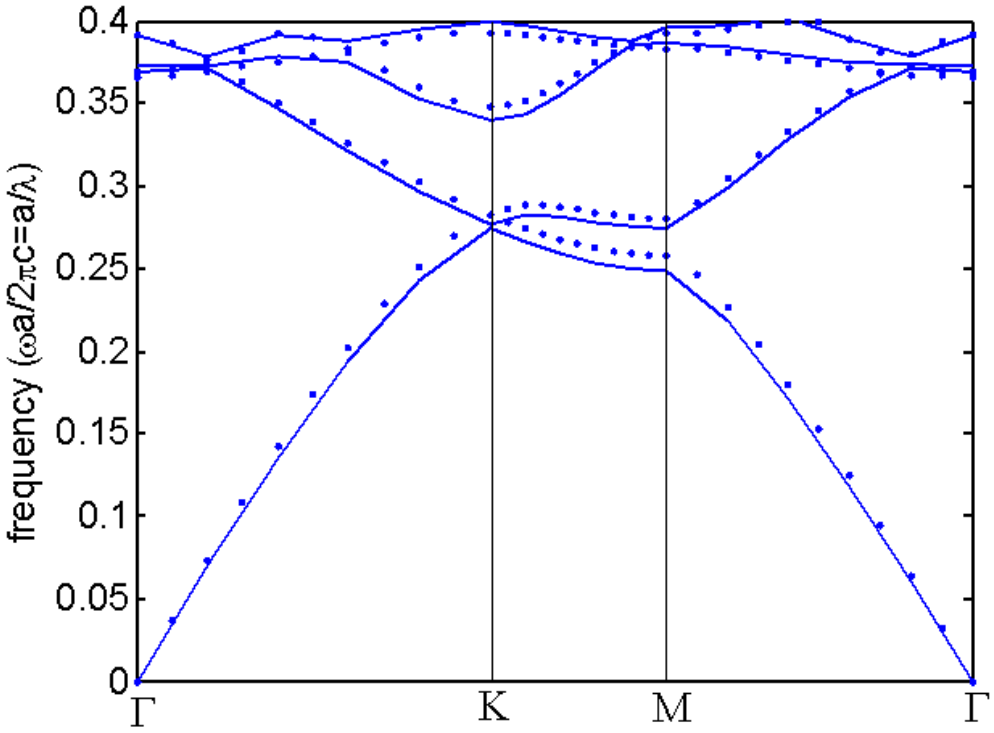

(a)

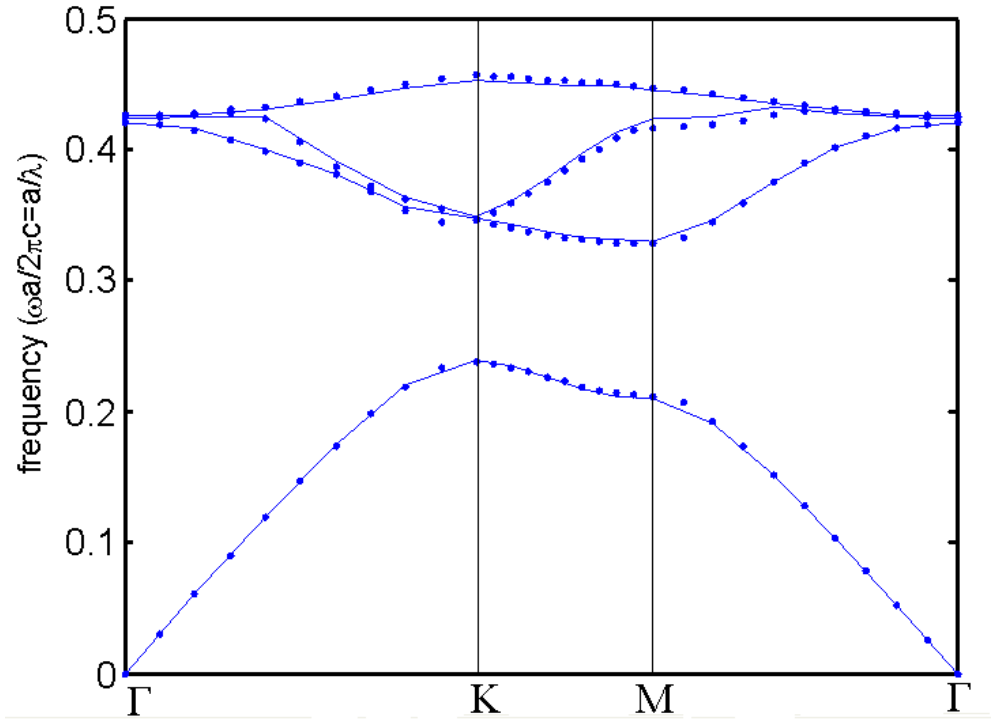

(b)

Figure 3.17 The band diagrams for square and circular hole PC slab with w=0.6a, t=0.8a, r=0.47*w(1+√2) (a) TE-like (b) TM-like polarizations.

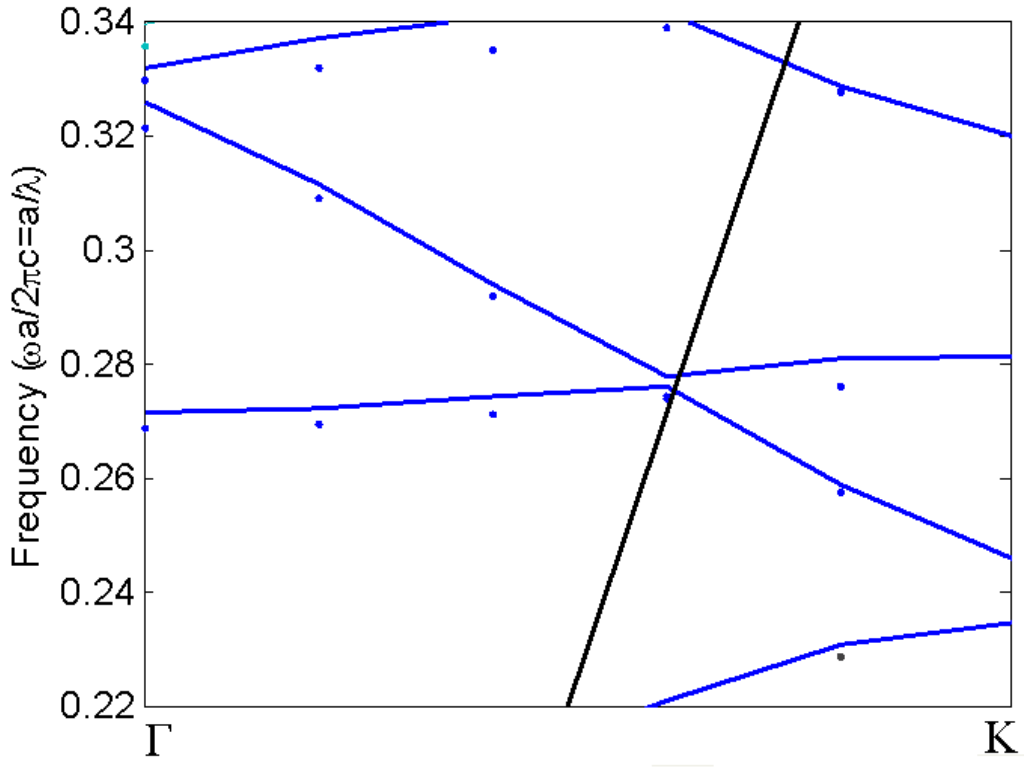

Figure 3.18 The band diagram for both square and circular hole single defect PC slab waveguide with w=0.6a, t=0.8a, r=0.47*w(1+√2) for TM-like wave.

In the band diagram calculation using the PWEM, it is assumed that the periodicity of the PC structure is extended to infinity. Yet, in practice there are only a finite number of unit cells in the structure. Studies conducted on finite PC structures indicate that the finiteness of the PC structure could lead to energy leakage in the bandgap [110]. Here, we have studied wave propagation within the frequency band of the bandgap for both square and circular hole PC slabs for the case that the PC slab is not extended to infinity. The PWEM analysis indicates that a TM-like wave bandgap exists within the normalized frequency band of 0.238-0.33. This means, no TM-like wave propagation inside the frequency band of bandgap is expected to be observed. The 3D-FDTD simulation was run for several frequencies inside the bandgap for both square and circular hole PC slab waveguides. Figures 3.19 (a) and (b) presents the 3D-FDTD contour map of the E_x and H_y components of the TM-like wave for a square PC with w=0.6a, t=0.8a and a=1 μm at a/λ=0.263 and y=0 plane. The input wave is a single frequency Guassian, the width of this Guassian beam is 5a. It is seen that the input wave has mostly

been reflected as a/λ=0.265 and lies inside the bandgap. On the other hand, the same graphs plotted for the circular hole PC slab waveguide ($r = \alpha(1+\sqrt{2})w$) (Figure 3.20) shows strong penetration of input wave inside the structure.

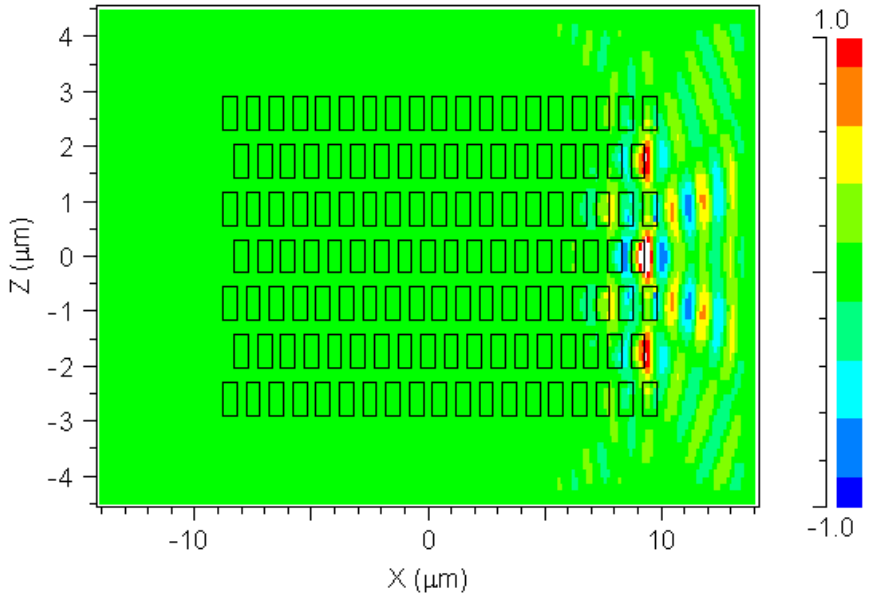

(a)

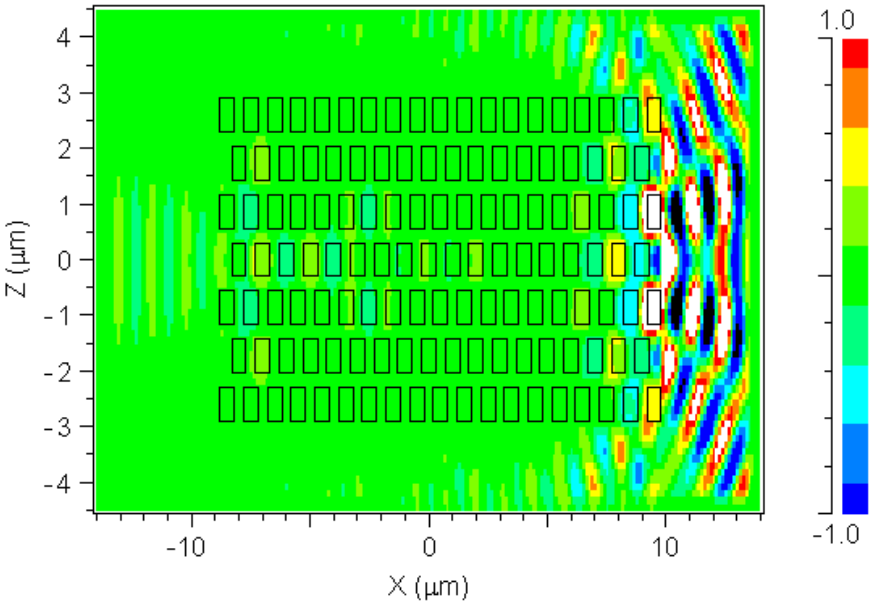

(b)

Figure 3.19 contour map of (a) E_x and (b) H_y for TM-like polarization of square hole PC slab waveguide with w=0.6a, t=0.8a, n_{si}=3.48, a=1 μm and a/λ=0.265.

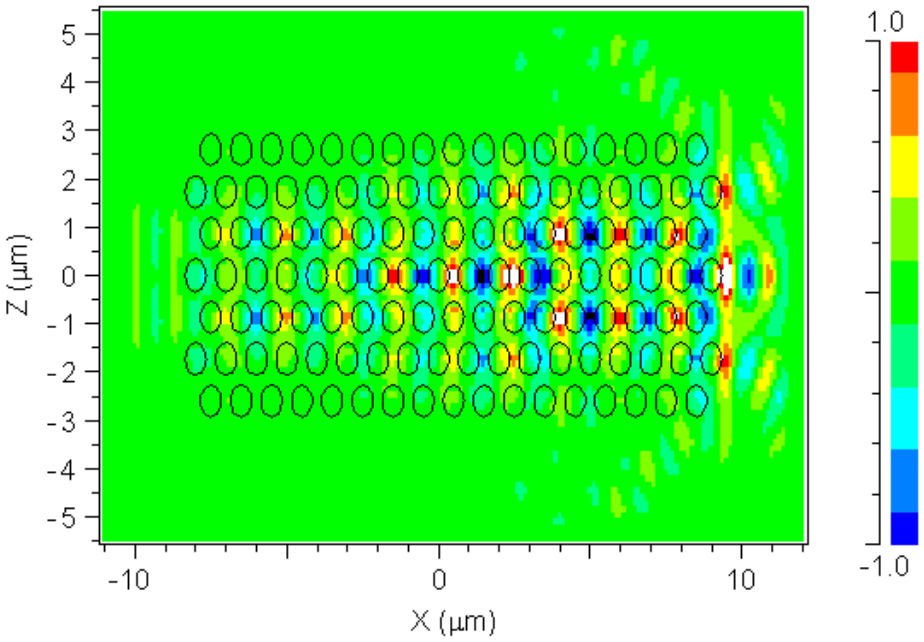

(a)

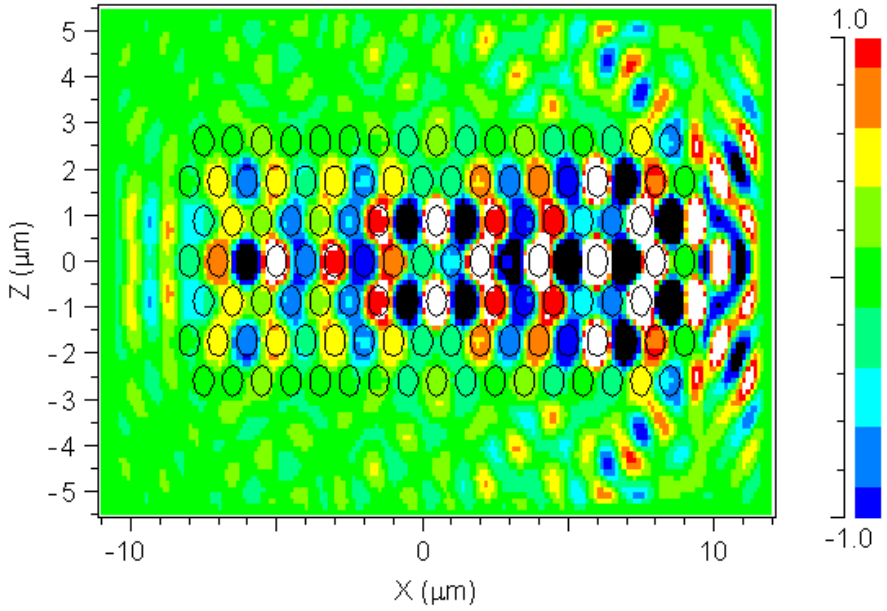

(b)

Figure 3.20 contour map of (a) E_x and (b) H_y for TM-like polarization of square hole PC slab waveguide with $r = \alpha(1+\sqrt{2})w$, t=0.8a, n_{si}=3.48 and a/λ=0.265.

To sweep the frequency within the bandgap and observe the behavior of finite square and circular hole PC slabs, a pulse in the time domain has been injected into the structure. Top view of the circular hole PC slab is shown in Figure 3.21 (a). The wave propagates in the z-direction. The central normalized frequency and time width of the pulse are 0.262 and λ/2. The spatial distribution of input is a Guassian beam, the width of the beam is the same as CW, 5a. Several time monitors are placed in the structure so that the time evolution of the signal at different locations can be recorded. By taking the Fourier transform of the time signals at the input and output, the frequency response of the structure can be obtained. Figure 3.21 (b) shows the normalized fourier transform of the output signal for both circular and square hole PC slabs. According to the PWEM, the bandgap lies in the frequency band of 0.238-0.33 for TM-like wave. In Figure 3.21 (b), the solid line corresponds to the square hole PC slab. It shows that there are some leakages around the lower edge of the bandgap, at the frequency of 0.238-0.25. Therefore, the bandgap obtained using this method lies within the frequency band of 0.25-0.33. In the same figure, the frequency response of the circular hole PC slab is plotted by a dotted line. Again the leakage is observed at lower edge of the bandgap, however, for the circular hole PC slab, the modes are extended from $a/\lambda=0.238$ to $a/\lambda=0.28$ which is a wide frequency band. They are placed within the frequency band of Bloch modes. Moreover, the upper edge of the bandgap is pushed up toward higher frequencies, while the upper edge of the bandgap is around $a/\lambda=0.385$. The presence of these leaky PC modes within the frequency band of the Bloch modes could change the wave propagation property in devices made of a PC slab. This issue has been addressed in the next chapter where the circular and square hole PC slab waveguide based polarization rotators are designed and simulated.

It is interesting to note that for the input wave injected in the x-direction, the distribution of the TM-like PC slab modes changes. Top view of the circular PC slab structure with wave propagating in the x-direction is sketched in Figure 3.22(a). Figure 3.22 (b) shows the spectrum of H_y component for both square and circular PC slabs with the same structural parameters as Figure 3.21. The only difference is that the wave is propagating in the x-direction as shown in Figure 3.22 (a). Almost no leaky PC slab mode is observed for the square hole PC slab. For the circular hole PC slab, the leaky PC slab

modes are extended from the lower edge of bandgap (a/λ=0.238) up to a/λ=0.24. Therefore, there are less leaky PC modes inside the bandgap.

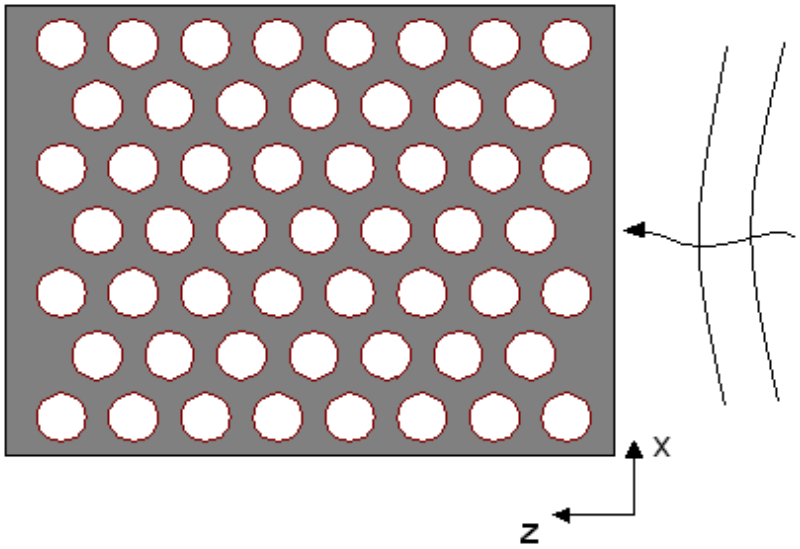

(a)

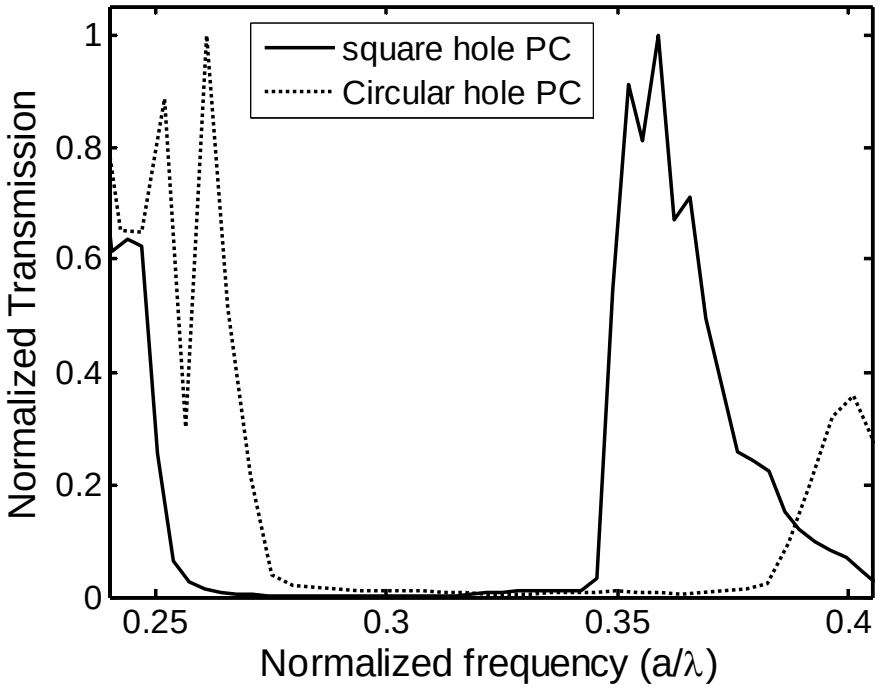

(b)

Figure 3.21 (a) Top view of circular hole PC slab (b) Spectrum of H_y for both square and circular hole PC slab obtained using 3D-FDTD simulations (t=0.8a, w=0.6a, r= , n_{si}=3.48).

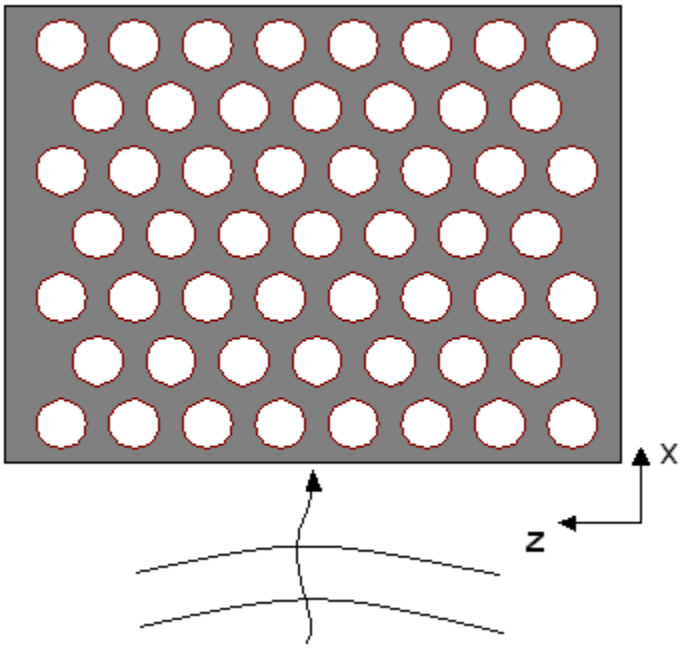

(a)

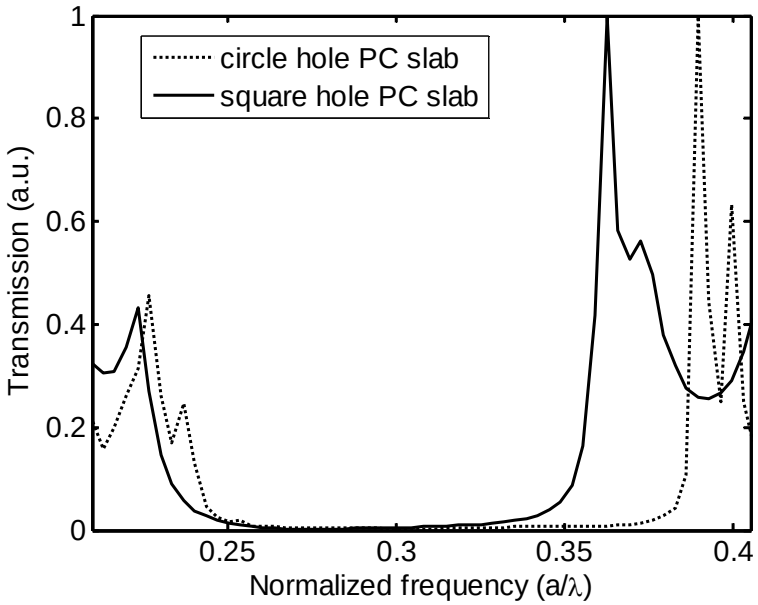

(b)

Figure 3.22 (a) Top view of circular hole PC slab (b) Spectrum of H_y for both square and circular hole PC slab obtained using 3D-FDTD simulations (t=0.8a, w=0.6a, r= , n_{si}=3.48)

Chapter 4

Design and analysis of PC slab waveguide based polarization rotator

4.1 Introduction

A polarization rotator structure is a crucial element of any optical integrated circuit. It is possible to utilize a polarization rotator to manipulate and control the polarization of a propagating wave. The passive polarization rotator structures introduced in Chapter 2 are mostly bulky. . Our goal is to propose and implement a compact planar integrated polarization rotator structure. Thus, the two main criteria are compactness and compatibility with planar PC circuit. Having these goals, we proposed an asymmetric loaded PC slab waveguide as it is the best candidate to meet both criteria. The PC slab waveguide is highly birefringent and compact; moreover, the fabrication process of the asymmetric loaded PC slab waveguide and integrated planar optical circuits are compatible.

The proposed structure consists of a single defect line PC slab waveguide. The geometrical asymmetry that is required to couple two orthogonal polarizations to each

other was introduced to the upper layer of the defect line. This upper layer is of the same material as the slab layer that has been etched asymmetrically with respect to z-axis (propagation direction). Power conversion reversal happens at half beat lengths along the line. In order to avoid power conversion reversal and synchronize the coupling, the upper layer that is a half beat in length is alternated on either side of the z-axis with the given period. Figure 4.1(a) is the sketch of the proposed structure, which is described as periodic asymmetric loaded PC slab waveguide. The PC based polarization rotator is expected to be very compact as opposed to periodic asymmetric loaded rib waveguide introduced in Chapter 2 [73], because of the large birefringence of the PC structures. The compact structure requires a smaller number of loading layers causing the radiation loss at the junctions between different sections to reduce.

Due to its compactness, the 3D-FDTD method can be employed to analyze and simulate its structure. For the preliminary and quick design an analytical method that provides the approximate values of the structural parameters is preferred. Coupled-mode theory is a robust and well-known method for the analysis of perturbed waveguide structures. Thus, the coupled-mode theory based on semi-vectorial modes was developed for these PC structures, however, the frequency band of the modes of the asymmetric loaded PC slab waveguide must be determined prior to the coupled mode analysis. The Plane Wave Expansion Method (PWEM) was employed for the modal analysis of the asymmetric loaded PC slab waveguide [49]. For the coupled mode analysis, the semi-vectorial modes of the asymmetric loaded PC slab waveguide, (illustrated in Figure 4.1 (b)), were calculated using the semi-vectorial Beam Propagation Method (BPM) of RSOFT, version 8.1. Coupled mode theory was employed to calculate the cross coupling between x-polarized and y-polarized waves. To simplify the problem for analytical calculations, instead of a circular hole PC pattern, a square hole PC pattern was employed. The coupled mode theory is an approximate method that provides an estimation of the structural parameters. The combination of the coupled mode theory and PWEM provides the frequency band over which low loss high efficiency polarization rotation is expected to be achieved.

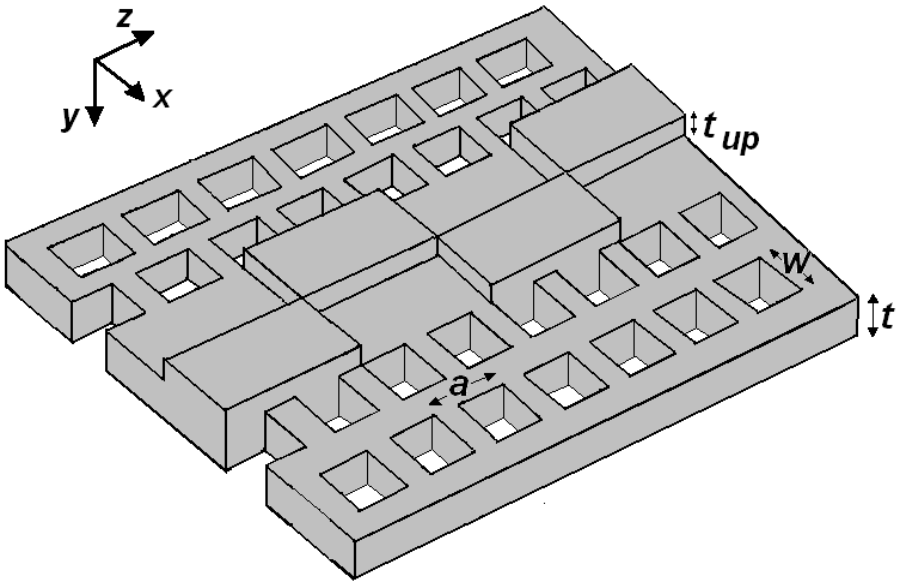

(a)

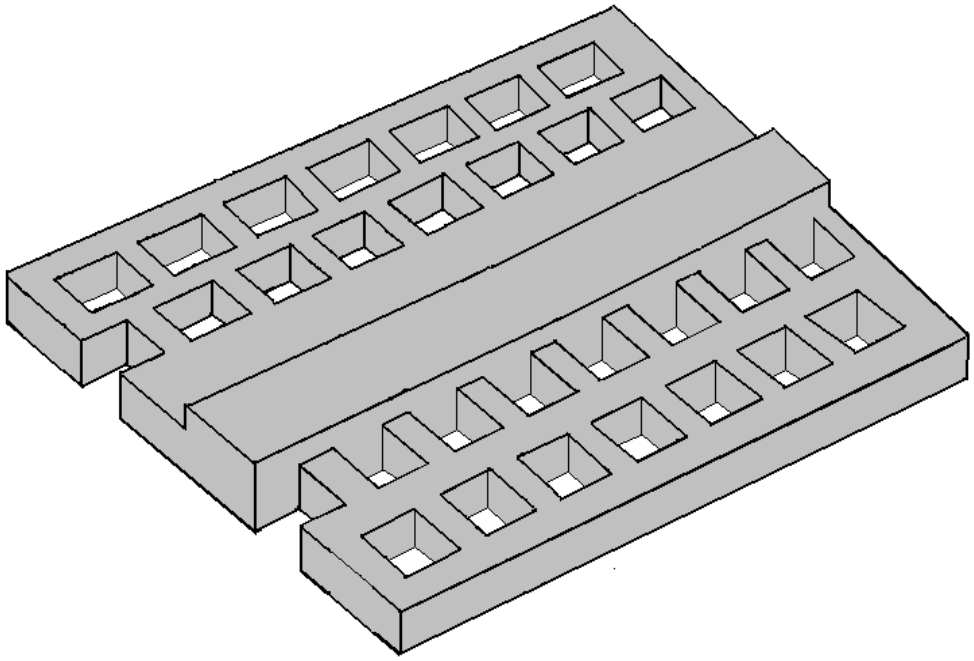

(b)

Figure 4.1. The sketch of (a) periodic asymmetric loaded triangular PC slab waveguide (b) asymmetric loaded PC slab waveguide.

Although, coupled mode theory presents a quick and efficient design methodology, the coupled-mode analysis for more complicated geometries such as a circular hole PC slab poses a tedious and error-prone process of discretization along the propagation direction. So, another design methodology based on vector-propagation characteristics of hybrid modes asymmetric loaded PC slab waveguide is proposed. It can be employed for any arbitrary shape PC slab structure. Hybrid mode analysis of an asymmetric loaded PC slab waveguide provides both the fast and slow hybrid modes of the structure. This allows the half-beat length to be calculated using equation (2.21). The vector-propagation characteristics of the hybrid modes of the asymmetric loaded PC slab waveguide were calculated using 3D-FDTD analysis combined with the Spatial Fourier Transform (SFT) of the electric field along the propagation direction. Both coupled-mode analysis and hybrid mode analysis lead to the same results for square shape PC slab waveguide based polarization rotator.

The design parameters were verified using coupled mode theory and hybrid mode analysis, and the polarization rotator structure was simulated using 3D-FDTD. Figure 4.2 presents the flow chart of the design. It shows the design consists of three main steps. In the first step, the operational frequency band must be determined using PWEM analysis. In this step, the thickness of the asymmetric loaded PC slab waveguide must be optimized to provide maximum frequency band over which highly efficient polarization conversion is expected to take place. In the second step, coupled mode theory is employed for preliminary design of the polarization rotator. The outputs of this step are the length of top loaded layers (half-beat length) and total number of top loaded layers. Finally, to verify the design parameters obtained using coupled mode theory the 3D-FDTD simulation is performed. Coupled mode theory was developed for simple hole geometries. For circular hole PC structure, another design methodology based on 3D-FDTD is developed which is shown by 2’ in the flow chart of the design. As it was explained before, 3D-FDTD analysis of asymmetric loaded PC slab waveguide combined with SFT is employed to obtain the vector-propagation characteristics of the hybrid modes of the structure. The accuracy of this method can be examined by 3D-FDTD simulation of the polarization rotator structure.

In section 4.2, the design methodology has been elaborated. The design and simulation results are presented in section 4.3.

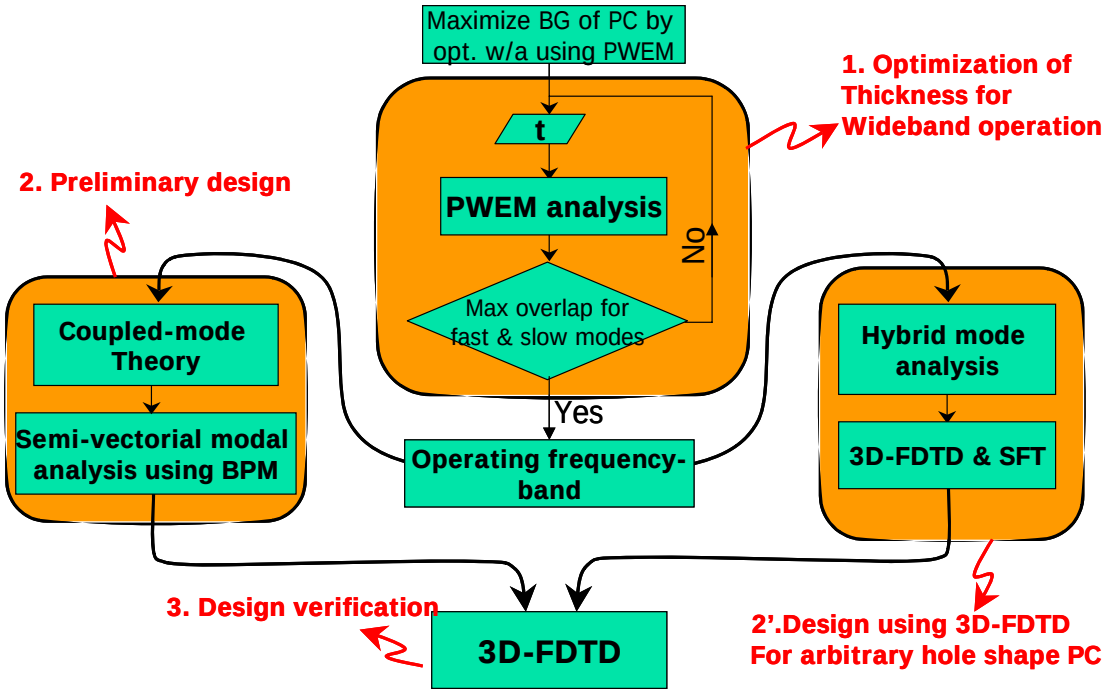

Figure 4.2 The flow chart of the design methodology of PC slab waveguide based polarization rotator

4.2 Theory

The schematic of the asymmetric square hole PC slab polarization rotator is shown in Figure 4.1(a). In this structure, the unit cell, the width of the square holes, the thicknesses of silicon PC slab waveguide and top loaded layer are represented by a, w, t and t_{up}. The top cladding layer is asymmetric with respect to the z-axis propagation direction and alternates periodically throughout the propagation direction to synchronize the coupling between the two polarizations.

The vector wave equation for the transverse electric field (x-y and z are the transverse and propagation directions) is given by [111]:

$$\frac{\partial^2 E_x}{\partial z^2} + \nabla_t^2 E_x + n^2 k^2 E_x = -\frac{\partial}{\partial x}\left(E_x \frac{1}{n^2}\frac{\partial n^2}{\partial x}\right) - \frac{\partial}{\partial x}\left(E_y \frac{1}{n^2}\frac{\partial n^2}{\partial y}\right) \qquad 4.1(a)$$

$$\frac{\partial^2 E_y}{\partial z^2} + \nabla_t^2 E_y + n^2 k^2 E_y = -\frac{\partial}{\partial y}\left(E_x \frac{1}{n^2}\frac{\partial n^2}{\partial x}\right) - \frac{\partial}{\partial y}\left(E_y \frac{1}{n^2}\frac{\partial n^2}{\partial y}\right) \qquad 4.2(b)$$

Where, n is the refractive index distribution of the waveguide and ∇_t^2 is the transverse differential operator defined as:

$$\nabla_t^2 = \frac{\partial^2}{\partial x^2} + \frac{\partial^2}{\partial y^2}$$

The vector properties manifest on the right hand side of equation (4.1.a), and equation (4.1.b), which indicates that the two orthogonal polarizations may be coupled to each other as a result of geometrical asymmetry.

As it was explained in the introduction, the two approaches, hybrid mode analysis of the asymmetric loaded PC slab waveguide, and coupled mode theory based on semi-vectorial modes were employed to design the polarization rotator structure. Both methods are explained in the following subsections.

4.2.1 Hybrid mode analysis using 3D-FDTD

The first approach to design a polarization rotator structure is to calculate the vector-propagation characteristics of the hybrid modes (fast and slow modes) for the asymmetric loaded PC slab waveguide (Figure 4.1 (b)). The half-beat length and the total number of the loaded layers can be calculated using equation (2.21). To obtain modal characteristics of the hybrid modes for the asymmetric loaded PC slab waveguide, the 3D-FDTD method is employed. The propagation constants of the x-polarized and y-polarized waves are extracted from the 3D-FDTD simulation results using SFT of the electric field along the propagation direction. First, the frequency band over which slow and fast modes are guided must be determined so that 3D-FDTD simulation could be performed over the aforementioned frequency band. PWEM is then employed to obtain the band diagram of the asymmetric loaded PC slab waveguide.

To calculate the birefringence of the structure, the effective frequency-dependent index of refraction of the hybrid modes is calculated. To obtain the aforementioned data,

the accurate dispersion analysis is carried out. The analysis is based on the SFT of the electromagnetic field distribution in the PC slab waveguide along the propagation direction

To employ the SFT, it is assumed that the electromagnetic field in the PC slab waveguide can be expressed as a modal expansion at the normal plane, as following [98]:

$$E_{\omega}(x,y,z) = \sum_{n,m} E_{n,m,\omega} e^{j\beta_{n,m,\omega} z} \tag{4.3}$$

Where $E_{n,m,\omega}$ and $\beta_{n,m,\omega}$ represent the electric field component and the propagation constant of the $(n,m)^{th}$ mode at frequency ω. The peaks of the SFT spectrum describe the propagating modes of the structure. These peaks are independent of the location, (x_0 , y_0) and the electromagnetic field components. The effective refractive indices of the modes can be determined by locating these peaks.

Having determined the effective refractive indices of the fast and slow modes, L_{π} can be calculated as well as the total number of top loaded layers. The design methodology presented in this subsection requires finding the vector-propagation characteristics of the hybrid modes of an asymmetric loaded PC slab waveguide. It is a very general methodology and can be extended to any air hole geometry of a PC slab structure. On the other hand, to coupled-mode theory that is more efficient for simple air hole geometry PC structures such as a square hole PC slab based polarization rotator. In the following subsection, coupled-mode theory based on semi-vectorial modes of the structure is presented.

4.2.2 Coupled-mode theory

Huang and Mao employed similar coupled mode theory based on the scalar modes to analyze polarization conversion in a periodic loaded rib waveguide [80]. In a PC slab waveguide, the propagation characteristics strongly depend on the polarization of the propagating wave leading to a large birefringence [71]. Yet, the scalar modal analysis completely ignores the polarization dependence of the wave propagation, making, it too simplified to represent the wave propagation inside a PC slab waveguide. Here, a coupled mode theory based on semi-vectorial modes of a PC structure was developed to analyze the asymmetric loaded PC slab waveguide. Using the semi-vectorial modal analysis, the

polarization dependence of wave propagation has been partially taken into account, allowing the coupling between the two x-polarized and y-polarized waves to be modeled more accurately using coupled mode analysis.

In a PC structure, the cross-section varies along the propagation direction within a one unit cell. Employing square holes instead of circular holes simplifies the problem of modeling such structures. The PC lattice is triangular, Figure 4.3, illustrates the unit cell can be divided into two regions with designated coupling coefficients. The problem boils down to calculating the coupling coefficients for regions 1 and 2. A semi-vectorial BPM (BPM package of RSOFT) was employed to calculate the semi-vectorial modes of the asymmetric PC slab waveguide shown in Figure 4.1(b). The output of the BPM analysis, the profile and and the propagation constants of the x-polarized and y-polarized modes of the asymmetric loaded PC slab waveguide were used to calculate the coupling coefficients of the x-polarized and y-polarized waves. Assuming that the profile of the total transverse field in the asymmetric loaded PC slab waveguide is represented as follows:

$$E = E_x\hat{x} + E_y\hat{y} \quad = a_x(z)e_x(x,y)e^{-j\beta_x z} + a_y(z)e_y(x,y)e^{-j\beta_y z} \quad , \qquad (4.4)$$

Where $e_x(x,y)e^{-j\beta_x z}$ and $e_y(x,y)e^{-j\beta_y z}$ are x- and y-components of electric field of the semi-vectorial solution of wave equation for x-polarized and y-polarized waves, respectively. β_x and β_y are propagation constants along x and y directions. . In order to keep the coupled mode equations simple, only the first order Bragg modes were employed. In modal analysis carried out using SFT analysis, it is observed that the amplitudes of higher order bragg modes are 3-order of magnitude less than that of first-order bragg modes; thus, their contribution in coupled mode equation is negligible. Substituting equation (4.4) into equation (4.1) and multiplying both side of equation (4.1.a), and equation (4.1.b) by $e^{j\beta_x z}$ and $e^{j\beta_y z}$, then assuming that the amplitude of the field are slowly varying along z-direction (propagation direction), the following equation has been obtained:

$$-j2\beta_x e_x \frac{da_x(z)}{dz} + a_x(z)\nabla_t^2 e_x + n^2 k^2 a_x(z) e_x - \beta_x^2 a_x(z) e_x = -a_x(z)\frac{\partial}{\partial x}(e_x \frac{1}{n^2}\frac{\partial n^2}{\partial x}) - a_y(z) e^{-j\Delta z}\frac{\partial}{\partial x}(e_y \frac{1}{n^2}\frac{\partial n^2}{\partial y}) \quad (4.5.a)$$

$$-j2\beta_y e_y \frac{da_y(z)}{dz} + a_y(z)\nabla_t^2 e_y + n^2 k^2 a_y(z) e_y - \beta_y^2 a_y(z) e_y = -a_y(z)\frac{\partial}{\partial y}(e_y \frac{1}{n^2}\frac{\partial n^2}{\partial y}) - a_x(z) e^{j\Delta z}\frac{\partial}{\partial y}(e_x \frac{1}{n^2}\frac{\partial n^2}{\partial x}) \quad (4.5.b)$$

Where: $\Delta = \beta_y - \beta_x$,

By invoking the following assumption:

$$\nabla_t^2 e_x + (n^2 k^2 - \beta_{ave}^2) e_x = 0$$
$$\nabla_t^2 e_y + (n^2 k^2 - \beta_{ave}^2) e_y = 0 \quad , \quad (4.6)$$

Where, $\beta_{ave} = \frac{\beta_x + \beta_y}{2}$,

A simplified form of equation (4.5) is obtained:

$$-j2\beta_x e_x \frac{da_x(z)}{dz} + (\beta_{ave}^2 - \beta_x^2) a_x(z) e_x = -a_x(z)\frac{\partial}{\partial x}(e_x \frac{1}{n^2}\frac{\partial n^2}{\partial x}) - a_y(z) e^{-j\Delta z}\frac{\partial}{\partial x}(e_y \frac{1}{n^2}\frac{\partial n^2}{\partial y}) \quad (4.7.a)$$

$$-j2\beta_y e_y \frac{da_y(z)}{dz} + (\beta_{ave}^2 - \beta_y^2) a_y(z) e_y = -a_y(z)\frac{\partial}{\partial y}(e_y \frac{1}{n^2}\frac{\partial n^2}{\partial y}) - a_x(z) e^{j\Delta z}\frac{\partial}{\partial y}(e_x \frac{1}{n^2}\frac{\partial n^2}{\partial x}) \quad (4.7.b)$$

Multiplying both sides of equation (4.7.a), and equation (4.7.b) by e_x^* and e_y^* (*-conjugate), and integrating over the cross-section, the following coupled mode equations are obtained:

$$\frac{da_x(z)}{dz} = -j\kappa_{xx} a_x(z) - j\kappa_{xy} a_y(z)$$
$$\frac{da_y(z)}{dz} = -j\kappa_{yy} a_y(z) - j\kappa_{yx} a_x(z) \quad (4.8)$$

Where:

$$\kappa_{xx} = \frac{(\beta_{ave}^2 - \beta_x^2)\iint e_x^*.e_x dxdy + \iint e_x^*.\frac{\partial}{\partial x}(e_x \frac{1}{n^2}\frac{\partial n^2}{\partial x})dxdy}{2\beta_x \iint e_x^*.e_x dxdy} \quad (4.9.a)$$

$$\kappa_{xy} = \frac{e^{-j\Delta z}\iint e_x^*.\frac{\partial}{\partial x}(e_y \frac{1}{n^2}\frac{\partial n^2}{\partial y})dxdy}{2\beta_x \iint e_x^*.e_x dxdy} \quad (4.9.b)$$

$$\kappa_{yy} = \frac{(\beta_{ave}^2 - \beta_y^2)\iint e_y^*.e_y dxdy + \iint e_y^*.\frac{\partial}{\partial y}(e_y \frac{1}{n^2}\frac{\partial n^2}{\partial y})dxdy}{2\beta_y \iint e_y^*.e_y dxdy} \quad (4.9.c)$$

$$\kappa_{yx} = \frac{e^{j\Delta z}\iint e_y^*.\frac{\partial}{\partial y}(e_x \frac{1}{n^2}\frac{\partial n^2}{\partial x})dxdy}{2\beta_y \iint e_y^*.e_y dxdy} \quad (4.9.d)$$

κ_{xx} and κ_{yy} are the self-coupling coefficients; whereas, κ_{xy} and κ_{yx} refer to the cross-coupling coefficients. In equation (4.9.a), and equation (4.9.c), we have noted that the second terms are negligible in comparison with the first terms. The coupling coefficients must be solved for both regions 1 and 2 (see Figure 4.3), using equation (4.9). The distribution of the electric fields in both regions is the same. Where as, the refractive index profile is different as depicted in Figure 4.3 leading to different values of coupling coefficients for regions 1 and 2. If the cross-coupling coefficients in both regions were assumed to be equal (κ_{xy}= κ_{yx}= κ), the coupled-mode equations could be solved analytically as presented in equation (4.10) below [80]. Nonetheless, numerical methods could be easily implemented for general cases where the cross-coupling coefficients were not equal. Given the exact analytical solution as *A(z)=MA(0)*, where *A* is a column vector for coefficients a_x and a_y. The transfer matrix (*M*) is expressed as follows:

$$M_{i\pm} = \begin{pmatrix} \cos(\Omega_i z_i) - j\cos(\varphi_i/2)\sin(\Omega_i z_i) & \mp j\sin(\varphi_i/2)\sin(\Omega_i z_i) \\ \mp j\sin(\varphi_i/2)\sin(\Omega_i z_i) & \cos(\Omega_i z_i) + j\cos(\varphi_i/2)\sin(\Omega_i z_i) \end{pmatrix} \quad i = 1,2 \quad (4.10)$$

$$\Omega_i = \sqrt{\delta_i^2 + \kappa_i^2}$$
$$\delta_i = \frac{\kappa_{xxi} - \kappa_{yyi}}{2} \qquad (4.11)$$
$$\tan(\varphi_i / 2) = \frac{\kappa_i}{\delta_i}$$

The ± signs correspond to the alternative sections of the periodic loading. z_1 and z_2 are the length of regions 1 and 2 shown in Figure 4.3. Assuming that w is the width of a square hole, z_1 and z_2 are determined as following:

$z_1=a-w$ (4.12.a)

$z_2=w$ (4.12.b)

Having set M_1 and M_2 as the transfer matrix of regions 1 and 2, the transfer matrix for one unit cell is obtained:

$M_{\pm}=M_{1\pm}.M_{2\pm}$, (4.13)

The loading period or half-beat length can be approximated as follows:

$$L_\pi \approx \frac{\pi}{\Omega_1 + \Omega_2} \quad , \qquad (4.14)$$

Thus, the length of one top silicon brick is L_π and the top cladding layer alternates periodically throughout the propagation length.

The simulation results revealed that for our structure, $|k_{xy}| \approx |k_{yx}|$ and $k_{xy} \approx k_{yx}^*$, where the imaginary parts were very small. The numerical and analytical solutions of the coupled mode theory equations (4.8.a) and (4.8.b), give us almost the same results. From equation (4.14) we calculated the preliminary value of the loading period before employing the numerical method to solve the coupled mode equation, using equation (4.8).

In next section, first the band structure of the asymmetric loaded PC slab waveguide is calculated using PWEM to determine the operating frequency band for the polarization rotator.

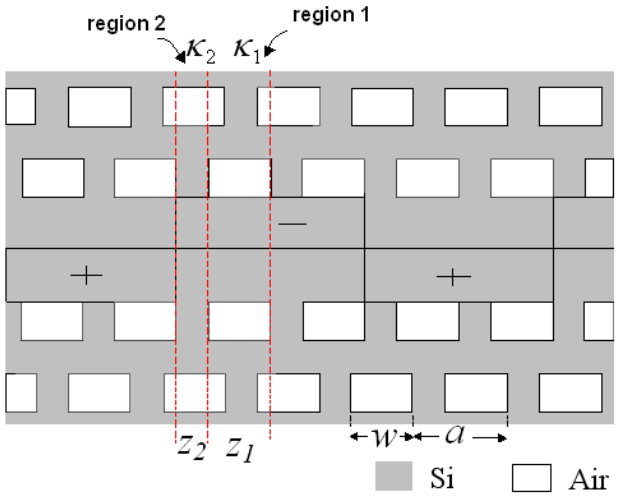

Figure 4.3. Top view of the asymmetrically loaded PC based polarization rotator. The top cover layer is marked by the dark solid line in the figure. κ_1 and κ_2 represent the cross-coupling coefficient for regions 1 and 2 inside a unit cell.

4.3 Design of the polarization rotator

In this section the results of the design using both coupled mode theory and hybrid mode analysis are presented.

4.3.1 Design of the polarization rotator using 3D-FDTD modal analysis

4.3.1.1 PWEM analysis

The first step in the design of the polarization rotator structure is to calculate the frequency band over which lossless propagation takes place for both x-polarized and y-polarized waves. Then we proceed with the design using both hybrid mode analysis and coupled mode theory within the aforementioned frequency band. The asymmetric loaded PC slab waveguide shown in Figure 4.1(b) was first simulated using PWEM to obtain the band diagram and the frequency band of the modes. As it is was mentioned in Chapter 3, the thickness of the PC slab structure plays an important role on the polarization dependent guiding. It is possible to obtain maximum overlap between x-polarized and y-polarized waves by optimizing the thickness of the PC slab waveguide. We have employed the design methodology presented in Chapter 3 to design the thickness of the asymmetric loaded PC slab waveguide.

Figure 4.4(a) shows the super-cell for the asymmetric loaded triangular PC slab waveguide. By including several unit cells in the horizontal plane, the defect lines in the super-lattice structure are isolated. In PWEM analysis, the definition of the TE-like and TM-like waves is based on the symmetry planes of the modes. The dominant components of TM-like mode (H_y, E_z, E_x) and the non-dominant components (E_y, H_z, H_x) have even and odd symmetry w.r.t. y=0 plane, respectively. Similarly, the dominant components of TE-like mode (E_y, H_z, H_x) and the non-dominant components (H_y, E_z, E_x) have even and odd symmetry to y=0 plane.

The thickness of the top loaded layer, t_{up}, is an important design parameter. Heuristically speaking, the larger the upper layer thickness is, the stronger the geometrical asymmetry is, leading to a more compact device. To comply with the fabrication constrains, the thickness of the top loaded layer is restricted to t_{up}=0.2a. The importance of this parameter has been assessed thoroughly in the next section.

To find the appropriate thickness, the design methodology presented in Chapter 3 is employed. The band diagrams for two different slab thicknesses t=0.6a and t=0.8a are obtained by PWEM and plotted in Figures 4.4(b) and (c). The thickness of the top loaded layer, the width of the PC squares and the refractive index of silicon are t_{up}=0.2a, w=0.6 and n_{si}=3.48, respectively. There are two modes depicted by dotted and solid lines. The mode graphed by the dotted line resembles an index-guided mode except for the mini-stop band observed at the zone boundary. We will call it an index-guided mode. The other mode depicted by solid line will be called Bloch mode. The index-guided mode is considered to be a y-polarized wave for which the dominant electric field component is in y-direction. On the other hand, the Bloch mode is considered x-polarized wave. For t=0.6a, the index-guided mode crosses the Bloch mode and is folded back at the zone boundary at a/λ=0.28. The Bloch mode touches the zone boundary (K) at a/λ=0.259 and crosses the TE-like PC slab modes at a/λ=0.274. Since the index-guided mode and Bloch mode cross each other, the difference between the effective refractive indices of the two modes, which is proportional to 1/Lπ, varies with frequency significantly. Thus, the polarization converter made of a PC slab with t=0.6a is expected to be narrow band.

In Figure 4.4(b), a mini-stop band (MSB) is observed around normalized frequency of a/λ=0.266. Note that the MSB observed in the band diagram calculation is

real. 3D-FDTD simulation of asymmetric loaded PC slab waveguide verifies the presence of MSB within a very narrow frequency band around $a/\lambda=0.266$ where the propagating wave experiences a huge loss. Further details of MSB can be found in [112], where it is shown that two modes with same symmetry and different orders anti-cross each other, when they obey the first-order Bragg condition: $\beta_s+\beta_f=2\pi/a$, giving rise to a MSB.

On the other hand, by increasing the thickness of the slab to t=0.8a, the index-guided mode has been pushed down to the lower frequencies. The index-guided mode depicted by a dotted line in Figure 4.4(c) has folded back at the zone boundary at $a/\lambda=0.243$. Within the frequency band of the Bloch mode, 0.257-0.267, the two bands are parallel, making the variation of the difference between the effective indices of the two modes and L_π with frequency negligible. In this diagram, the index-guided and Bloch modes also correspond to the fast and slow modes. At a normalized frequency of $a/\lambda=0.267$, the Bloch mode crosses the TE-like PC slab mode. The band diagram obtained by PWEM also is verified by 3D-FDTD simulation of asymmetric loaded PC slab waveguide (Figure 4.1(b)). For example, the cross-section of the electromagnetic field are plotted in Figure 4.5 at $a/\lambda=0.267$ to show not only the guided mode components, but also the presence of a TE-like PC slab mode. In 3D-FDTD simulations, the central normalized frequency of $a/\lambda=0.265$ is assigned to f=600 GHz resulting in the unit cell size of a=132.5 μm. The cross-section of E_x, E_y, H_x and H_y components for the TE-like input at $a/\lambda=0.267$ (f=604.5 GHz) are plotted in Figure 4.5. The graphs verify the presence of PC slab modes. The E_y and H_x components of the PC slab modes own even symmetry w.r.t. y=0 plane as opposed to the E_x and H_y components that have odd symmetry. Therefore, PC slab modes are TE-like, verifying the PWEM analysis. Moreover, the field distribution inside the defect line indicates that E_y and H_x are the dominant components of the electric and magnetic field, respectively, indicating that the TE-like wave at the input excites the y-polarized wave. All four components of the y-polarized mode have even symmetry with respect to y=0 and x=0 planes; although, the minor components of input wave, TE-like, (E_x and H_y) have odd symmetry w.r.t y=0 plane. Thus, TE-like input wave has evolved into the mode of the asymmetric loaded PC slab waveguide.

By further increasing the thickness of the PC slab waveguide, higher order modes will be pushed down inside the bandgap, which is not suitable for our application. Having compared the band diagram for t=0.6a and t=0.8a, it is seen that t=0.8a suits better for the polarization conversion application.

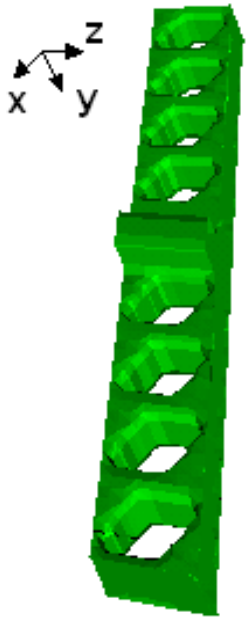

(a)

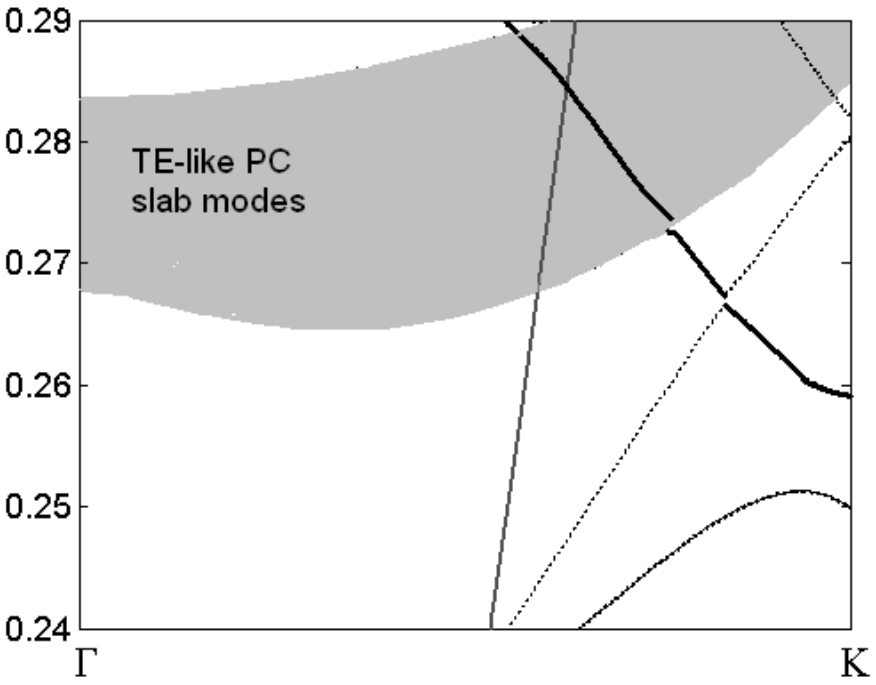

(b)

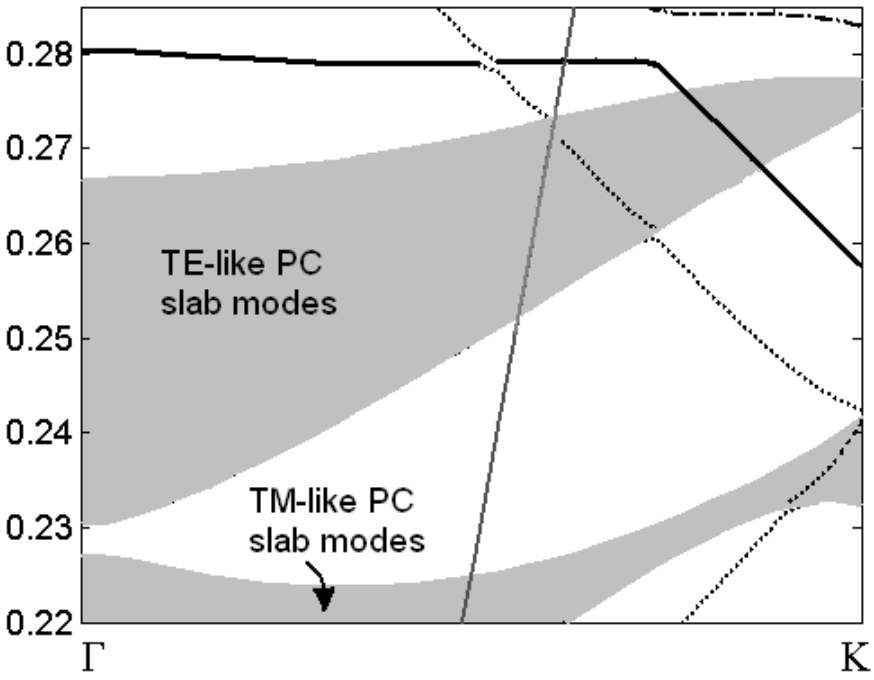

(c)

Figure 4.4 (a) The super cell of the asymmetric loaded PC slab waveguide for PWEM analysis. The band diagram for the asymmetric loaded PC slab waveguide obtained by PWEM for (b) t=0.6a, t_{up}=0.2a and w=0.6a (c) t=0.8a, t_{up}=0.2a and w=0.6a.

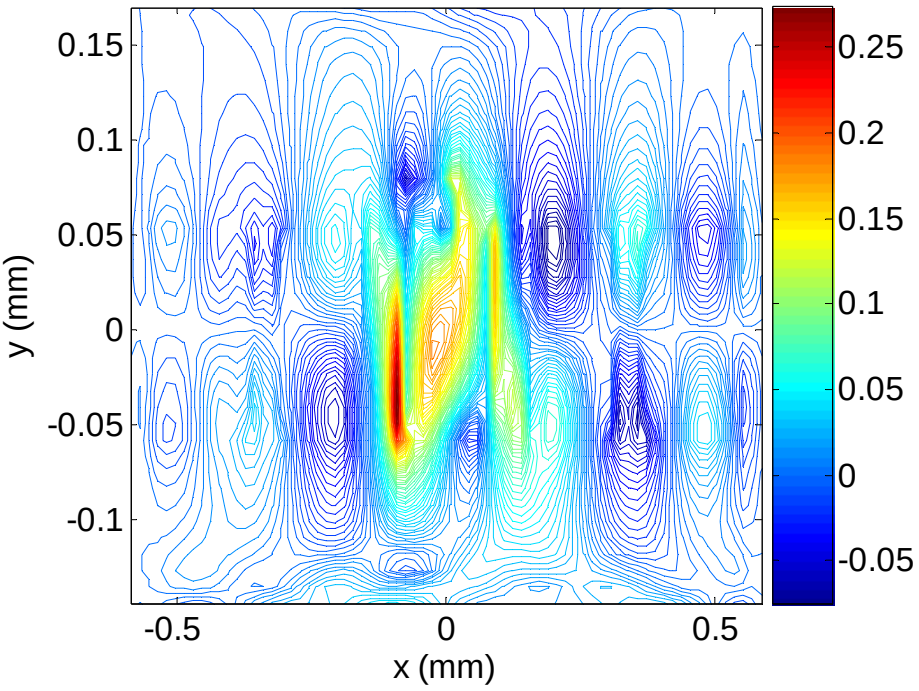
0.15
0.1
0.05
0
-0.05
-0.1
y (mm)
-0.5
0
0.5
x (mm)
0.25
0.2
0.15
0.1
0.05
0
-0.05

(a)

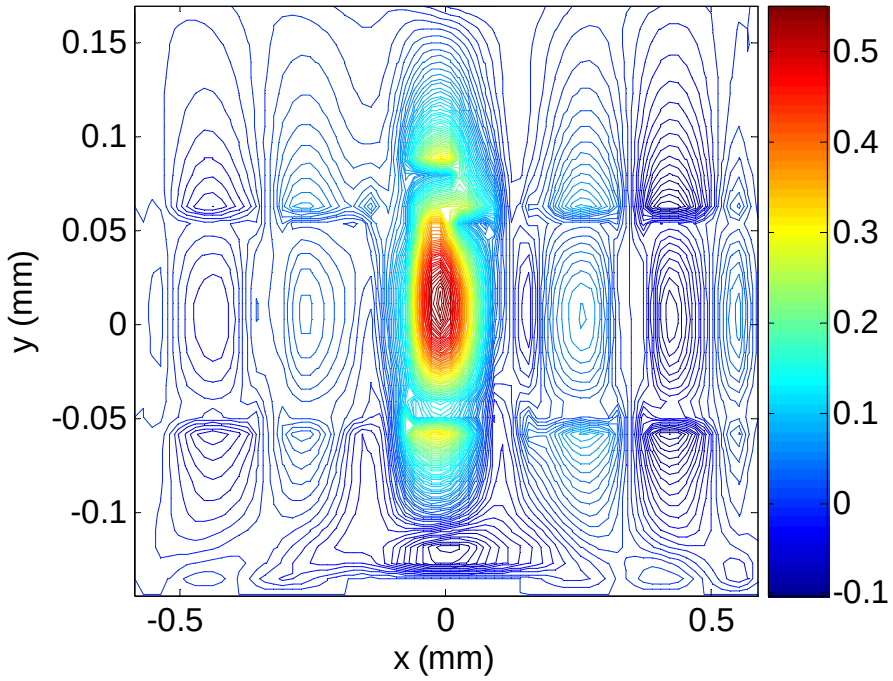
0.15
0.1
0.05
0
-0.05
-0.1
y (mm)
-0.5
0
0.5
x (mm)
0.5
0.4
0.3
0.2
0.1
0
-0.1

(b)

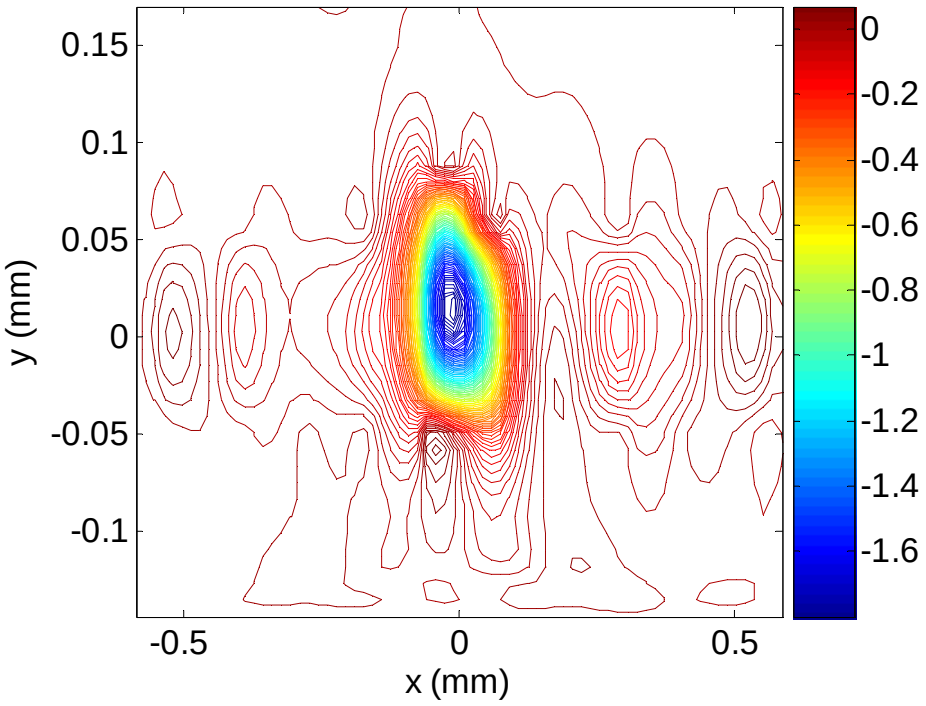

(c)

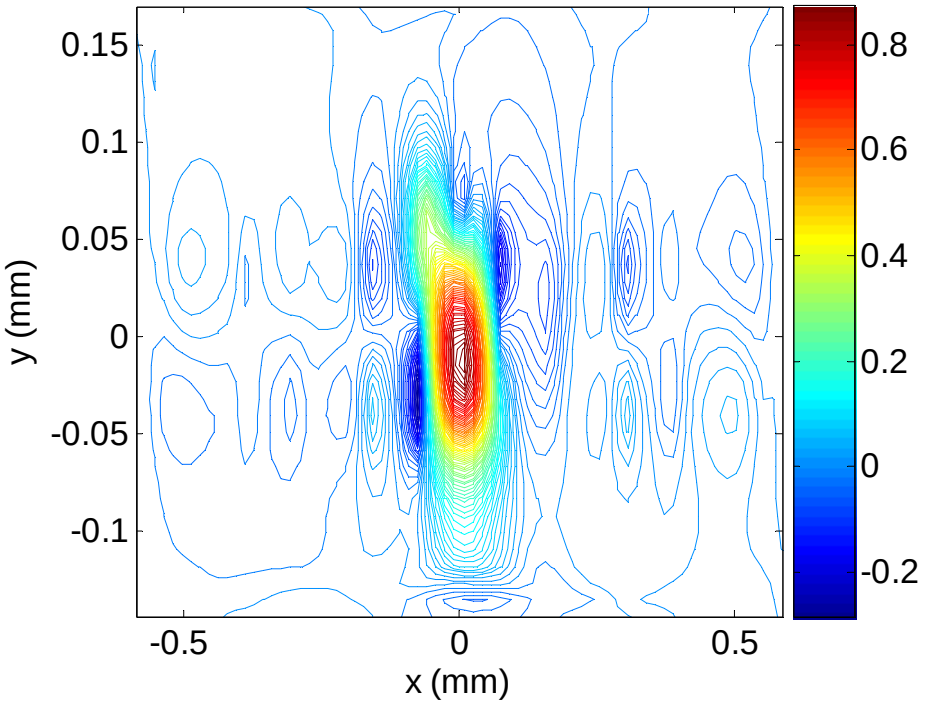

(d)

Figure 4.5 Cross-section of electromagnetic field components obtained by 3D-FDTD analysis of asymmetric loaded PC slab waveguide at f=604.5 GHz (a/λ=0.267) with t=0.8a, w=0.6a, t_{up}=0.2a, n_{si}=3.48 (a) E_x (b) E_y (c) H_x (d) H_y.

Now that the overlap between the x-polarized and y-polarized guiding are defined, the 3D-FDTD simulation for extracting the modal characteristics of an asymmetric loaded PC slab waveguide will be limited to the aforementioned frequency band. In the next subsection, the modal analysis using 3D-FDTD simulation is presented.

4.3.1.2 3D-FDTD modal analysis

To calculate the birefringence and the half-beat length L_π, using 3D-FDTD, it is required to obtain the vector-propagation characteristics of the hybrid modes of the asymmetric loaded PC slab waveguide, (the waveguide structure is illustrated in Figure 4.1(b)).The effective frequency-dependent refraction indices of the structure for both E_x and E_y components are calculated using SFT analysis of the transverse electric field components along the propagation direction at the center point of the defect line (x=0, y=0). For 3D-FDTD simulation, the input is a single frequency sinusoidal with Guassian distribution in space. As time proceeds and the wave propagate along the z-direction inside the defect line, the wave evolves into the modes of the structure. Thus, in the steady state case by applying SFT to the field distribution along the propagation direction at any point inside the defect line, the propagation characteristics of the modes can be obtained.

In our design example, the structural parameters of the PC polarization rotator are determined by assigning the normalized central frequency of 0.265 in the fundamental mode, to the operating frequency. For example, for f=600 GHz to correspond to the normalized frequency of 0.265, the unit cell size would be 132.5 μm (a= 0.265λ).

Figure 4.4 (c) shows that the overlap between the x-polarized and y-polarized guiding laid within the frequency band of 0.258-0.267. The normalized SFT diagram for the normalized input frequency of a/λ=0.265 is calculated and plotted in Figure 4.6. Figure 4.6(a) and 4.6(b) correspond to TE-like and TM-like excitations. For the TE-like excitation, the input E_y is the dominant component, however, as the wave proceeds, the input evolves into the hybrid modes of the structure that are depicted by the two dominant peaks in the SFT spectrum. In the SFT spectrum, the horizontal axis is the $1/\lambda_g$ where $\lambda_g = \frac{\lambda}{n_{eff}}$. λ and n_{eff} are the free space wavelength and effective refractive index of the propagating mode. For example, in Figure 4.6(a) the SFT spectrum of E_y has a peak at

$1/\lambda_g$=5.16 where it coincides with one the peaks of the SFT spectrum of the E_x component. The corresponding effective refractive index n_{eff} or n_f (refractive index of fast hybrid mode) would be 2.58. The other peak of the SFT spectrum for the E_x component corresponds to the x-polarized or slow mode. It has been located at $1/\lambda_g$=5.52 resulting in n_{eff} or n_s (refractive index of slow hybrid mode) of 2.76. It is seen that the asymmetric loaded layer has induced a large birefringence. Having determined the effective refractive indices of the two hybrid modes, the half-beat length or L_π can be calculated using Equation (2.21). For the two refractive indices calculated above at λ=500 μm, the half-beat length (L_π) would be 1.39 mm that is equivalent to 10.5a, where a is the unit cell of the PC slab. The same values are obtained for the n_f and n_s from graph 4.5(b) which is plotted for the TM-like input wave.

Another important parameter that can be extracted from modal analysis is the polarization rotation angle, φ, which is the tilted angle of the optical axes with respect to Cartesian coordinate depicted in Figure 2.15. The following expression is used to calculate the polarization rotation angle:

$$\varphi = \tan^{-1}\left(\frac{abs(SFT(E_x))}{abs(SFT(E_y))}\right)\Bigg|_{@\ peak,TE-like} = \tan^{-1}\left(\frac{abs(SFT(E_y))}{abs(SFT(E_x))}\right)\Bigg|_{@\ peak,TM-like} \quad (4.15)$$

In calculating φ, it is assumed that the linear relationship between x and y components of field transforms to the Fourier spectrum. In Figure 4.6(a), the normalized values of SFT are plotted. The absolute values of SFT(E_x) and SFT(E_y) are 14.5 and 127, respectively. Thus, the value of the polarization rotation angle (φ) for above example is 6.5^o. The polarization rotation angle is important in determining the total number of loaded layers required to achieve 90^o polarization rotation. For this example, at the end of the fourth loaded layer, the polarization of the input wave should be rotated by 104^o which exceeds 90^o. To compensate the extra rotation angle, the length of the last top loaded layer can be increased. Thus, the hybrid mode analysis provides the length and total numbers of top loaded layers.

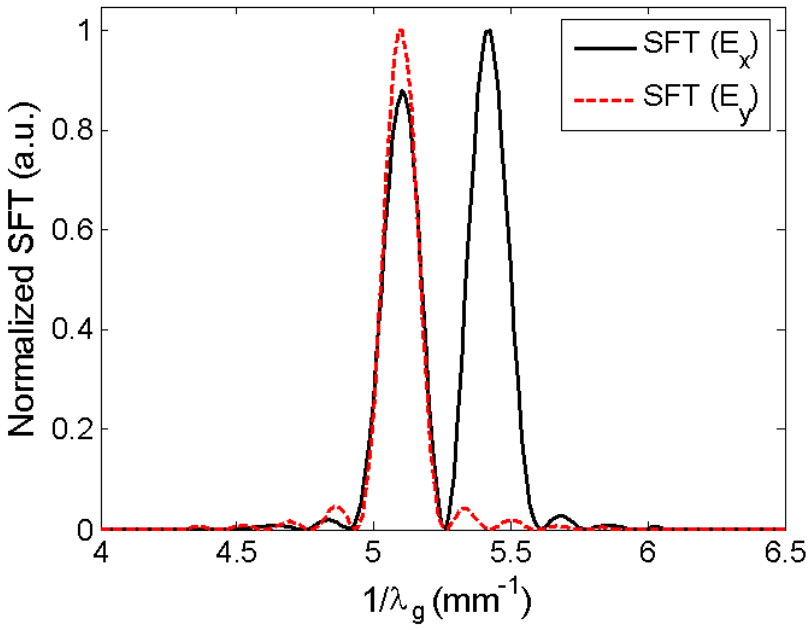

(a)

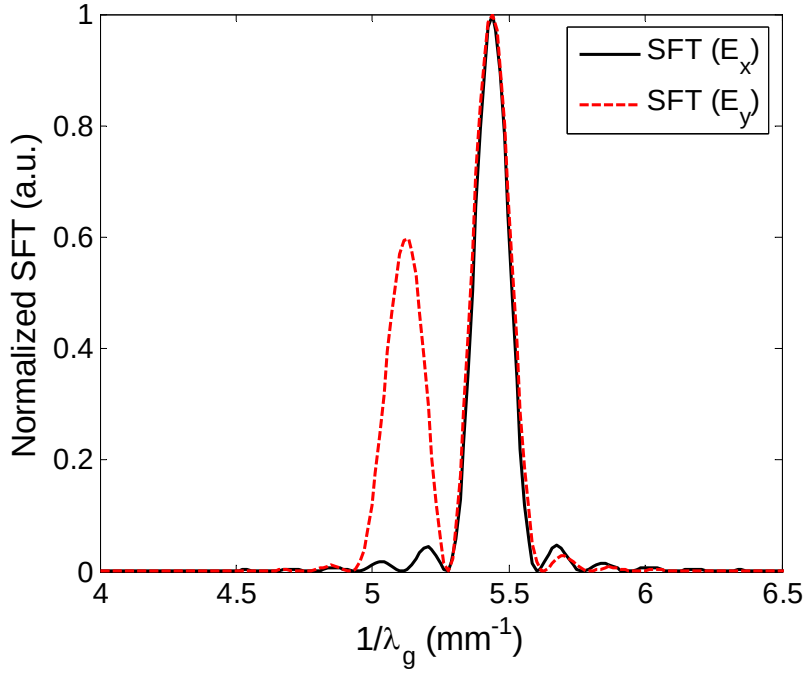

(b)

Figure 4.6 The normalized SFT spectrum of the transverse electric field components of an asymmetric loaded PC slab waveguide for (a) TE-like wave input and (b) TM-like wave input (w=0.6a, t=0.8a and t_{up}=0.2a, λ=500 μm).

Below the normalized frequency of a/λ=0.257, only the y-polarized wave is guided, as such, no polarization rotation is expected as the x-polarized wave is not guided. To verify this, the normalized SFT diagram of an asymmetric loaded PC slab waveguide for the input normalized frequency of a/λ=0.252 is calculated and plotted inFigure 4.7. The input wave is y-polarized or is a TE-like wave. This means the dominant component of the electric field is E_y. The normalized SFT spectrum of both E_y and E_x components of the electric field are plotted in Figure 4.7. The SFT diagram of E_x has only one peak verifying the PWEM diagram that only the y-polarized wave is guided at this frequency.

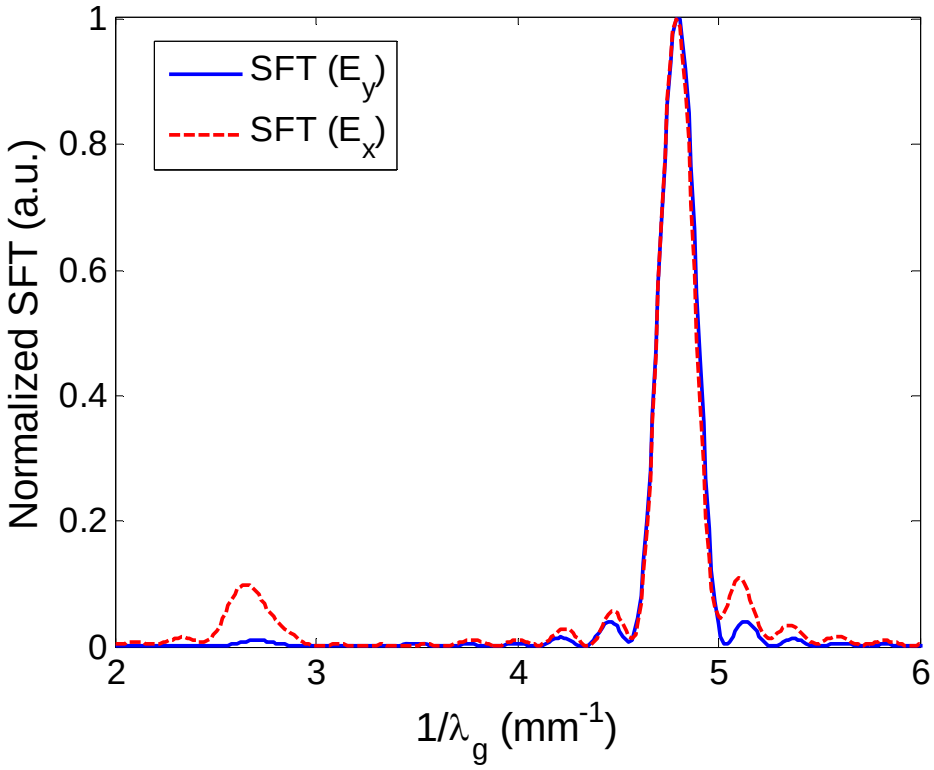

Figure 4.7 The normalized SFT spectrum of transverse electric field components of asymmetric loaded PC slab waveguide for TE-like wave input (w=0.6a, t=0.8a and t_{up}=0.2a, a/λ_0=0.252).

The half-beat coupling length and polarization rotation angle (L_π, φ) for three different thicknesses (t_{up}=0.1a, 0.15a and 0.2a) of top layer are calculated and plotted versus the normalized frequency in Figures 4.8 (a) and (b), respectively. As it is shown in

Figure 4.8(a), by reducing the thickness of the top loaded layer of the square hole, L_π decreases, but, to compare the total distance required for a 90^o rotation both L_π and φ must be taken into account. As a matter of fact, the phase shift per length determines the total length of the device. This concept has been explained later in this chapter. The variation of L_π and φ versus frequency are smooth, hence, it is expected that a 90^o polarization rotation can be achieved over a wide frequency band for a square air hole for all three thicknesses.

In next section, the design of the polarization rotator using coupled-mode theory based on semi-vectorial modes is presented.

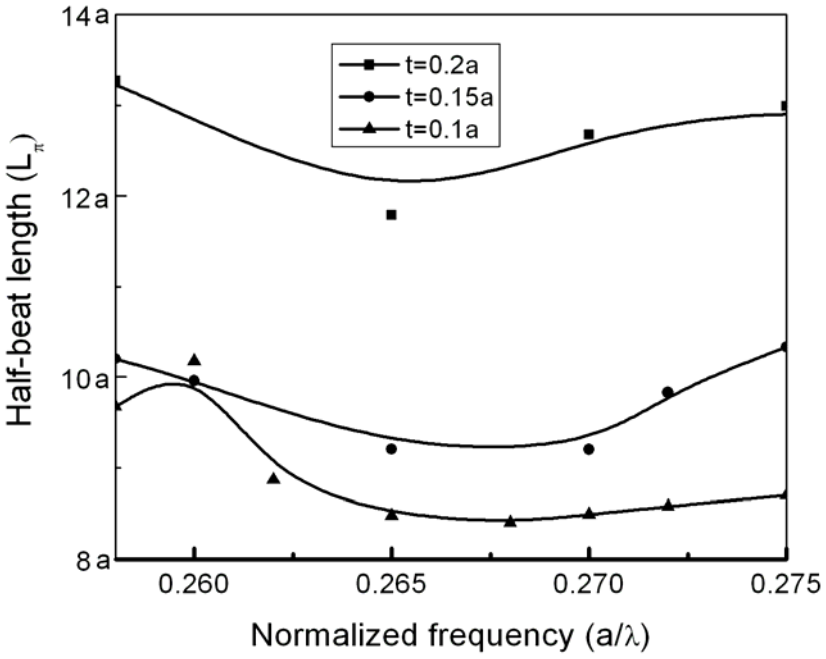

(a)

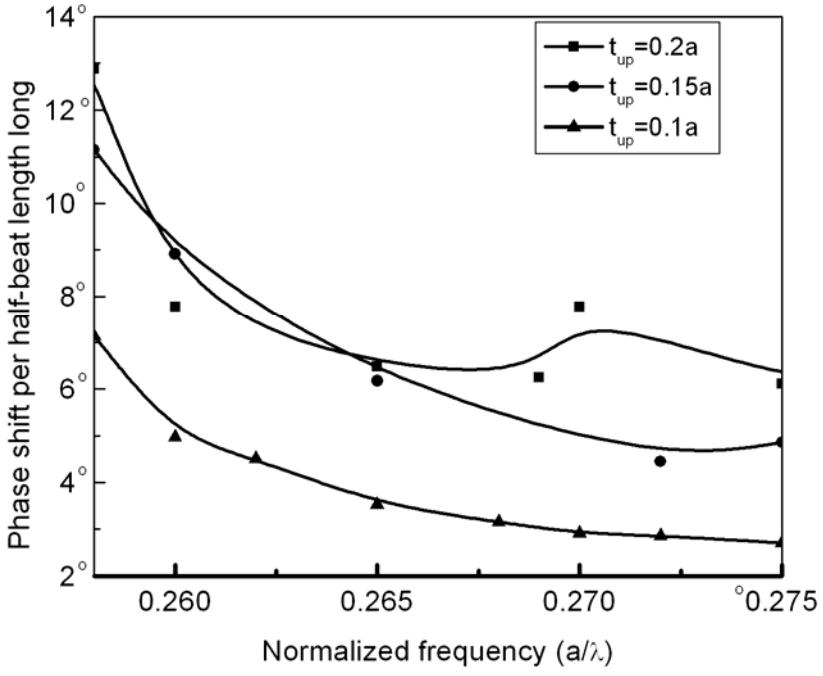

(b)

Figure 4.8 (a) The half-beat length (b) phase shift per half-beat length long versus the normalized frequency for different top layer thicknesses for square shaped air holes and t_{up}=0.2a, 0.15a and 0.1a (w=0.6a, t=0.8a and n_{si}=3.48).

4.3.1.3 Design of the polarization rotator using coupled-mode theory

In this section, we use the coupled mode theory discussed earlier to design the asymmetrically loaded PC polarization rotator. In order to employ the coupled mode theory, first, the semi-vectorial modes of the asymmetrically loaded PC slab waveguide, shown in Figure 4.1(b), must be calculated. Semi-vectorial BPM was employed for the semi-vectorial modal analysis of the structure. The normalized electric field for x-polarized (TM-like) and y-polarized (TE-like) waves for the normalized frequency of $a/\lambda=0.265$ are shown in Figures 4.9(a) and 4.9(b). It shows that the electric field distribution is asymmetric in both vertical and lateral directions as a result of the geometrical asymmetry. The propagation constants of the corresponding modes were calculated also using semi-vectorial BPM simulation, as well. The effective refractive indices of x-polarized and y-polarized waves were 2.6567 and 2.5007, respectively. A big birefringence was observed, as expected in the PC slab waveguide structure. For aforementioned parameters, the coupling coefficients of the periodic asymmetric loaded PC polarization rotator (shown in Figure 4.1(b)) were calculated using Equation (4.9) for both regions of 1 and 2, as depicted in Figure 4.3. Using Equation (4.11), the loading period was calculated to be approximately, 10.8a. The value of the half-beat length, L_π, was computed using the coupled-mode theory and hybrid mode analysis was 10.8a and 10.5a, respectively. Both methods delivered the same results prove their effectiveness. Figure 4.10 shows the power exchange between the two polarizations along the propagation distance for $a/\lambda=0.275$, 0.265 and 0.255, $\lambda_0=500$ μm (600GHz). The length of each top loaded layer is 10a.

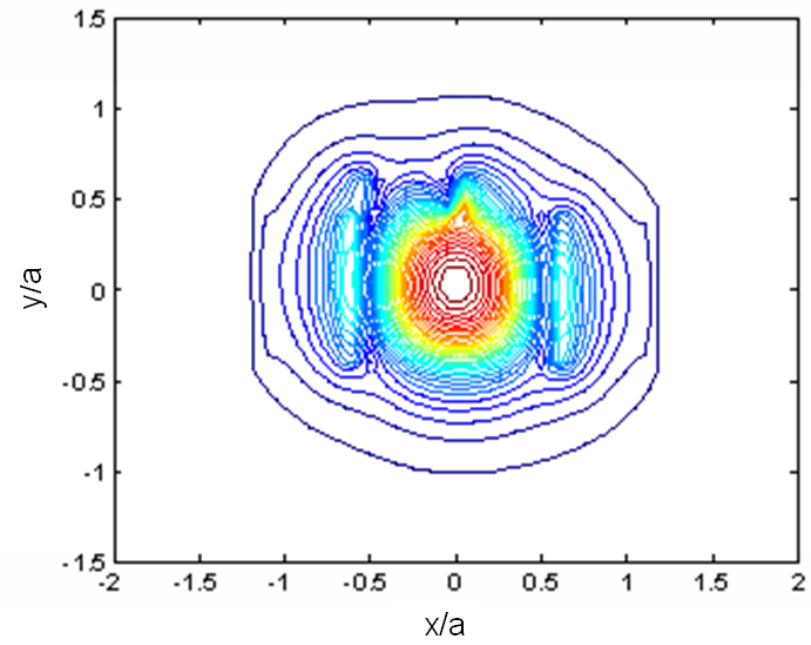

(a)

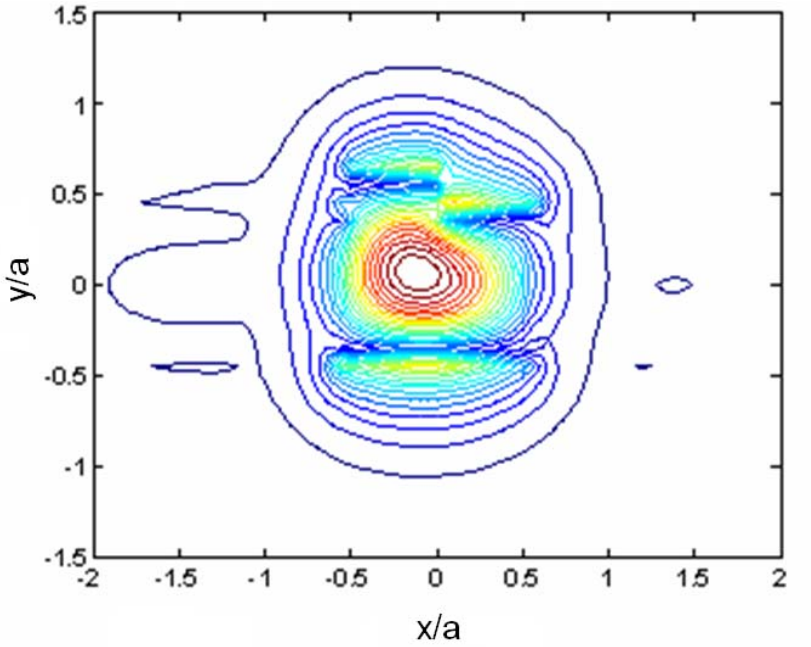

(b)

Figure 4.9 The profile of (a) E_x and (b)E_y components of x-polarized and y-polarized modes of the structure shown in Figure 4.1(b) obtained by semi-vectorial 3D BPM analysis (t=0.8a, t_{up}=0.2a, w=0.6a, a=132.5 μm, n_{si}=3.48 and λ=500 μm).

Given the Power Conversion Efficiency (P.C.E.) is defined as follows:

$$P.C.E. = \frac{P_{TM}}{P_{TM} + P_{TE}} \times 100 = \frac{a_x^2}{a_x^2 + a_y^2} \times 100 \qquad (4.16)$$

For a/λ=0.265 (λ=0.5 mm), 96% efficiency at z=7.2 mm (millimeter) was achieved. It is expected that by increasing or decreasing the normalized frequency, the power conversion efficiency reduces. To achieve high power conversion efficiency, the last silicon brick (top loaded layer) was not flipped around the z-axis. In other words, the length of the last silicon brick was larger than 10a as it was predicted by the hybrid mode analysis method. The P.C.E. for a/λ=0.275 and 0.255 is larger than 75% at z=7.2 mm. Thus, it is expected to have a very high P.C.E. within the frequency band of the defect mode (0.258-0.267).

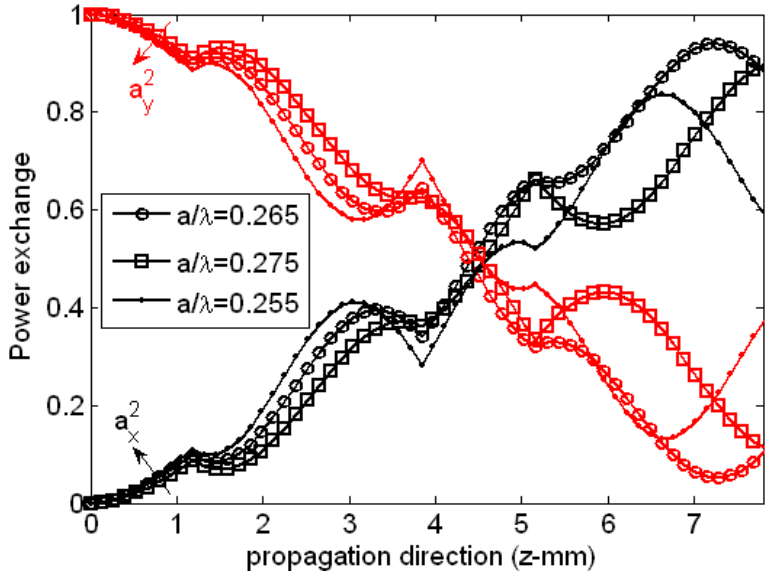

Figure 4.10 Power exchange between the x-polarized and y-polarized wave versus the propagation length (t=0.8a, t_{up}=0.2a, w=0.6a, a=132.5 μm, n_{si}=3.48) for a/λ=0.255, 0.265 and 0.275 obtained by coupled-mode analysis.

4.4 3D-FDTD simulation of polarization rotator structure

Both design methodologies suggest that a high power exchange rate is expected to be observedin the overlap frequency band between the fast and slow mode guiding, 0.258-0.267. To verify the aforementioned results, 3D-FDTD was employed to simulate the polarization rotator. The simulated structure (Figure 4.1(a)) consists of 70 rows of holes along the propagation direction and 11 rows of holes (including the defect row) in the x-direction. The mesh sizes along the x, y and z-directions (Δx, Δy and Δz) are $\Delta x=\Delta z=0.0331\lambda$ and $\Delta y=0.0172\lambda$. The Perfectly Matched Layer (PML) boundary condition was applied for all three directions. Time waveforms in the 3D_FDTD model were chosen as a single frequency sinusoid. The spatial distribution of the incident field was Guassian.

The frequency of the input signal lies within the normalized frequency band of the defect mode which is 0.258-0.267 corresponding to 586 - 601 GHz. As the wave proceeds, the polarization of the input signal starts rotating. The power exchange between the (E_x, E_y) and (H_x, H_y) components was observed. To achieve the maximum power conversion, the size of the last top silicon brick was 15a instead of 10a. Figure 4.11 shows the contour plot of the transverse field components, E_x, E_y, H_x and H_y at the input for $a/\lambda=0.265$. The input excitation is TE-like, and E_y and H_x are the dominant components that have even parity as opposed to the non-dominant components E_x and H_y that have odd symmetry with respect to y=0 plane.

The contour plot of E_x and H_y at a point close to the output are plotted in Figure 4.12. It is seen that the parity of the E_x and H_y components have changed and become the dominant component. The amplitudes of E_y and H_x have decreased more than an order of magnitude and reached to zero at the output plane. Thus, a 90^o rotation of polarization is realized at the output.

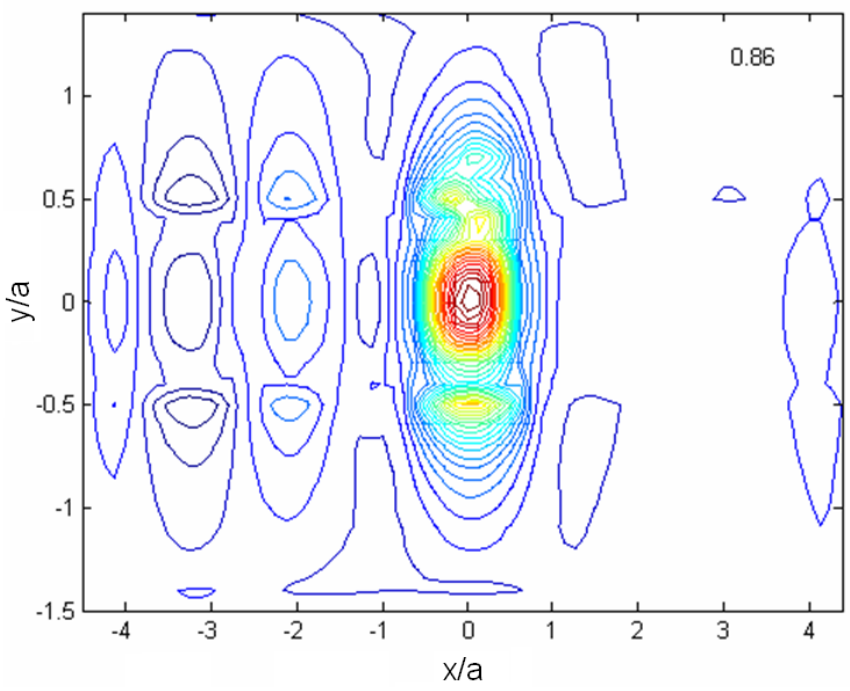
0.86
y/a
x/a
1
0.5
0
-0.5
-1
-1.5
-4
-3
-2
-1
0
1
2
3
4

(a)

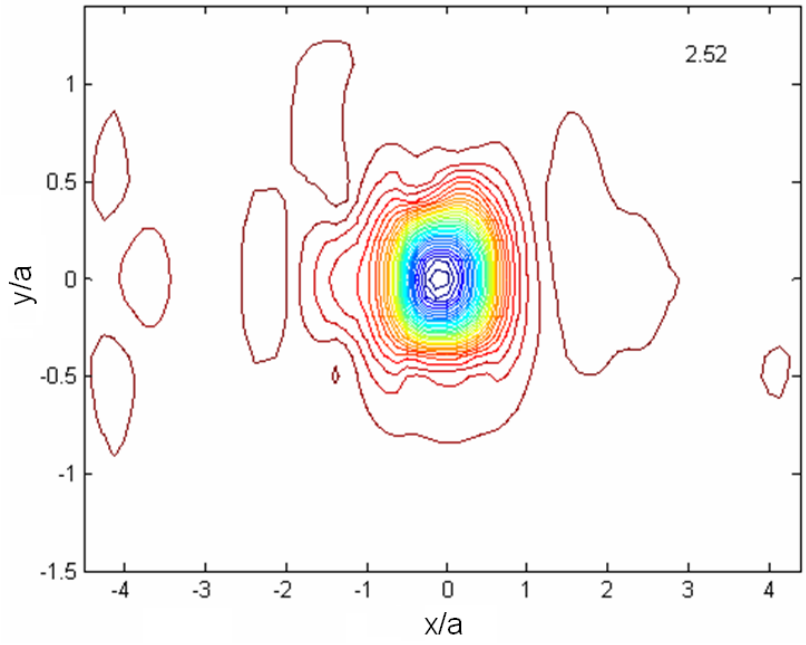
2.52
y/a
x/a
1
0.5
0
-0.5
-1
-1.5
-4
-3
-2
-1
0
1
2
3
4

(b)

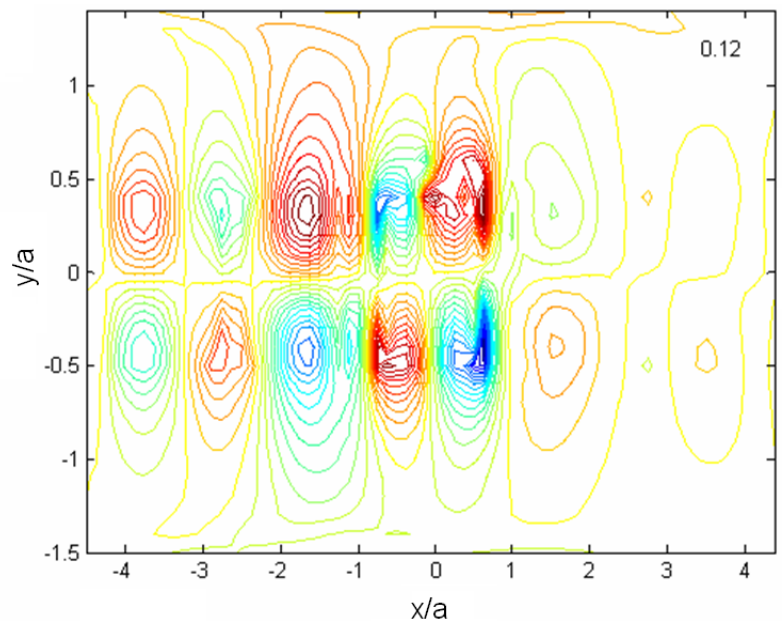

(c)

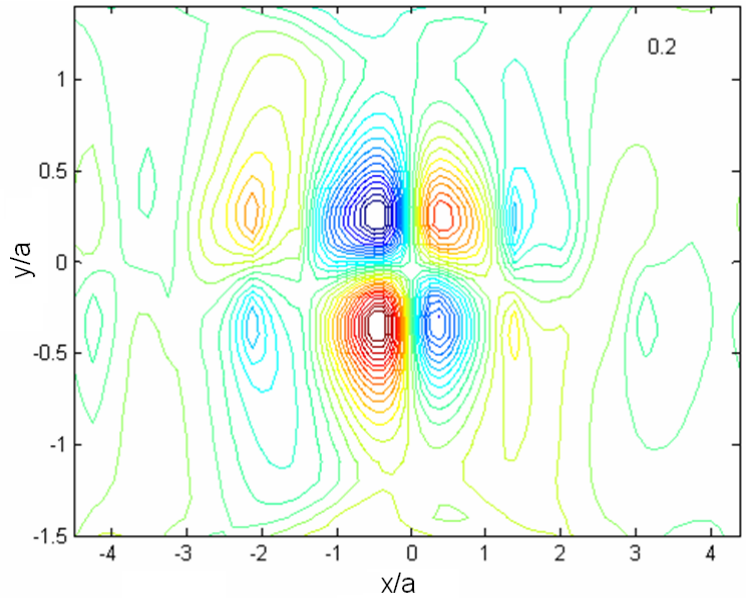

(d)

Figure 4.11 The contour plot of the cross section of the (a) E_y, (b) H_x, (c) E_x and (d) H_y components at the input plane (t=0.8a, t_{up}=0.2a, n_{si}=3.48, a/λ=0.265, λ=500 μm).

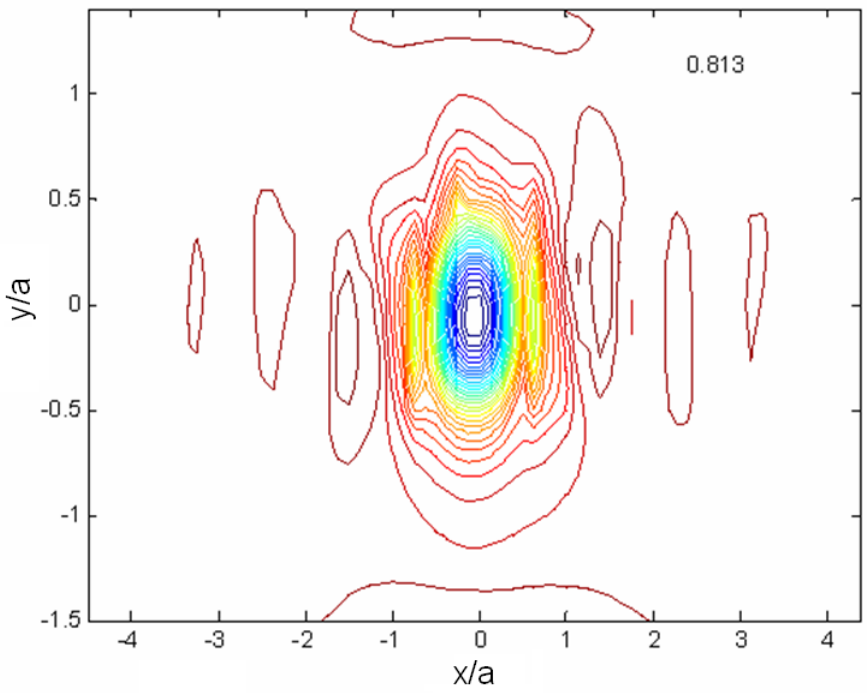

(a)

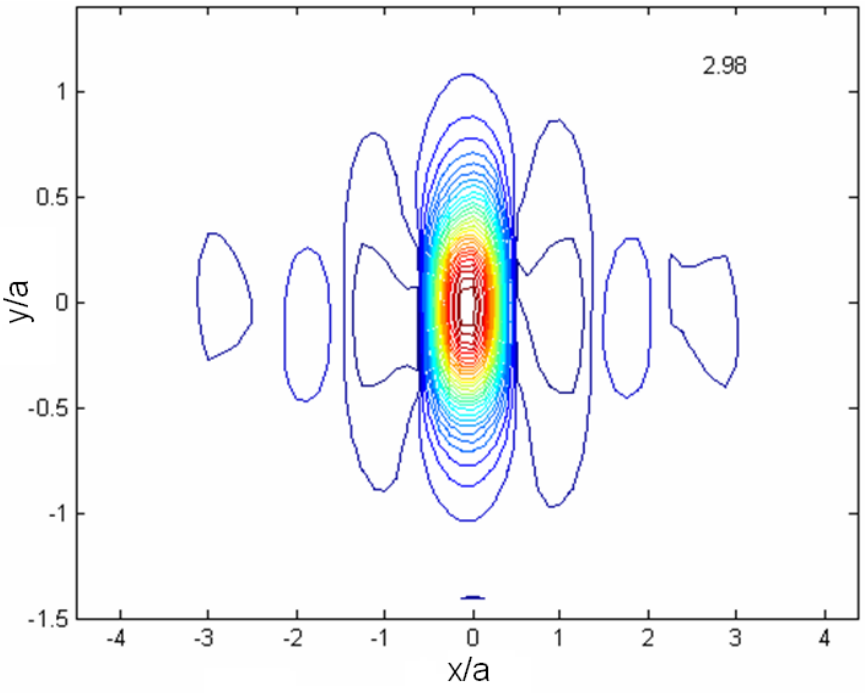

(b)

Figure 4.12 Contour plot of the cross section of (a) E_x and (b) H_y at z=5.5 mm (t=0.8a, t_{up}=0.2a, n_{si}=3.48, a/λ=0.265, λ=500 μm).

To show the power exchange between the two polarizations, the z-varying square amplitudes of the E_x and E_y components were graphed. Figure 4.13 shows $a_x^2(z)$ and $a_y^2(z)$ along the propagation direction for the normalized frequency of 0.265 corresponding to the free space wavelength of 500 μm. The two main elements contributing to the numerical noise are local reflections and imperfections of the absorbing layer. Dots in the figure are the actual values of the 3D-FDTD analysis. To have a smooth picture of the $a_x^2(z)$ and $a_y^2(z)$ variations along the propagation direction, a polynomial fit to the data using a least square method is also shown in the figure. Each plot consists of more than 100 data points. The FDTD "turn-on" transition of the input wave has also been included in the graph (first 0.5 mm). This portion is obviously a numerical artifact of the FDTD scheme. In Figure 4.13 it is shown that after almost 6 mm (12λ) complete power exchange took place. Comparing this graph with a coupled-mode (counterpart plot in Figure 4.10), it is seen that the power exchange between the two polarizations takes place at a smaller propagation distance of 6 mm in comparison with 7.2 mm. Moreover, the value of P.C.E obtained by 3D-FDTD is close to 100 %; whereas, P.C.E for the same wavelength for coupled-mode analysis is 96%. On the other hand, the hybrid mode analysis method predicted that 100% polarization conversion could take place at less than $4.5L_\pi$, 6 mm. Therefore, the hybrid mode analysis design methodology provides more accurate results.

The 3D-FDTD simulations were repeated for other frequencies to obtain the frequency dependence of polarization conversion. The power exchange rate for both coupled-mode analysis and 3D-FDTD are graphed versus the normalized frequency in Figure 4.14. Coupled-mode analysis shows that a P.C.E of higher than 90% was achieved within the normalized frequency band of 0.258-0.267. The 3D-FDTD simulation results show that a P.C.E close to 100% was realized within the frequency band of 0.258-0.267, over which the defect mode lies.

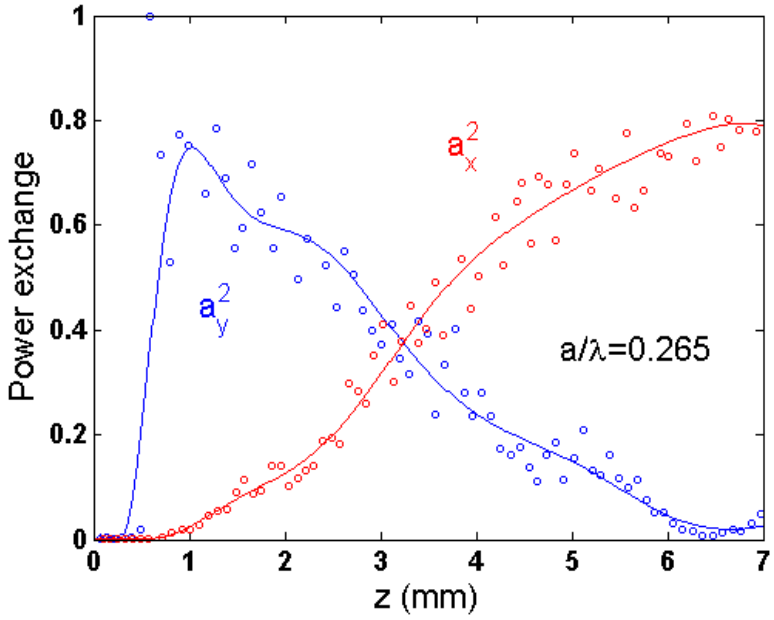

Figure 4.13 Power exchange between the x-polarized and y-polarized wave versus the propagation length for a/λ=0.265 obtained by 3D-FDTD simulation (t=0.8a, t_{up}=0.2a, w=0.6a, a=132.5 μm, n_{si}=3.48, λ=500 μm).

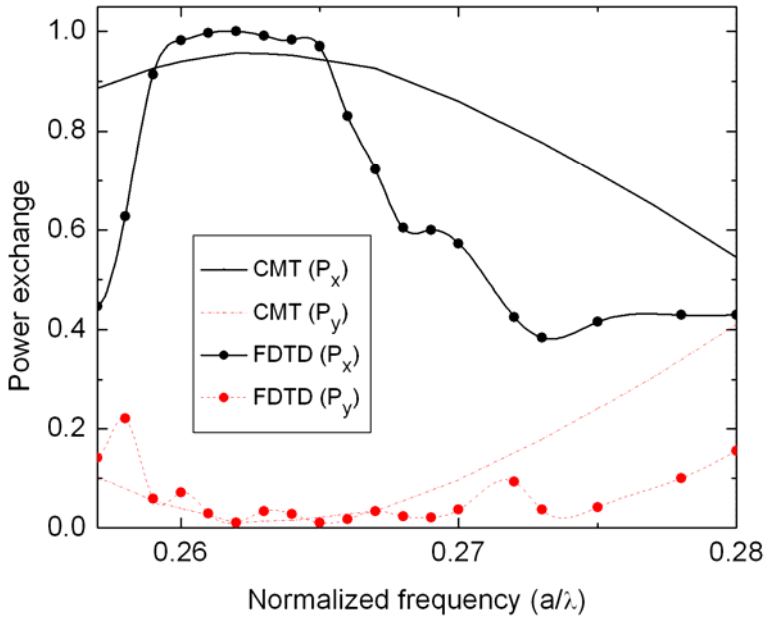

Figure 4.14 Power exchange between the x-polarized and y-polarized waves versus frequency for both coupled-mode analysis and 3D-FDTD simulations ((t=0.8a, t_{up}=0.2a, w=0.6a, a=132.5 μm, n_{si}=3.48).

At normalized frequencies higher than 0.267, *Ey* starts leaking energy to the TE-like PC slab modes as it crosses the TE-like PC slab modes, as illustrated in Figure 4.4(c). The Figure 4.15 graph shows the FDTD simulation of the power exchange between the x-polarized and y-polarized waves for a/λ=0.275. It is seen that for a/λ=0.275, the drop slope of $a_y^2(z)$ is much sharper than the rise slope of $a_x^2(z)$. More importantly, $a_y^2(z)$ is dropping much faster than that of a/λ=0.265, Figure 4.13. This observation can be interpreted as if E_y is dissipating and leaking energy into the TE-like slab modes. As a result, a sudden drop on power exchange rate is observed at normalized frequencies higher than 0.267. The semi-vectorial BPM analysis utilized for modal analysis is not capable of including the PC modes. Therefore, in the power exchange graph calculated by coupled-mode analysis for a normalized frequency of a/λ=0.275 (Figure 4.10), no power dissipation is observed as opposed to the 3D-FDTD simulation (Figure 4.15).

At frequencies lower than a/λ<0.255, only the y-polarized wave is guided, and so no power exchange between the two polarization takes place. Our recommendation is to avoid this region for the design of the polarization rotator. Having compared FDTD and coupled-mode analyses, the coupled-mode theory approach is effective within the frequency band where the x-polarized and y-polarized guiding overlap. The other approach described in 4.3.1.2 can predict the frequency response of the PC based polarization rotator. In the polarization rotation angle graph versus frequency obtained using hybrid mode analysis, a sudden jump in the polarization rotation angle at normalized frequencies larger than 0.268 and smaller than 0.257 is observed that is a sign of changing behavior of the modes.

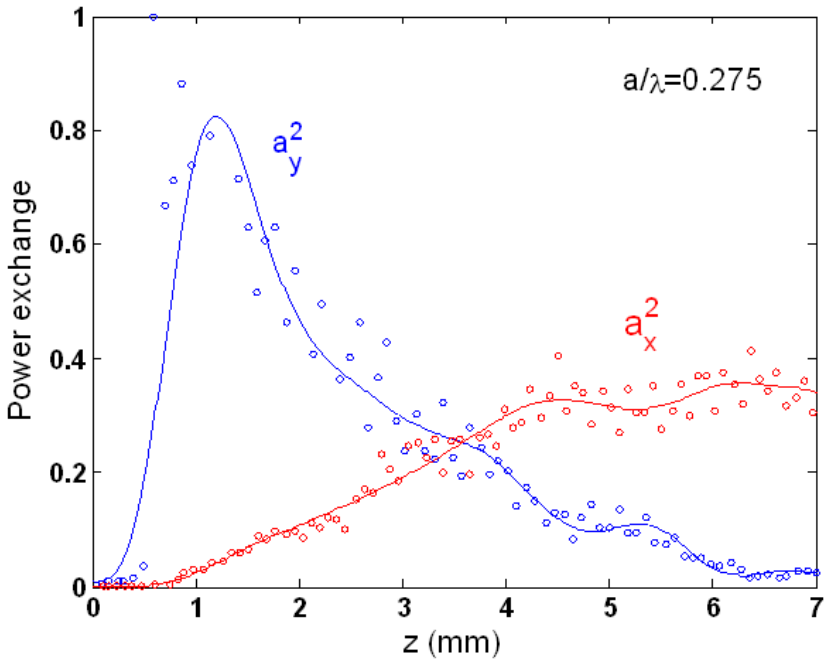

Figure 4.15 Power exchange between the x-polarized and y-polarized wave versus the propagation length for a/λ=0.275 obtained by 3D-FDTD simulation (t=0.8a, t_{up}=0.2a, w=0.6a, a=132.5 μm, n_{si}=3.48, λ=500 μm).

4.5 Optimization of the thickness of top loaded layer

Another design parameter is the thickness of the top loaded layer. It is expected that by reducing the thickness of the top loaded layer, the field will be concentrated mostly at the edges leading to a larger birefringent and smaller half-beat length, L_π. This importance is assessed in this section using 3D-FDTD analysis.

Three different thicknesses of top loaded layers including t_{up}=0.2a, 0.15a and 0.1a are studied. PWEM analysis shows that the band diagram of an asymmetric loaded PC slab waveguide barely changes when the thickness of the top loaded layer is changed. So, the study has been concentrated in the normalized frequency band of 0.255-0.275 where it covers both the x-polarized and y-polarized modes. Figure 4.8 graphs the half-beat length and polarization rotation angle versus frequency for all three top loaded layer thicknesses. It shows that the half-beat length decreases by decreasing the thickness of top loaded layer ,but both L_π and φ must be taken into account to define the total length of the device. The importance of both L_π and φ in determining the total length of the polarization converter are comprehended by following examples.,At a normalized frequency (a/λ) of 0.265, the half-beat length for t_{up}=0.2a, t_{up}=0.15a and t_{up}=0.1a are 10.5a, 9.2a and 8.5a. On the other hand, φ for t_{up}=0.2a, 0.15a and 0.1a are 6.5^o, 6.173^o and 3.53^o. For t_{up}=0.2a and 0.15a, the difference between the polarization rotation angle is small. The 3D-FDTD simulation was run for periodic asymmetric loaded PC slab waveguide with (t_{up}=0.2a, L_π=10a) and (t_{up}=0.15a, L_π =9a).

To show the power exchange between the two polarizations, the z-varying square amplitudes of the E_y components ($a_y^2(z)$) for both t_{up}=0.2a and t_{up} =0.15a for the TE-like wave as an input were graphed in Figure 4.16(a) for the normalized frequency of 0.265 corresponding to the free space wavelength of 500 μm. To have a better picture of how $a_y^2(z)$ vary along the propagation direction, the data was extrapolated with a polynomial using Least Square method. It is seen that after 6.5 mm (13λ) for t_{up}=0.2a and 6.8 mm (13.6λ) for t_{up}=0.15a, $a_y^2(z)$ has almost reached zero and the complete power exchange between x and y polarizations has taken place. Therefore, there is not a significant difference on the propagation distance of t_{up}=0.15a and t_{up}=0.2a, since, the difference between the value of φ is very small for these two thicknesses. The same graphs for

t_{up}=0.2a and t_{up}=0.1a are plotted in Figure 4.16(b). The length of the top bricks are 10a and 8a for t_{up}=0.2a and t_{up}=0.1a. The value of φ (polarization rotation angle) for t_{up} =0.2a and t_{up}=0.1a are 6.5^o and 3.53^o, thus, a significant difference on the total length for complete power exchange for these two thicknesses is expected. Figure 4.16(b) shows that $a_y^2(z)$ reaches zero at 6.4 mm and 9 mm for t_{up}=0.2a and t_{up}=0.1a. By decreasing the thickness of the top layer from t_{up}=0.2a to t_{up}=0.1a, the total propagation distance required to achieve 90^o polarization rotation has increased by 40%. The phase-shift per unit length for t_{up}=0.2a (6.5^0/10a) is almost 35% more than that of t_{up}=0.1a this proves the discussion made in the previous section that the determinant parameter for the total optical length of the device is the phase-shift per unit length rather than L_π by itself.

The 3D-FDTD simulations were repeated for other frequencies to obtain the frequency dependence of polarization conversion. The power exchange rate for all three top layer thicknesses (t_{up}=0.2a, 0.15a and 0.1a) versus the normalized frequency are graphed in Figure 4.17. The propagation length for t_{up}=0.2a, 0.15a and 0.1a are considered to be 6.4 mm, 7 mm and 9 mm, respectively. The 3D-FDTD simulation results shows that a P.C.E higher than 90% for t_{up}=0.2a, and is realized within the frequency band of 0.258-0.267, over which both x-polarized and y-polarized modes lie.

For t=0.15a and t=0.1a, a P.C.E higher than 90% is achieved within the normalized frequency band of 0.26-0.266 and 0.261-0.265. At a normalized frequency of a/λ=0.26 and o.259, t_{up}=0.2a provides a 22% and 26% improvement in the P.C.E in comparison with t=0.1a, respectively. These graphs suggest that by increasing the thickness of the top loaded layer, the frequency response of the polarization converter structure improves significantly. This improvement in bandwidth by increasing the thickness of the top layer could also be explained employing Figure 4.8(b). The variation of φ versus frequency within the normalized frequency of a/λ=0.258-0.268 for t_{up}=0.2a is smoother than that of the other two thicknesses (t_{up}=0.15a and 0.1a). Hence, a wider frequency band operation for the polarization converter structure with t_{up}=0.2a is expected.

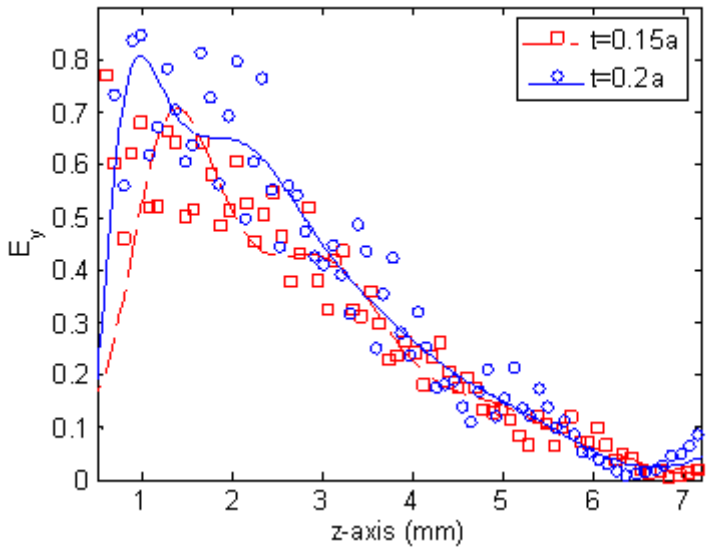

(a)

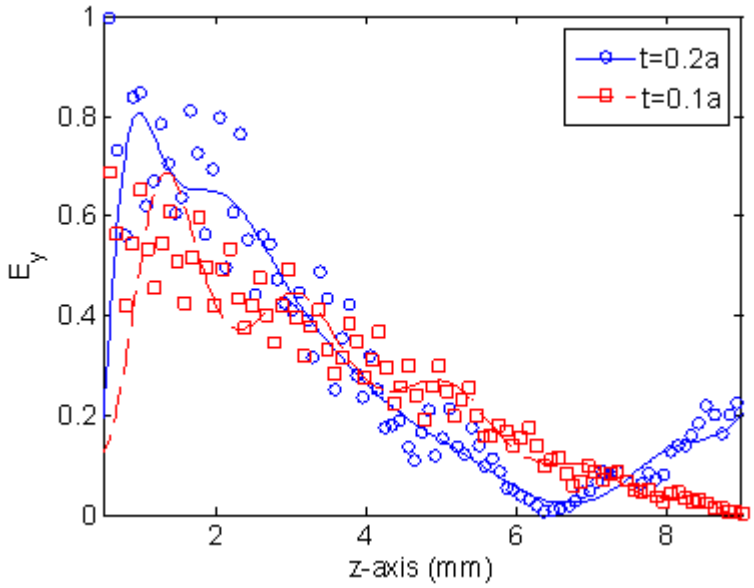

(b)

Figure 4.16 $a_y^2(z)$ versus propagation distance of a periodic asymmetric loaded PC slab waveguide for (a) t_{up}=0.2a, 0.15a and (b) t_{up}=0.2a and 0.1a (t=0.8a, w=0.6a and λ=500 μm).

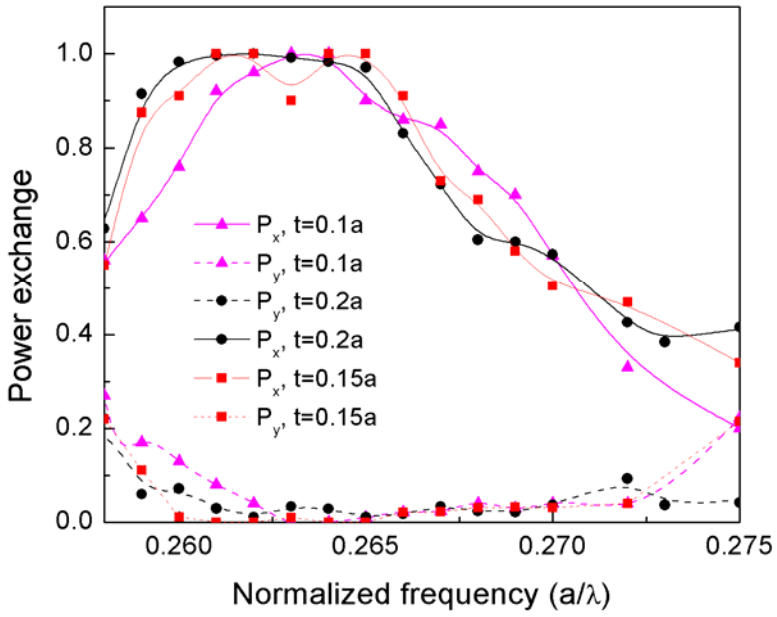

Figure 4.17 Power exchange versus normalized frequency for three different top layers (t_{up}=0.2a, 0.15a and 0.1a, w=0.6a and t=0.8a).

4.6 3D-FDTD circular shape air holes PC based polarization converter

So far, the square-shaped air hole PC based polarization converter has been studied. Here, the study has been extended to the circle-shaped air hole PC based polarization converter. In the process of changing the shape of the air holes, it is important to keep the filling factor of dielectric material per unit cell constant to preserve the band structure characteristics. As it was shown in chapter 3, the radius of the equivalent circular hole to the square hole PC slab is the square width of w=0.6a is $r = 0.47(1+\sqrt{2})w$ (t=0.8a, n_{si}=3.48). For both square hole and circular hole PC slabs for the TM-like wave, the normalized frequencies associated with lower and upper edges of the bandgap are 0.238 and 0.327. No bandgap exists for the TE-like wave for either square shape or circular shape air hole PC slab structure.

The next step is to build a polarization converter structure by periodic loading of the asymmetric top layers. To obtain the birefringence and half-beat length, 3D-FDTD simulation was carried out for an asymmetric loaded circular hole PC slab waveguide with t=0.8a, $r = 0.47(1+\sqrt{2})w$, t_{up}=0.2a, n_{si}=3.48 and a/λ=0.265. By applying a SFT analysis on the electric field distribution (E_x, E_y) along the propagation direction at (x=0, y=0), the effective refractive indices for the slow and fast hybrid modes and L_π are obtained. A normalized SFT diagram for the TE-like and TM-like waves as an input are graphed in Figures 4.18 (a) and (b), respectively. In Figure 4.18(a), the dominant component of the input is E_y as depicted by a solid line. Two peaks in the SFT diagram of E_x correspond to the fast and slow modes. The values of n_s, n_f, L_π and φ are 2.7025, 2.5825, 15.72a (a=132.5 μm) and 22.2°, respectively. The same results are obtained from Figure 4.18 (b). It is expected to observe complete power conversion within $2L_\pi$ where the input polarization rotates by $88.8^o \approx 90^o$. The 3D-FDTD simulation of the circular hole PC based polarization rotator verified this speculation. Power exchange between x and y polarizations in the circular hole PC based polarization converter is graphed in Figure 4.19. It shows almost 90% of the power exchange takes place at a propagation distance of 4 mm (=$2L_\pi$). Some of the power has been lost, the origin of the propagation loss will be discussed later. The total length of the square hole PC polarization rotator is 6.4 mm.

Therefore, by employing a circular hole PC instead of a square hole PC the total length of the polarization rotator has been reduced by approximately 40%.

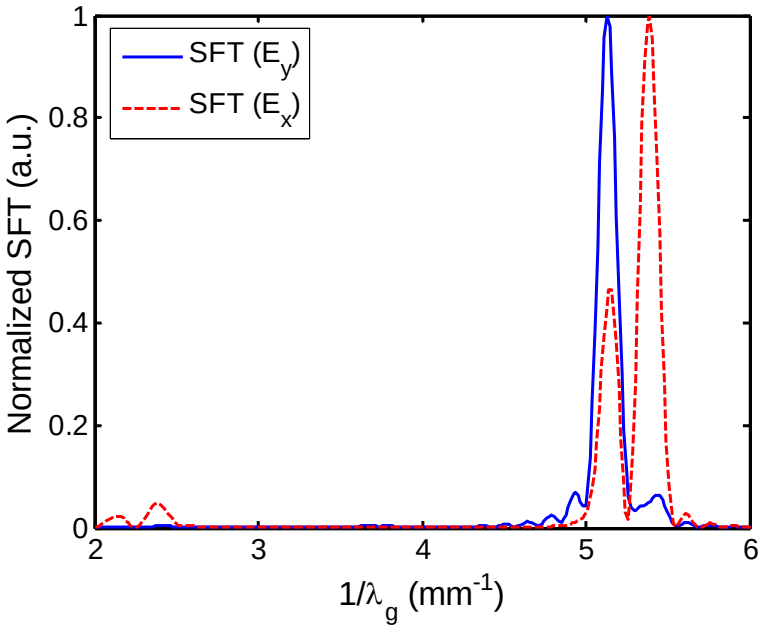

(a)

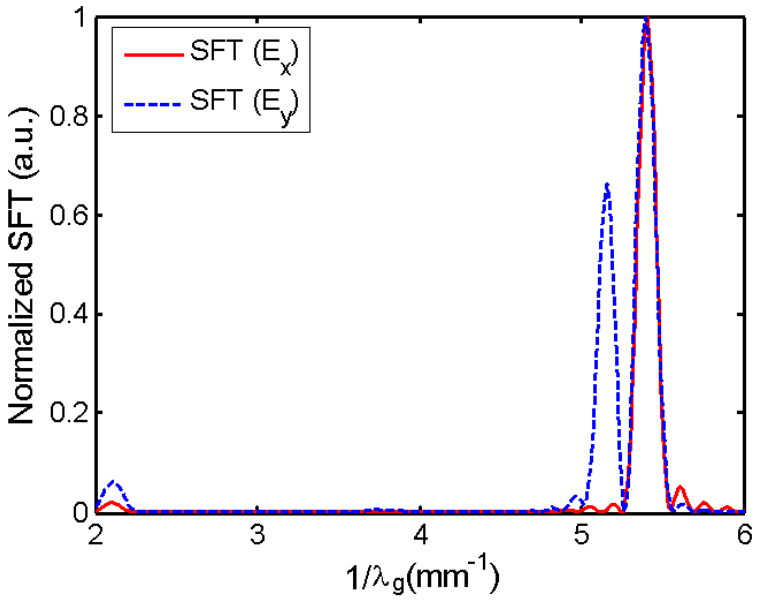

(b)

Figure 4.18 The normalized SFT spectrum of transverse electric field components of an asymmetric loaded circle hole PC slab waveguide for (a) TE-like wave input and (b) TM-like wave input

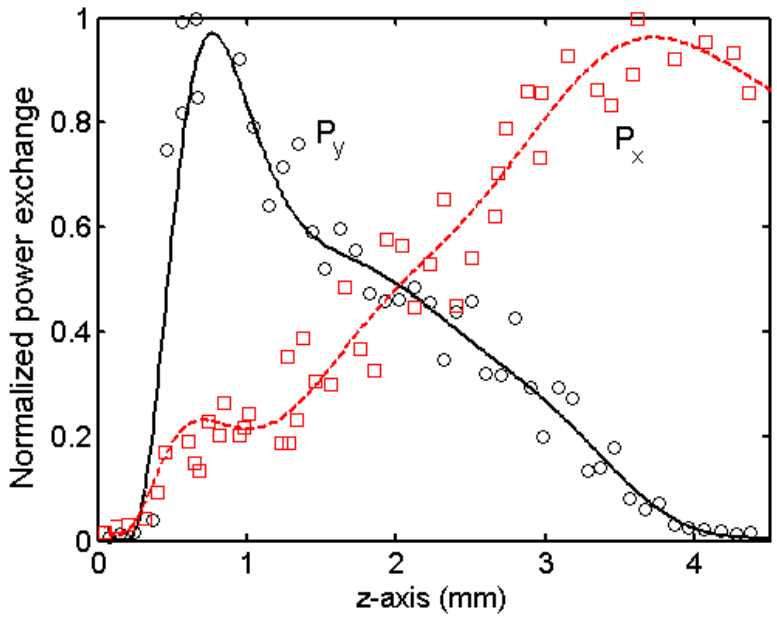

Figure 4.19 Power exchange between the x-polarized and y-polarized wave versus the propagation length for a/λ=0.265 obtained by 3D-FDTD simulation (t=0.8a, t_{up}=0.2a, $r = 0.47(1+\sqrt{2})w$, a=132.5 μm, n_{si}=3.48, λ=500 μm).

To investigate the frequency response of the circular hole PC slab waveguide based polarization rotator, the modal analysis was carried out for other frequencies within frequency band of both fast and slow modes. For example, a normalized SFT diagram at a/λ=0.263 for both TE-like and TM-like input waves are plotted in Figure 4.20 (a) and (b), respectively. Again the SFT of the dominant component of the TE-like input wave, E_y, is depicted by a solid line in Figure 4.20(a). The SFT diagram of the E_x component has one peak at 1/ λ=5.07 corresponding to fast mode with n_f=2.554 and two other peaks at 1/ λ=5.29 and 5.46 with n_{s1}=2.665 and n_{s2}=2.751. The half-beat length between the fast mode and first slow mode (n_{s1}), and fast mode and second slow mode (n_{s2}) would be 17.15a and 9.68a. This means the three modes are involved in the process of power exchange that could have a detrimental effect on the performance of the polarization rotator. In Figure 4.20(b), where the SFT diagram for the TM-like wave is plotted, the dominant component E_x is plotted by a dotted line. It is seen that it is not a pure mode. The background noise in the SFT diagram of E_x component can be attributed to the PC TM-like slab modes.

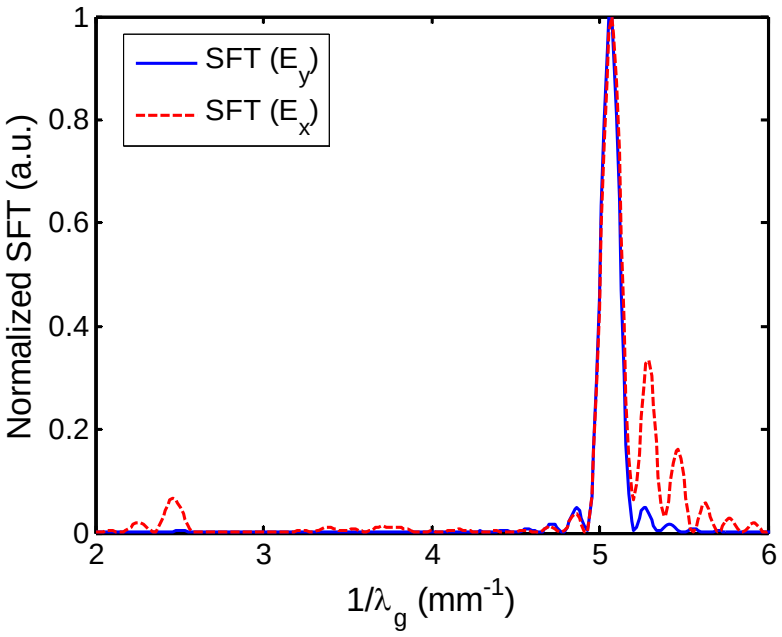

(a)

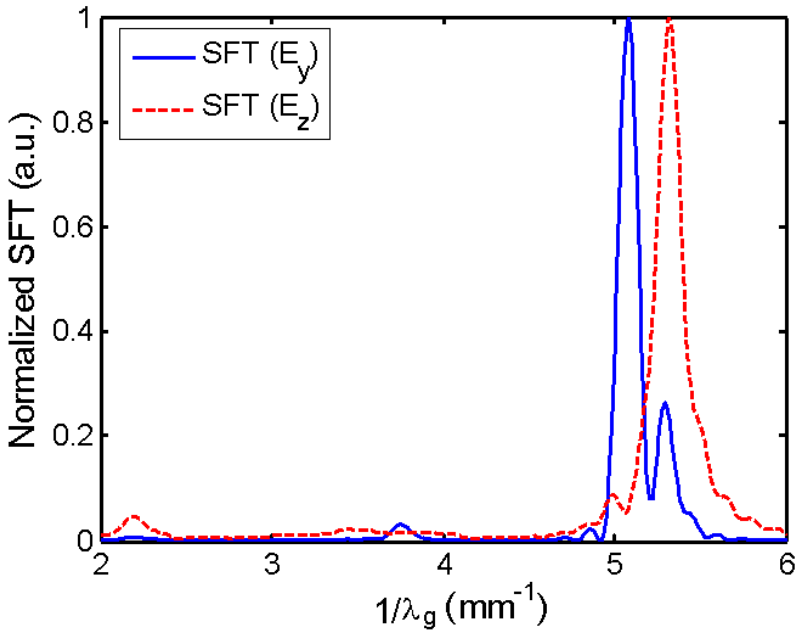

(b)

Figure 4.20 The normalized SFT spectrum of transverse electric field components of asymmetric loaded circle hole PC slab waveguide for (a) TE-like wave input and (b) TM-like wave input ($r = 0.47(1+\sqrt{2})w$, t=0.8a and t_{up}=0.2a, a/λ=0.263, a=132.5 μm).

In Sec. 3.6 of chapter 3, the square hole and circular hole PC slab with w=0.6a and r=0.47(1+√2)w were studied and compared. It was shown that in a finite PC structure, the TM-like PC slab modes would leak into the bandgap. The presence of PC slab modes were more pronounced in the circular hole PC slab. For example, Figure 3.21 (b) shows that PC slab modes are introduced into the lower edge of the bandgap for both square hole and circular hole PC slabs. The leaky TM-like PC slab modes of the circular hole PC structure have two peaks around normalized frequency of a/λ=0.25 and 0.26; thus, they have overlap with the fast and slow hybrid modes of an asymmetric loaded PC slab waveguide. On the other hand, the TM-like PC slab modes of the square hole PC structure are below the normalized frequency of a/λ=0.25; thus they all are below the operating frequency band of polarization rotator.

The presence of a PC slab mode within the frequency band of the slow and fast modes contributes to the propagation loss. Low loss propagation for the slow and fast defect modes takes place at normalized frequencies higher than 0.265 where the attenuation of the PC slab modes has increased significantly. This inhibits the detachment of energy away from the guided mode, meaning low-loss propagation takes place within a narrow band frequency 0.265-0.267.

To verify the discussion presented in previous paragraph, 3D-FDTD simulations were repeated for other frequencies. The frequency dependency of the polarization conversion is plotted in Figure 4.21. A polarization conversion efficiency higher than 75% takes place within normalized frequency band of 0.265-0.267. Maximum power exchange takes place at a normalized frequency of 0.265 and it drops off fast at frequencies above and below the frequency point of 0.265.

To show the presence of the TM-like PC slab modes, a contour map of H_y component at a/λ=0.263 is plotted in Figures 4.22. The PC slab modes presented in Figure 4.22 verifies our previous discussion.

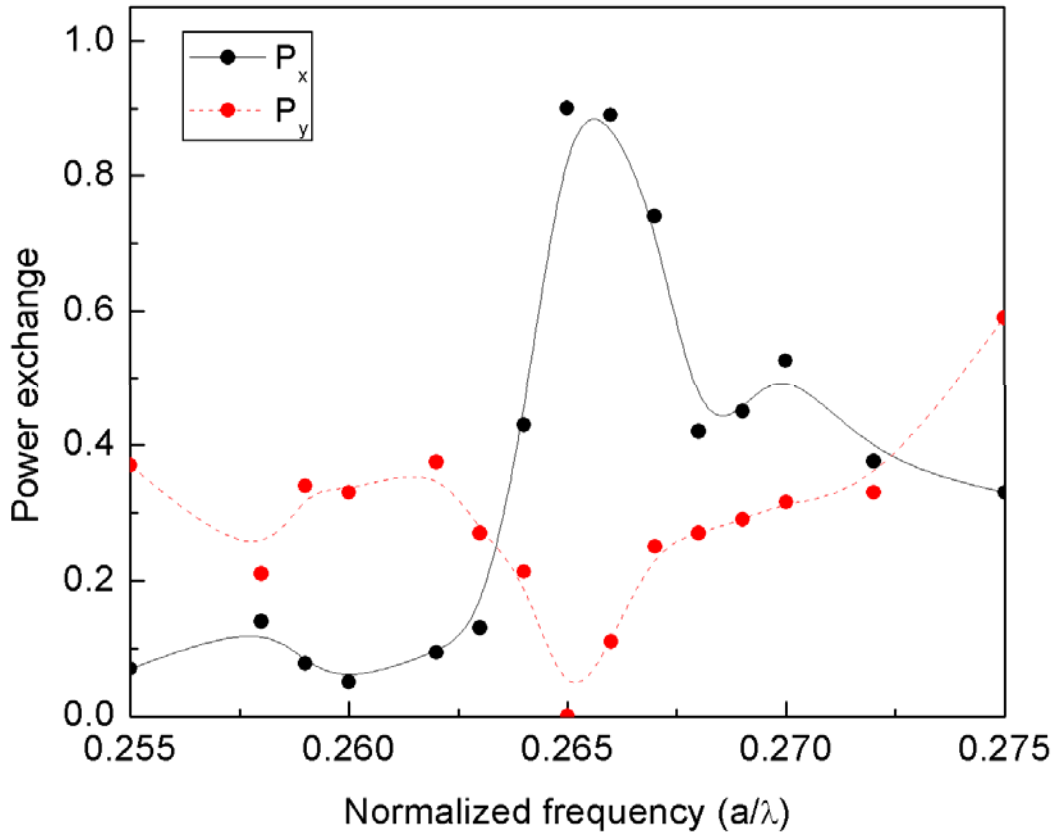

Figure 4.21 Power exchange versus normalized frequency for circle air holes PC based polarization converter (t_{up}=0.2a, r= r=0.47/2(1+√2)w (w=0.6a) and t=0.8a).

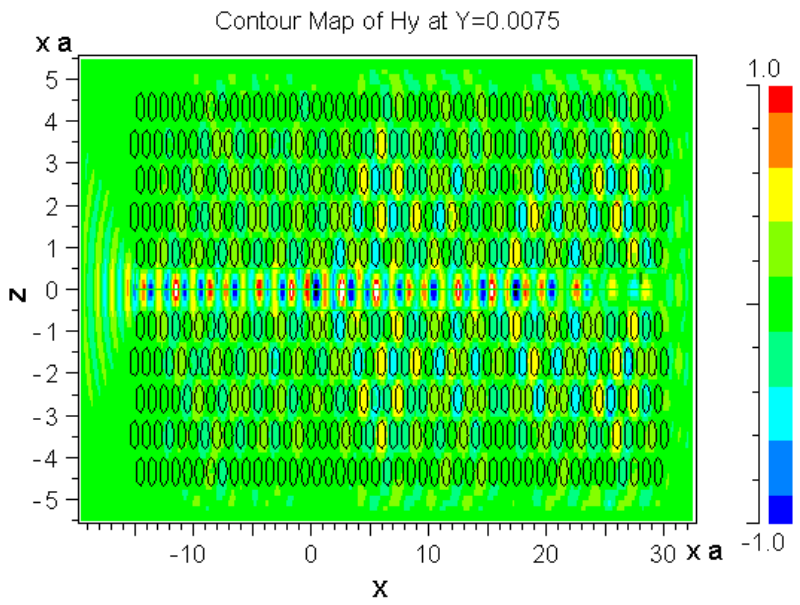

Figure 4.22 Contour map of H_y component for a/λ=0.263 obtained by 3D-FDTD simulation (t=0.8a, t_{up}=0.2a, $r = 0.47(1+\sqrt{2})w$, a=132.5 μm, n_{si}=3.48).

The circular hole PC slab based polarization rotator has a maximum power conversion efficiency of 90% which is less than that of a square hole PC slab based polarization rotator. We suspect the additional loss is due to the PC slab mode.

We can conclude this section by remarking the advantages of a square hole over a circular hole PC slab based polarization rotator. A square hole PC slab polarization rotator provides better performance in terms of bandwidth and loss characteristics. For a square hole PC based polarization rotator the P.C.E is higher than 90% within the normalized frequency band of 0.257-0.267. On the other hand, a circular hole PC based polarization rotator has a lower P.C.E of 75% within a much narrower frequency band of 0.265-0.267 which is very narrow band.

To conclude the design portion of this work we make the following observations:

- The overlap between the x-polarized and y-polarized guiding can be adjusted by varying the thickness of the PC slab waveguide.
- Ultra-compact polarization controlling devices can be implemented utilizing a PC structure.

- A periodic asymmetric loaded PC slab waveguide was introduced as polarization rotator device.
- For a quick and preliminary design, the coupled-mode theory based on semi-vectorial modes was developed for square hole PC structure.
- Another design methodology based on asymmetric loaded PC slab waveguide vector-propagation characteristics for hybrid modes was introduced for PC structures with an arbitrary hole geometry.
- Design methodology based on vector-characteristics of hybrid modes the give the exact solution of the structure.
- The design was refined and verified using a rigorous electromagnetic numerical method (3D-FDTD). The 3D-FDTD simulations verified the robustness of the design methodologies presented in the previous steps.
- A polarization conversion efficiency higher than 90% was achieved within the normalized frequency band of 0.258-0.267 for square shape PC based polarization rotator. The total length of the device was 12λ.
- The design was extended to a circular hole PC structure. In the process of changing the shape of air holes, it is important to keep the filling factor of dielectric material per unit cell constant to preserve the band structure characteristics.
- A polarization conversion efficiency higher than 75% takes place within normalized frequency band of 0.265-0.267 for a circular hole PC polarization rotator. The total length of the devices is 8λ. Maximum power exchange takes place at normalized frequency of 0.265 and it drops off fast at frequencies above and below.
- The additional loss in a circular hole PC polarization rotator is attributed to the TM-like PC slab modes. In a finite PC structure, TM-like PC modes are introduced to the lower edge of the bandgap calculated by the PWEM. The PC slab modes are extended deep inside the bandgap and overlap with the Bloch modes. Whereas, in a square hole PC polarization rotator, the TM-like PC slab modes are below the normalized frequency of $a/\lambda=0.258$, the operating frequency

of the structure. Thus, highly efficient, and wide band polarization conversion takes place for square hole PC polarization rotator.

Chapter 5

Fabrication and process development

5.1 Introduction

This chapter presents the processes developed for the fabrication of the PC structures in both optical and THz frequency bands. Two different approaches were followed to make these PC structures. For the making of PCs in an optical frequency band, amorphous silicon oxynitride (a-SiON) thin films with engineered refractive indices were developed by a Plasma-Enhanced Chemical Vapor Deposition (PECVD) technique and used to implement the PC slab waveguides. For the THz band, a highly resistive Silicon On Insulator (SOI) material was used to implement the PC structures.

Fabrication of the PC structures often involves patterning the PC structure and then etching the structural PC material. Depending on the frequency band of interest, the lithography or etching processes can be challenging. Lithography becomes challenging for optical frequency band, because of the need for very fine feature sizes (few hundreds of a nanometer). The etching process, however, becomes more challenging at long

wavelengths, for example, in THz frequency band, since there is need for a very deep (tens of micrometers) anisotropic etching process.

In section 5.2, we present the development of a-SiON films as versatile photonic materials which can be grown at low temperatures (<300˚C) and can yield refractive index values in a very wide window. Some of the key characteristics of this technology including the low temperature nature of the material growth process, as well as the controllability of the refractive index in a wide range, this technology can be integrated with any optoelectronic platform technologies including GaAs optoelectronic devices, and CMOS based electronic devices. In section 5.3, the development of a new PC membrane technology on a SOI wafer is presented for fabrication of the PCs for the THz frequency band. This technology enables realization of variety of low loss THz waveguide, resonators, and polarization processing devices on a single SOI chip.

5.2 Platform independent PC slab technology for optical frequency band

Currently, the silicon-based PCs rely on Silicon On Insulator (SOI) wafers. SOI-PCs can be integrated with SOI CMOS Integrated Circuits (ICs) with some modification of the fabrication process, but, the SOI-PC technology suffers from several major drawbacks: (i) This technology offers no control on the thickness and refractive indices of the film and the cladding layers; (ii) the technology is solely limited to SOI-CMOS technologies; (iii) the integration of PCs in SOI-CMOS require modifications in the early stage of the fabrication process, prior to making MOSFETs; the PC fabrication has to be conducted by the IC manufacturing company; and (iv) the area used for making PC structure cannot be used for making active electronic devices . Basically, in SOI-CMOS technology, the thickness of the active Si layer is optimized for MOSFET performance and is fixed. Also, there is no freedom in choosing the film, the cladding materials, or the refractive indices. Furthermore, most of the conventional CMOS chips (>90%) do not use SOI substrates. Therefore, this technology cannot be generalized for many applications.

Silicon oxynitride films, grown at medium to high temperatures using a low pressure CVD technique, has previously been reported for realizing conventional Optical Integrated Circuit (OIC) [113-114]. It had been shown that the refractive index of such

films can be engineered to a range of refractive index between 1.45-1.9. Nevertheless, a-SiON films along with a-Si films, grown using tPECVD technique, offers a low temperature PC technology which can be integrated with a variety of optoelectronic and IC technologies.

In this work, we introduce a low temperature (<300˚C) a-SiON thin film technology for integration with IC technologies. Figure 5.1(a) shows the structure of an a-SiON optical integrated circuit on top of an electronic chip without affecting the underlying devices. Figures 5.1(b) and 5.1(c) show two versions of a-SiON PC technologies, where both structures utilize a high refractive index film sandwiched between cladding layers to achieve an optically symmetric structure. The top PC structure utilizes air holes to achieve maximum contrast while the bottom structure uses the cladding layer to achieve a lower contrast PC.

This technology provides significant freedom in engineering the thicknesses and the refractive indices of the films. The major advantages of this technology over the conventional SOI-PC technology are: (a) the thickness and the refractive indices of the film layer as well as the cladding layer can be engineered for a variety of PC device applications. The thickness of films in a PECVD growth can be controlled with nanometer resolution. The freedom in choosing the thicknesses and refractive indices of the utilized films offers an excellent opportunity for the optimization of OICs based on this technology. (b) The low temperature nature and the platform independence of the proposed technology allows it to be integrated in any IC technology including Si and GaAs integrated circuits. (c) The PC-OICs can be implemented on top of the electronic circuits using interlayer dielectric and metal layers to isolate optical and electrical signals. Therefore, the area of the resulting optoelectronic chips can be efficiently reduced.

In the proposed technology, the intermediate layer (lower cladding layer) between the substrate and the core of the PC, is a low refractive index a-SiON. The core layer is a high refractive index a-SiON or a-Si:H. The holes are filled with either a-SiON or air. PECVD grown films are normally conformal, therefore it is possible to completely fill the holes using the cladding material.

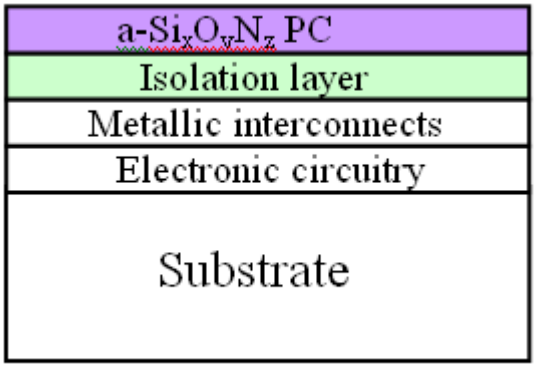

(a)

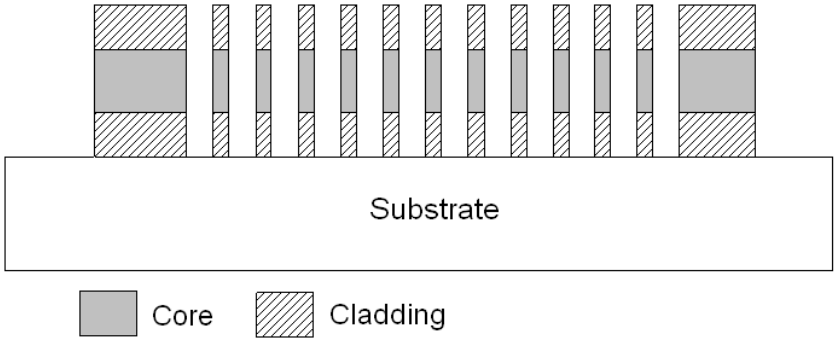

(b)

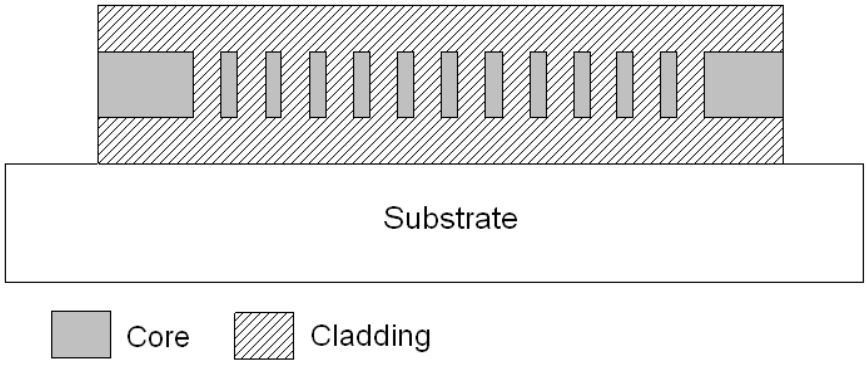

(c)

Figure 5.1 (a) The structure of the proposed PC for integration in IC technology. (b, c) Two different configurations for a-SiON:H based PC.

To demonstrate the proposed approach, the structures were simulated and analyzed. a-SiON films of different refractive indices were developed, and the structure in Figure 5.1(b) was fabricated. The films were deposited with different gas flows of

SiH_4, N_2O, and NH_3. For the development of the films, the deposition rate, thickness, refractive index, stoichiometry and the composition of the films were characterized by surface profiling, spectroscopic ellipsometry, Rutherford Back-Scattering (RBS), and Fourier Transform Infra Red (FTIR) spectroscopy.

5.2.1 Development of a-SiON films and fabrication of a-SiON based PC slab waveguides

The a-SiON films were deposited by a standard PECVD system running at 13.56 MHz at 300°C. Silane, nitrous oxide, and ammonia were used as the gas phase precursors. The pressure and RF power were fixed at 250 mTorr and 40 W (31 mW/cm^2). Two sets of experiments were conducted to develop films with different refractive indices. First, silane and amonia flow rates were fixed at 8 sccm (standard cubic centimeter per minute) and 80 sccm, and the flow of N_2O was varied from 0 to 80 sccm to grow low refractive index films. Then the silane and N_2O flow rates were fixed at 8 sccm and 80 sccm, and the flow of NH_3 was varied between 0 and 80 sccm to grow high refractive index films. To achieve very high refractive index films, intrinsic a-Si:H films were deposited using the PECVD technique and the following process conditions: pressure of 250 mTorr, RF power of 12 W, temperature of 300 ^oC, SiH_4 flow of 40 sccm and the deposition time of 8 minutes.

Spectroscopic ellipsometry was used to measure the refractive index of the films in the range of 400 nm – 900 nm. The refractive indices of the films at 630 nm were used for comparing films of different compositions. To measure the refractive indices of the films using ellipsometer, films of about 100 nm thickness were deposited on crystalline Si substrates. To enhance the precision of the ellipsometry, the thickness of the films were measured by patterning the films using conventional lithography and thickness measurement by the Dektak 8 surface profiler.

To study stoichiometry and the bonding of the films using RBS and FTIR measurements, films of 500 to 700 nm thicknesses were deposited on (p-type) c-Si substrates having resistivity of 8 to 12 Ω-cm.

Low temperature PECVD based PCs were made using a 300 nm intrinsic a-Si:H film layer sandwiched by a 100 nm thick a-SiON cladding layers on top of a

Corning 1737 glass substrate. The structural parameters were designed for a central wavelength of 1.55 μm. Due to the spectroscopy ellipsometery system being limited to 900 nm, we were not able to measure the refractive index of the deposited layers at λ=1.55 μm. For an accurate design, the refractive index of the film and cladding layers must be measured at λ=1.55 μm. For realizing air holes in the PC structure, an Electron Beam Lithography (EBL) followed by an anisotropic reactive ion etching process using CF_4/O_2 gas mixture was used. First the EBL was used to transfer the design onto the PMMA. Then holes were etched by Reactive Ion Etching (RIE) using the PMMA as the soft mask. The RIE process conditions were optimized to achieve anisotropic etching with right angle sidewalls.

5.2.2 Results and discussion

5.2.2.1 Thickness and refractive index measurement of a-SiON

Figure 5.2 shows the measured refractive index at λ=630 nm and the deposition rate (nm/sec) of the developed a-SiON films as a function of gas flow rates. As it was mentioned before, spectroscopic ellipsometry was used for the measurement of the refractive indices of the deposited films.

The increase in the NH_3/SiH_4 flow, while keeping N_2O constant at 80 sccm, results in an increase in the refractive index and decrease in the deposition rate. On the other hand, the increase in the N_2O/SiH_4 flow, while keeping NH_3 constant at 80 sccm, results in decrease in the refractive index of the film and increase in the deposition rate. By varying the gas flows, a-SiO, a-SiON, and a-SiN films were achieved. The refractive indices in the range of 1.43 – 1.75 were achieved where 1.43 and 1.75 refer to the refractive indices of a-SiO and a-SiN films, respectively. A refractive index of 3.4 was measured for a-Si:H film deposited on corning 1737 glass substrate. The very high refractive index of the a-Si:H layer allows it to be used as the film layer in high contrast PC structures.

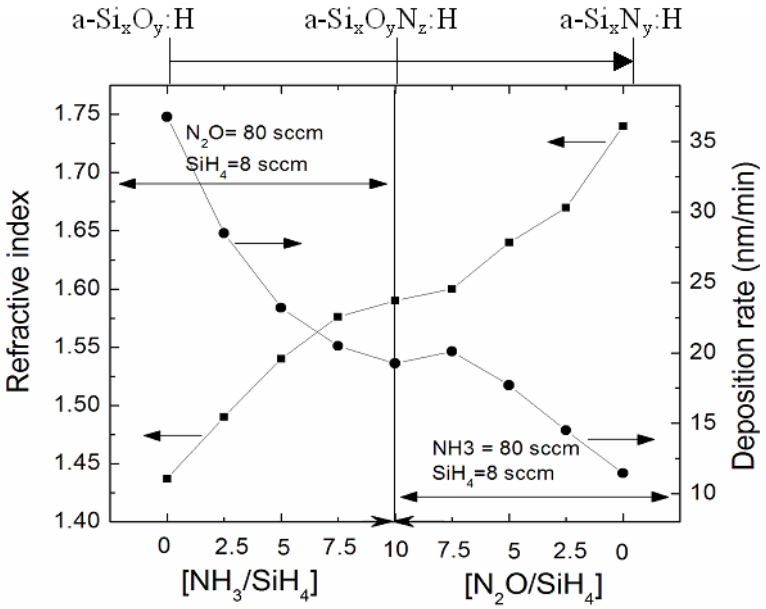

Figure 5.2 Deposition rate and the refractive indices of the thin layers of a-SiON (≈ 100 nm) as a function of the gas flow ratios. The refractive indices were measured by ellipsometer at the wavelength of 630 nm.

These sets of experiments show that the refractive index of the PECVD a-SiON material system can be engineered in a very wide range of 1.43 to 3.4. Such flexibility in refractive index can be utilized for implementation of many new devices.

5.2.2.2 RBS and FTIR of a-SiON films

The composition and stoichiometry of the a-SiON films were characterized by RBS and FTIR spectroscopy. Table 5.1 summarizes the RBS measurement results with a NH_3 flow of 80 sccm, which results in a higher refractive indices (right side of Figure 5.2). Similarly Table 5.2 summarizes the RBS measurement results with a N_2O flow of 80 sccm, which results in a lower refractive indices (left side of Figure 5.2).

Comparing materials in Table 5.1 with a Stoichiometric Silicon Nitride (Si_3N_4) material, manifests that the films are nitrogen rich. Moving towards right side of the Table, the oxygen content of the films increases, hence the refractive index of the materials decreases. On the other hand, the materials presented in Table 5.2 are oxygen rich leading to a lower refractive indices. The right side of the Table 5.2 shows, the oxygen content of the films decreases and leads to the increase in the refractive index.

Element	(a) N_2O/SiH_4=0 AF	(b) N_2O/SiH_4= 2.5 AF	(c) N_2O/SiH_4= 5 AF	(d) N_2O/SiH_4=10 AF
n	1.75	1.673	1.64	1.59
Si	1	1	1	1
O (x)	0	0.71	0.75	1.2
N (y)	2	1.43	1.5	1.3
H (z)	0.1	0.1	0.1	0.1

Table 5.1 Atomic fractions (AF) of the single elements of 0.5 μm thick a-SiON layers measured for several gas flow ratios of N_2O/SiH_4 and constant gas flows of SiH_4=8 sccm and NH_3=80 sccm.

Element	(a) NH_3/SiH_4=0 AF	(b) NH_3/SiH_4= 2.5 AF	(c) NH_3/SiH_4= 5 AF	(d) NH_3/SiH_4= 10 AF
n	1.437	1.47	1.54	1.59
Si	1	1.3	0.7	1
O (x)	2.5	2.2	0.8	1.2
N (y)	0	1.1	0.5	1.3
H (z)	0.1	0.1	0.1	0.1

Table 5.2 Atomic fractions (AF) of the single elements of 0.5 μm thick a-SiON layers measured for several gas flow ratios of NH_3/SiH_4 and constant gas flows of SiH_4=8 sccm and N_2O=80 sccm.

RBS is sensitive to the density of the constituent atoms, but it does not provide information about chemical bonding of the constituent elements. In other words, RBS cannot detect what percentage of the Si atoms participates in the SiN, SiO, or SiH bonds. FTIR is a powerful characterization technique that can be used to determine chemical bonding composition of the films. Figure 5.3 shows the IR-absorption spectrum of the a-SiON deposited films measured at our laboratory. The plots (a)-(e) were obtained for five different gas flow ratios of N_2O/SiH_4 and with a constant ammonia gas flow (NH_3=80

sccm). Where as, the plots (e)-(i) were obtained for the five different gas flow ratios of NH_3/SiH_4 and constant N_2O gas flow (N_2O=80 sccm).

The IR-absorption bands are summarized as the following: a N-H stretching vibration centered at about 3335 cm^{-1} (λ= 3 μm) and an additional weak feature at 1545 cm^{-1}(λ= 6.47 μm), a N-H bending vibration near 1175 cm^{-1}(λ= 8.51 μm), a Si-H vibration near 2300 cm^{-1}(λ= 4.35 μm), an O-H stretching vibration near 3650 cm^{-1}(λ= 2.74 μm), a Si-N stretching vibration at 830-890 cm^{-1}(λ= 11.2 - 12 μm), and Si-O stretching and bending vibrations at 1050-1080 cm^{-1} (λ= 9.26 - 9.52 μm) and 800 cm^{-1}[113-114]. The gas flow ratios of N_2O/SiH_4 samples (a), (b), (c), (d) and (e) are 0, 2.5, 5, 7 and 10, respectively. With increasing the gas flow ratio of N_2O/SiH_4, the Si-O stretching bonds becomes stronger and Si-N stretching band at 830-890 cm^{-1} (λ= 11.2 - 12 μm) becomes weaker. Moreover, the N-H band at 3335 cm^{-1} (λ= 3 μm) becomes weaker.

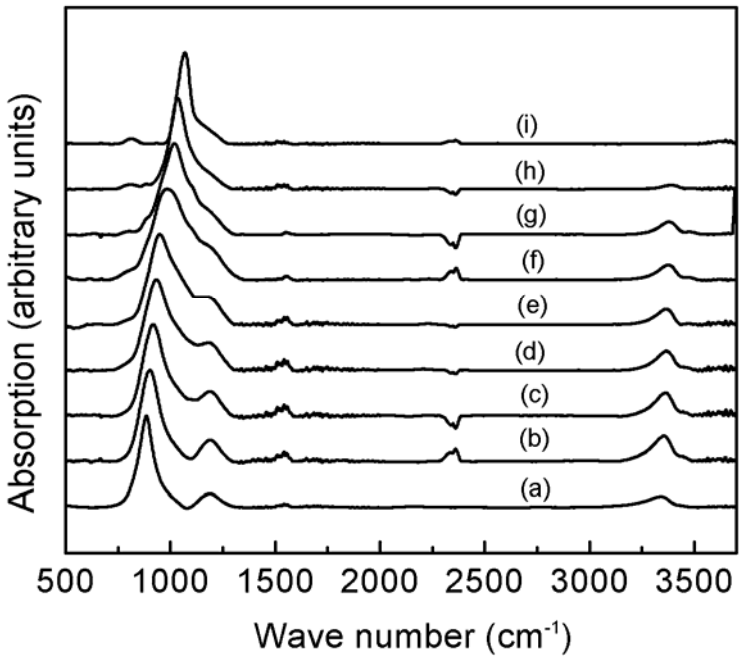

Figure 5.3 IR-absorption spectra for 0.5 μm thick a-SiON films as deposited by PECVD with constant NH_3 gas flow of 80 sccm and different gas flow ratios of N_2O/SiH_4 of (a) 0 (b) 2.5 (c) 5, (d) 7.5 and (e) 10 and constant N_2O gas flow of 80 sccm and different gas flow ratios of NH_3/SiH_4 of (f) 7.5 (g) 5 (h) 2.5 and (i) 0.

This is consistent with the results of the RBS measurement on the samples (a)-(d) in table 5.1. On the other hand, for samples (e), (f), (g), (h) and (i), the gas flow of N_2O is

80 sccm and the gas flow ratio of NH_3/SiH_4 are 10, 7.5, 5, 2.5 and 0, respectively. As the gas flow ratio of NH_3/SiH_4 reduces, the Si-N stretching band at 830-890 cm^{-1} becomes weaker, while the Si-O band at 1050-1080 cm^{-1} becomes stronger. The N-H band at 3335 cm^{-1} becomes very weak. This is also consistent with the results of the RBS measurements on samples (a)-(d) in Table 5.2.

To study hydrogen bonding in the material we ran Rapid Thermal Annealing (RTP) at 750°C for the duration of 10 minutes. Figure 5.4 shows the FTIR spectrum of the a-SiON layer with gas flow ratio of N_2O/SiH_4=5 before and after annealing. Substantial reduction of N-H bonds at 1545 $cm^{-1}$and 3335 cm^{-1}, and O-H bonds at 3650 cm^{-1} were observed. This means that hydrogen has been out diffused as a result of annealing. The N-H bonds at wave number 3350 cm^{-1} contributed to the loss at the wavelength of 1510 nm, and its low energy tail leads to an unwanted absorption loss in the wavelength region of interest (1545-1565 nm) [5].

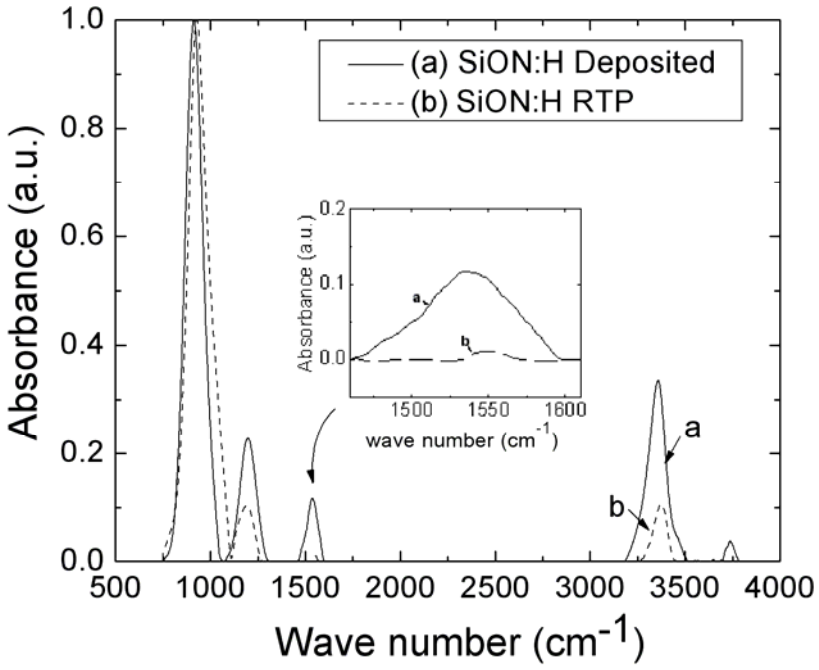

Figure 5.4 IR-absorption spectra of 0.5 μm thick a-SiON film with gas flow ratios of N_2O/SiH_4 of 5 before and after RTP carried out at 750° for the duration of 10 minutes.

By performing rapid thermal annealing on the films, it substantially reduced the absorption peak at 3350 cm^{-1}. Moreover, the tail of the bond has been diminished at a large extend.

Both RBS and FTIR confirm the results obtained from the ellipsometery, where nitrogen rich films show higher refractive index than that of oxygen rich films. The consistency of the characterization results suggest that the optical materials developed in this work are stable, reliable, and the PECVD experiment is reproducible.

5.2.3 Design and analysis of a-SiON based PC

As shown in Fig. 5.2, the refractive index of films can be engineered in a wide range of, 1.43 to 1.75. Addition of the a-Si material, with a refractive index of 3.4 into the developed material system results in a very versatile optical material system that can be utilized for developing variety of PCs with different band gaps. Low contrast symmetric PCs can be implemented using a-SiON material as the film layer. High contrast symmetric PCs, on the other hand, can be implemented using a-Si material as the film layer.

Figure 5.5 shows the propagation loss for a PC slab waveguide with the propagation length of 20 μm. It was calculated using the Three-Dimensional Finite Difference Time Domain (3D-FDTD) method for a low contrast single defect line PC slab waveguide for the TM-like wave, shown in Figure 5.5.

The refractive indices of the cladding and core layers are 1.43 and 1.7. The cross section of the structure is as shown in Figure 5.1(b). The thickness of the core and cladding layers are 0.75a and 0.3a. The radius of air holes are r=0.4a. Figure 5.5 shows that the propagation loss is quite low within the normalized frequency band of 0.38-0.45. Assuming that a normalized frequency of 0.41 corresponds to the free space wavelength of 1.55 μm, the unit cell size would be 0.635 μm that is almost 1.6 times the size of the unit cell of high contrast (SOI based) PC structures. Thus, low contrast PC offers the advantage of larger feature sizes in comparison with high contrast PC.

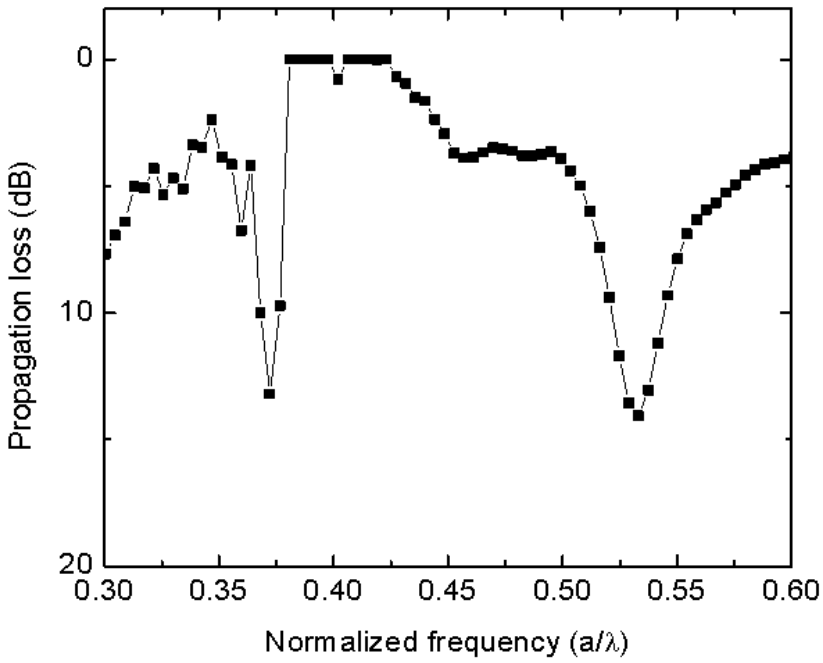

Figure 5.5 The loss diagram for single defect line PC slab waveguide with 20 μm propagation length and the core and cladding refractive indices of 1.7 and 1.43.

Figure 5.6 shows the bandgap map of a triangular PC slab, having an a-Si film layer and an a-SiON cladding layer, for both TE-like and TM-like waves. The radius of the air hole and thickness of the film layer in this simulation were 0.3a and 0.75a. The cross section of the structure looks like the configuration depicted in Figure 5.1(b).

By increasing the refractive index of the cladding layers from 1.42 to 1.8, the band gap size for the TM-like wave reduces from 0.045 to 0.0155. The band gap sizes for the TE-like waves are very small and have no overlap with the TM-like wave. Therefore, the band gap properties are strongly dependent on the refractive indices of the cladding layer.

The aforementioned results suggest that the band gap of a-SiON based PC technologies can be engineered by changing the contrast between the refractive index of the film and the cladding layers. This can be easily done by changing the gas flows and process conditions during the deposition of the films. This is extremely important and can be considered as a major advantage of this technology over the widely discussed SOI-PC technology, where the band gap of the PC is fixed.

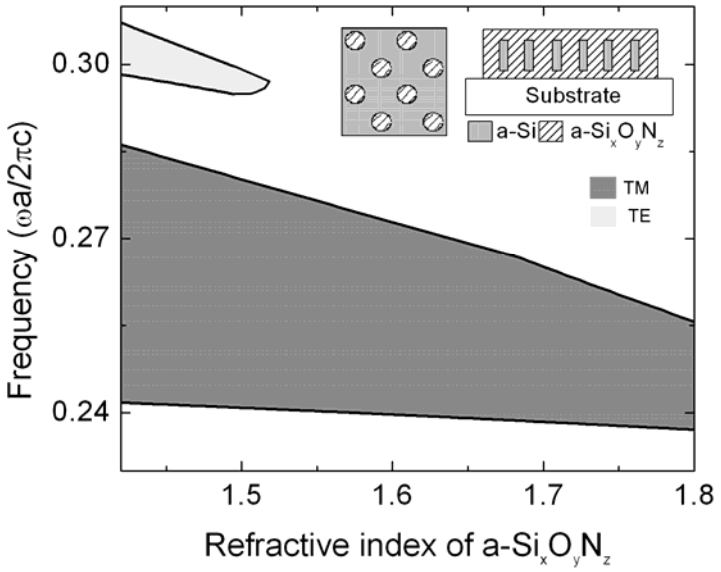

Figure 5.6 Gap map which graphs the band gap size versus the refractive index of the a-SiON film layer for triangular PC with *r=0.3a*, *t=0.75a* for both TE-like and TM-like waves for the configuration illustrated in Figure 5.1 (b).

5.2.4 Fabrication of a-SiON based PC

The PC waveguide, formed by removing one row of holes along the z-direction (Figure 3. 1), was fabricated. The lattice constant of the PC and the radius of the holes are 411 nm and 123 nm. These structural parameters are obtained by assigning the central bandgap normalized frequency of $a/\lambda=0.265$ to a free space wavelength of $\lambda=1.55$ μm. To fabricate the PC waveguide, 100 nm a-$Si_{0.7}O_{0.8}N_{0.5}$:H with the refractive index of 1.54 was deposited on a Corning 1737 glass wafer followed by deposition of 300 nm a-Si and 100 nm a-$Si_{0.7}O_{0.8}N_{0.5}$:H.

To etch the holes, a resist, PMMM, was spun on the surface. EBL was utilized to pattern the resist (exposing the resist) and selectively removing the resist (developing). EBL is a maskless lithography system that overcomes the limitation of diffraction of light. This means very small features in the range of nm can be realized. The desired pattern is supplied to the EBL machine so that it was programmed to write a pattern on the resist using an electron beam. The main limitation of the EBL system is throughput. It takes a long time to cover the whole surface of the silicon or any other wafer. This makes it not suitable for high volume manufacturing where the throughput is very important

[115]. After patterning the PMMA using the EBL, an anisotropic reactive ion etching was employed to etch the a-$Si_{0.7}O_{0.8}N_{0.5}$:H and a-Si.

Figure 5.7 shows the SEM of the fabricated a-Si and a-$Si_{0.7}O_{0.8}N_{0.5}$:H based PC slab waveguide. The taper seen in the SEM pictures was implemented to facilitate the coupling of the light into the input waveguide. The width of the input waveguide is 535 nm which was tapered out to 10 μm. Figure 5.7 shows the successful implementation of the proposed technology. Both EBL patterning and the anisotropic reactive ion etching were successfully performed in deep submicron scales.

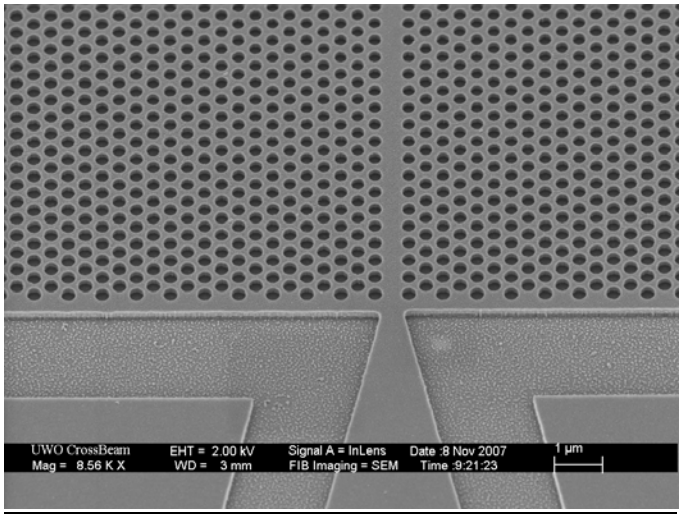

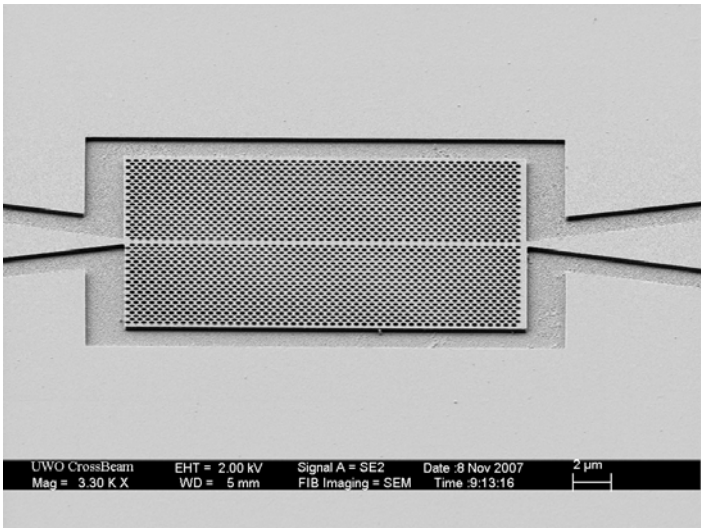

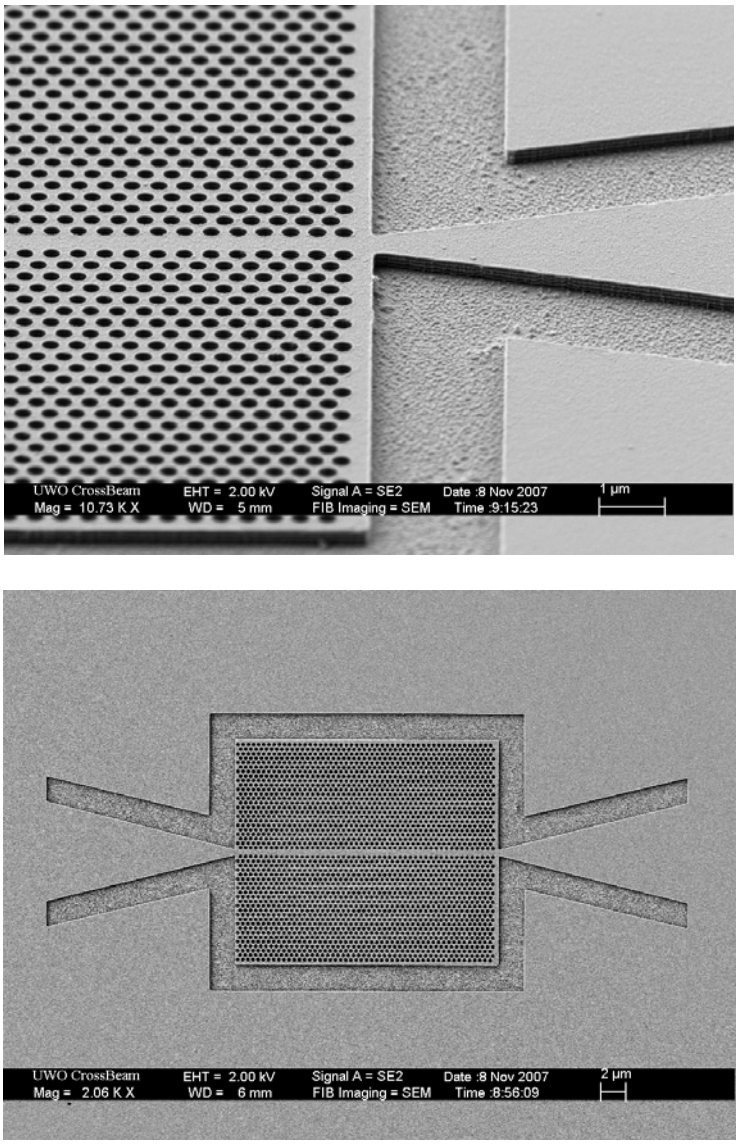

Figure 5.7 SEM picture of the fabricated a-$Si_{0.7}O_{0.8}N_{0.5}$:H -a-Si photonic crystal waveguide

5.3 PC membrane technology for THz application

In this section, the fabrication process of the Si membrane PC technology for THz application is presented. Finding a lossless transmission media for the THz wave has been the topic of research for many THz groups over the last decade [34-36]. The THz signal is strongly absorbed by moisture, and so, THz propagation in the atmosphere would experience a huge propagation loss due to the presence of moisture in air [116]. This makes it very important to find a low loss media for the THz transmission. Metallic waveguides utilized in microwave frequencies are lossy media for the THz wave due to the penetration and absorption of the THz wave in metal [117-119].

It is shown that highly resistive silicon (>3 kΩ-cm) provides a lossless media for THz wave propagation [120]. In this thesis, we have employed highly resistive silicon (> 5-10 kΩ-cm) to implement PC based membrane structures for THz applications. There are some research groups that have utilized PC technology for THz application [121-122]. For example, a metallic PC in a parallel waveguide was implemented and tested for a THz frequency band [122]. SU8 was employed to create few rows of PC rods, by sputtering silver, the metallic PC rod were implemented and tested. The bandgap measurement was reported utilizing THz pulse was centered at f=600 GHz. The application was limited to pure PC structure. Jukam et al reported the implementation of a PC structure on highly resistive thin silicon layer and bandgap measurement of the PC structure [121]. There is no report on the implementation of a PC slab waveguide structure for THz application. Moreover, handling and integration of PC structures on thin silicon layers are not convenient or practical.

Here, we introduce a novel PC technology for the THz wave that is a potential candidate as a compact and low loss media for THz wave propagation. More importantly, this technology has a potential for integration. In the following section, the details of the fabrication process are presented.

5.3.1 Fabrication process of THz PC membrane structure

The PC membrane technology has been developed on SOI wafer. SOI wafer for THz application is composed of highly resistive silicon layer (5-10 *KΩ-cm*) that is called a device layer. A buried oxide layer separates the device layer from ‘handle’ silicon.

Handle silicon is low resistive silicon making it a lossy medium for THz wave propagation. We fabricated devices in the frequency band of 500 GHz - 3 THz. The thickness of the device layer is chosen between 100 μm and 135 μm based on the design. The thickness of the buried oxide layer that separates the silicon device layer from the silicon handle layer could be varied between 0.5 μm-5 μm. Handle silicon layer is a low resistive silicon that attenuates the THz signal significantly and must be taken into consideration in the fabrication technology design.

The fabrication process consists of both front side and backside processing of the SOI wafer. The front side processing involves etching of deep holes into the silicon layer. Backside processing consists of opening window at the backside of the devices to prevent coupling of the THz wave to the lossy substrate modes and guarantee low loss propagation.

To pattern the device layer, standard lithography is utilized as opposed to the optical PC structure that requires nanometer range lithography. In order to etch deep holes (> 100 μm), Deep Reactive Ion Etching (DRIE) is required. Thick photoresist must be utilized for photolithography in order for it to stand the long etching process. We employed 4 μm thick photoresist (S1827) as a soft mask for the DRIE process. In working with thick photoresist special guidelines must be observed. First of all, the exposure time must be increased and adjusted to provide enough energy to the bottom of the resist. The exposure dosage and time directly affects the sharpness of the walls.

After spinning the resist, the sample must be kept at room temperature for 15-20 minutes. This allows most of the solvent to be evaporated prior to soft-baking. Otherwise, the surface will dry very fast and the trapped solvent at the bottom will form bubbles that lift the resist and leave defects in the pattern. Also, the standard resist creates a lot of nitrogen that can not escape from the thick resist. Trapped nitrogen would lift the resist and create defects in the pattern. It is recommended to utilize a hot plate for baking the resist instead of an oven. In hot plate baking the hot temperature is conducting from the bottom to the surface; thus, the solvent at the bottom can be evaporated first. On the other hand, with oven baking the surface will be dried out first resulting in a crust on the surface that obstructs nitrogen and solvent escape. Multiple coatings while baking in-

between, is also helpful to reduce the defects. The in-between baking must be carried out at temperatures less than 90^0C.

Furthermore, the development process must be optimized to create a thick resist. A high exposure dosage limits the dissolution rate. Following these guidelines will help to reduce the density of the defects significantly.

The etching of the holes was carried out using an optimized DRIE process to create holes with smooth vertical side walls and the desired aspect ratio. We used the Bosch process which alternates between two modes of nearly isotropic plasma etching using SF_6 for 7 sec and deposition of chemically inert passivation layer using C_2F_8 for 2 sec. The SF_6 and C_2F_8 flow rates are 300 sccm and 150 sccm, respectively. The process temperature is kept at 20^oC. The etching rate is around 5μm/min, and can vary slightly during the etching process. Buried oxide acts as an etch stop. The etching ratio of oxide to silicon is 10^{-3}, which can act as an etching stop for Silicon. After etching, photoresist was removed by resist striper.

The second phase of the process is opening a window at the backsides of the SOI wafer to construct the membrane PC structure. Handle silicon is a thick silicon (525 μm), which is removed by wet chemical etching. We used 30% KOH etching at 90^oC, which gave an etching rate of almost 50μm/hr. For uniform etching a KOH bath was setup. More importantly, the front side of the wafer must be protected from the KOH etching. The KOH etching was carried out by a custom made wet etching tool which only exposes the backside of the wafer to hot KOH solution. KOH mask that covers the unetched areas must withstand 10 hours of KOH at 90^oC. A thick amorphous silicon nitride film (a-SiN) of 1μm, was deposited using PECVD technique to function as the hard mask at the backside of the SOI wafer. The second lithographic step was performed to pattern the SiN_{1-x} layer for the opening windows at the backside of the SOI wafer. Again buried silicon dioxide functions as the etching stop.

The SEM image of a fabricated membrane PC slab waveguide is shown in Figure 5.8 (a). It shows that the window under the active area (waveguide area) has been etched nicely. Figure 5.8 (b), is SEM picture of the top side showing the air holes close-up. It can be seen that the walls are sharply etched.

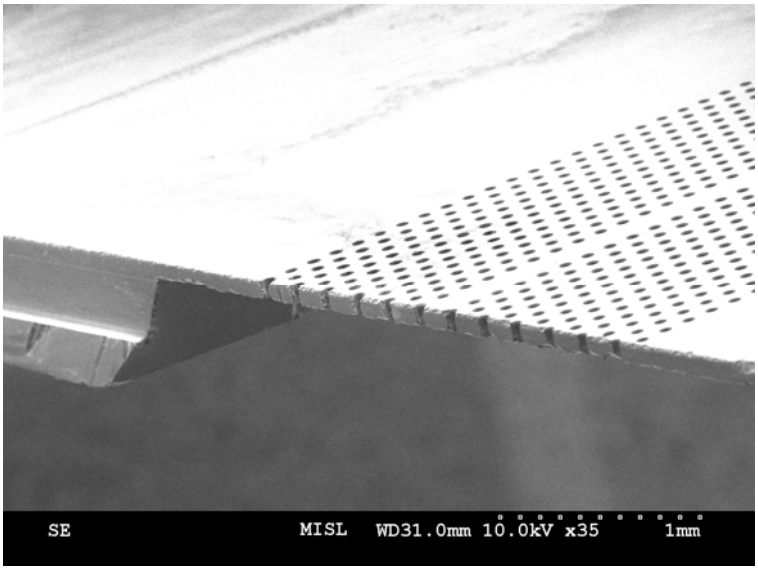

(a)

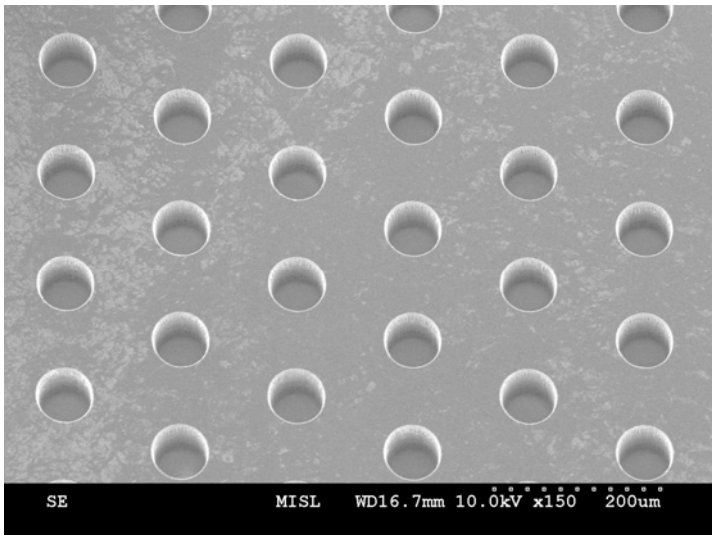

(b)

Figure 5.8 The SEM picture of (a) cross section (b) top view of the fabricated membrane PC slab waveguide for THz application.

The backside etching is also very important and critical. Figure 5.9 shows the SEM picture of the backside. It can be seen that the back is etched uniformly, the oxide at the back can be easily removed by buffered HF (BHF).

It is worthwhile to note that the order of the processes is very important. It is essential to carry out the front side process first. In the DRIE process, it is essential to maintain thermal conductivity to keep the process temperature at 20^{o}C. If the backside

were to be removed first, in the DRIE plasma chamber the backside would be filled with air; thus, the temperature would be raised leading to the melting of the mask. This could be avoided by performing the DRIE process first followed by backside etching. Handle silicon that is thermally conducting can maintain the DRIE process temperature at 20^{o} C.

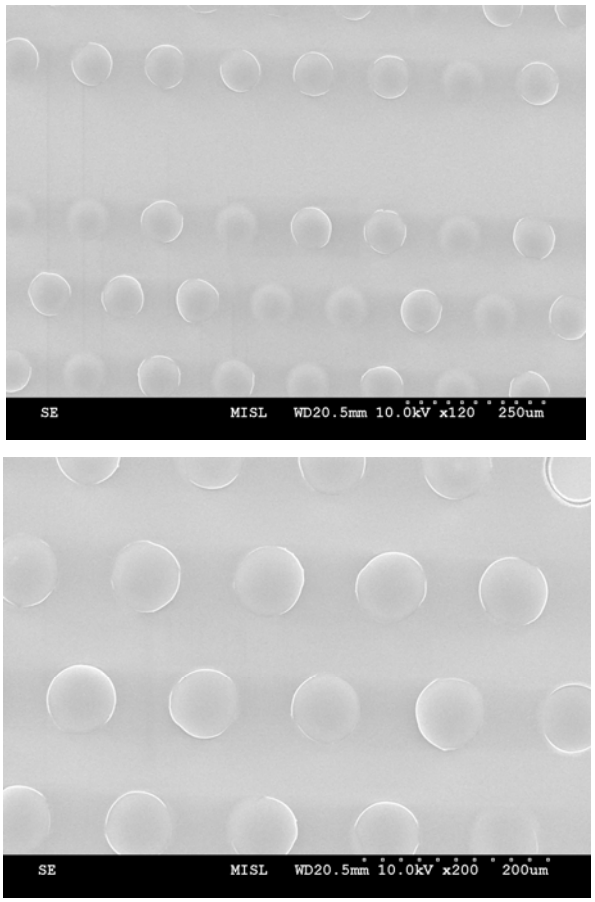

Figure 5.9 SEM picture of the backside of the fabricated PC membrane slab waveguide

5.3.2 Fabrication process of the THz PC based polarization rotator

We fabricated the polarization rotating devices for potential applications in the THz frequency band (500 GHz – 3THz). Detail design and numerical simulation/validation of this rotator has been presented in Chapter 4. The fabrication of this PC based polarization rotator is more complex in a sense that the front side processing requires two sets of masks. The first mask is employed to create the periodic loading layers. The second mask

is for patterning of the PC slab waveguide. The third mask is used to open window at the back side of the structure.

Figure 5.10 shows the SEM picture of the front side of the taper that is used to couple the input wave to the waveguide. Tapering in the PC structures is accompanied with a huge radiation loss [123-124]. In [124], it is shown that by gradually changing the thickness and radius of the air holes, the radiation loss can be reduced, however, the implementation of such structures is not easy. To avoid such complications, we etched a strip of silicon (150μm) along side the taper line so the electromagnetic field will not see the PCs. The only problem associated with this kind of taper is the low mechanical stability. Since the taper line has to be long for gradual tapering of the input waveguide and it tapers from 10 mm width down to 100 μm, as a result the taper is extremely fragile. To enhance the mechanical stability of the taper line, small unetched areas are left along the taper line as it seen in Figure 5.10. The taper has been designed using 3D-FDTD analysis to achieve low reflection and radiation loss, and a compact structure. The simulation results show that a tapering angle of 12^{o} can satisfy all the requirements.

Figure 5.11 shows the SEM picture of the periodic asymmetric loaded PC slab waveguide with square holes. The SEM picture shows that the walls are very sharp. In Figure 5.12, the SEM picture of the periodic asymmetric loaded PC slab waveguide for circular air holes pattern is presented. Finally, the top view of the structure that includes input and output tapers is shown in Figure 5.13.

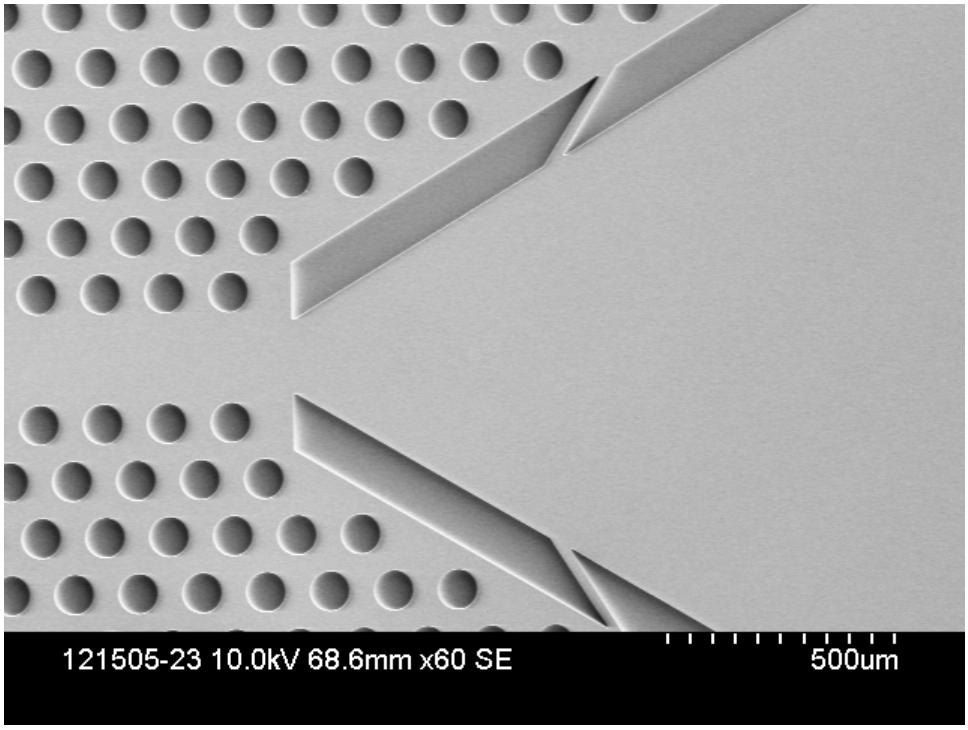

Figure 5.10 The SEM picture of the input taper of polarization rotator structure with circle air holes

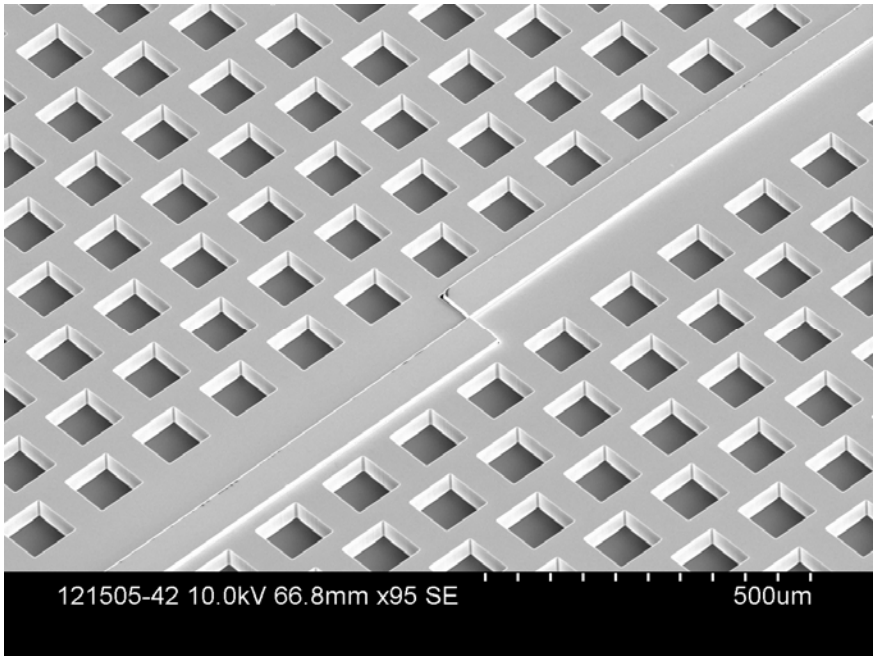

Figure 5.11 The SEM picture of the front view of periodic asymmetric loaded PC slab waveguide with square air holes.

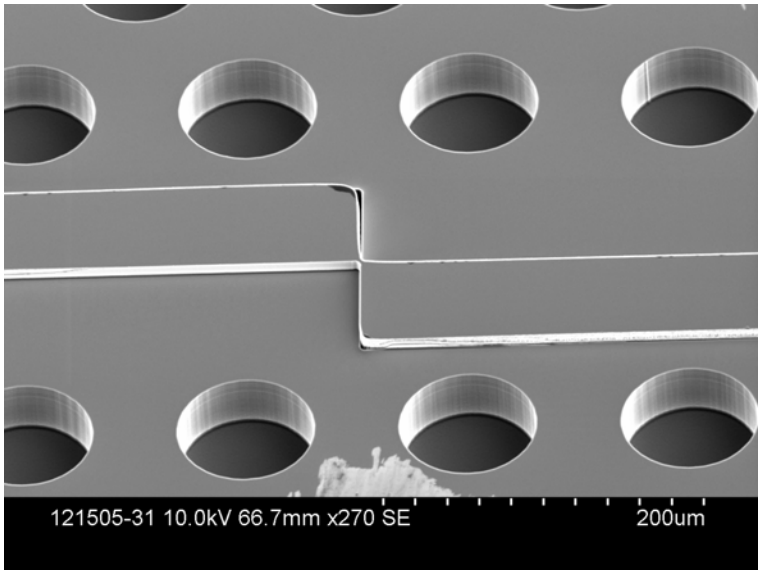

Figure 5.12 The SEM picture of the periodic asymmetric loaded PC slab waveguide with circle air holes.

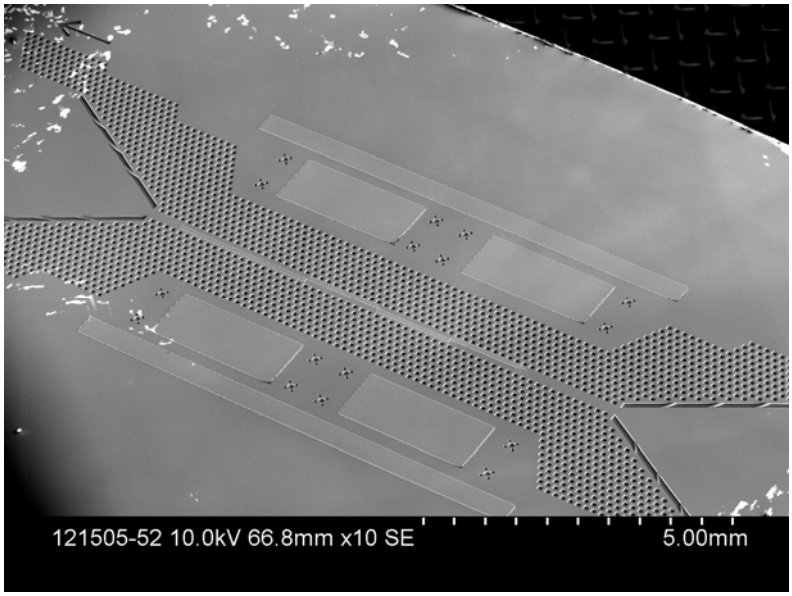

Figure 5.13 The SEM picture of the top view of the polarization rotator structure

Chapter 6

Conclusions and Future Work

6.1 Summary

The focus of this thesis was on design and fabrication of a PC slab waveguide based polarization processor devices. A summary of the key achievements are highlighted as following:

- A thorough study was conducted on the polarization dependence of the wave propagation inside a PC slab waveguide. In chapter 3, a design methodology based on PWEM and 3D-FDTD was introduced to optimize the thickness of the PC slab waveguide to achieve maximum overlap between the TE-like and TM-like guiding. Depending on the application, only one or both principal polarizations must be guided. In the same chapter it was shown that the overlap between TE-like and TM-like guiding can be varied by adjusting the thickness of PC slab waveguide.

- A novel compact PC slab waveguide based polarization rotator was introduced and designed. A PC based coupled-mode theory was developed to design the structure. The coupled-mode theory provides a simple yet closed form method for the initial design. A square hole PC was preferred to simplify of the closed-form formulations. The design was refined using rigorous 3D-FDTD electromagnetic numerical method. The simulated results verified the robustness of the coupled-mode theory for design and analysis of the PC based polarization rotator.
- To extend the design to a more general shape PC based polarization rotator, a design methodology based on vector-propagation characteristics of hybrid modes for an asymmetric loaded PC slab waveguide was introduced. The hybrid mode vector-propagation characteristics of the structure were calculated utilizing 3D-FDTD method combined with SFT. Profile and propagation constants of the slow and fast modes for an asymmetric loaded PC slab waveguide were extracted from the 3D-FDTD simulation results. The half-beat length, which is the length of each loaded layer, and total number of the loaded layers are calculated using aforementioned data. This method provides exact parameter values of the parameters of the polarization rotator structure.
- The design was extended to a circular hole shaped PC structure using hybrid mode analysis. The circular hole PC polarization rotator was more compact than the square hole PC structure, but the loss characteristics and bandwidth of the circular hole and squarehole polarization rotators were different. A circular hole PC polarization rotator is narrow band in comparison with a square hole PC polarization rotator. In circular hole PC slab structure, the Bloch mode (fast and slow modes) couple energy to the TM-like PC slab modes. In both square and circular hole PC slab structures with finite number of rows, TM-like PC slab modes are extended to the lower edge of the bandgap. In bandgap calculation through PWEM, it is assumed that the PC structure is extended to infinity, however, in practice the number of rows is limited, which is the source of discrepancy between the bandgap calculation using PWEM and 3D-FDTD. In an asymmetric loaded circular hole PC slab waveguide, the leaky TM-like PC slab

modes are extended deep inside the bandgap and overlap with both the slow and fast Bloch modes. Whereas, in an asymmetric loaded square hole PC slab waveguide, the leaky TM-like PC slab modes are below the frequency band of the slow and fast modes. Therefore, TM-like PC slab modes have a significantly more adverse effect on the performance of circular hole based polarization rotator leading to a narrow band structure.

- SOI based PC membrane technology for THz application was developed. The PC slab waveguide and polarization rotators were fabricated employing this technology.
- An a-SiON PC slab waveguide structures were also fabricated at low temperature for optical applications. This technology has the potential to be implemented on any substrate or CMOS chips.

6.2 Future Work

We have found some areas worth more exploring in future.

- The origin of the difference between the square hole and circular hole PC slab can be studied using the electromagnetic scattering pattern of circular and rectangular cylinders. This study would provide physical insight into the geometry (hole shape) dependence of loss characteristics of PC slab waveguide based devices.
- By default, the common trend is to use a circular hole pattern for PC structures. The design investigations in this thesis showed that other hole geometries might result in better performances for certain applications. Having noted that, it could be possible to find the optimum hole geometry for wide band low loss applications. The work along this line of extension is worth exploring.
- As it was discussed in chapter 4, to couple two orthogonal polarizations to each other, a geometrical asymmetry must be imposed on the PC slab waveguide structure. In our proposed device, geometrical asymmetry was imposed on top of the defect line of a PC slab waveguide in the form of asymmetric loading. Other forms of geometrical asymmetries could be considered. For example, Zaccaria at el. studied symmetry reduced PCs [124]. They showed that by employing

symmetry reduced PCs the full bandgap for both TE and TM polarization could be achieved. This is a very interesting observation, for future PC based polarization rotator structures, the geometrical asymmetry could be introduced in the bulk PC instead of defect line. Heuristically speaking, loss characteristics might improve in the sense that geometrical asymmetry is applied to the bulk PC region where power density is low. Thus, the scattering loss at the junctions between alternating geometrical asymmetry will be minimized, as well as a reduced symmetry in PC own bandgap for both TE and TM polarizations. As a result, the TE/TM PC slab modes that detach energy from propagating modes can be eliminated, but the structure might not be as compact as our structure.

6.3 Characterization

The fabricated samples can be characterized in-house in the near future. Given the unique facilities at the University of Waterloo, the characterization setup for the PC slab waveguide and polarization rotators at frequency range of 200-500 GHz is under consideration at this time.

The measurements are carried out utilizing Agilent Millimeter-wave PNA-X network analyzer (up to 500 GHz). Standard waveguides are employed as the interface between coaxial cable and input/output tapers. The characteristics of standard metallic waveguides are presented in Table 6.1 [125]. For example, the central frequency of 400 GHz, WR-2 is utilized with size of $0.02" \times 0.01"$ (0.5mm × 0.25mm). The total thickness of the polarization rotator assuming that 400 GHz corresponds to a normalized frequency of $a/\lambda=0.265$ would be $0.008"$ (0.2 mm). A such, there could be a good match between the WR-2 and input taper. Figure 6.1 shows the sketch of the setup designed to couple electromagnetic wave in and out of the waveguide utilizing standard metallic waveguides. The input wave is TE10 that has been polarized along the y direction. The structural parameters of the waveguide are as follows: w=0.6a, t=0.8a, a=0.756 mm, $n_{si}=3.48$ and $\tan\delta=1\times10^{-4}$. The central frequency is set to 100 GHz corresponding to the normalized frequency of 0.252. This structure has been simulated by HFSS, v.11.

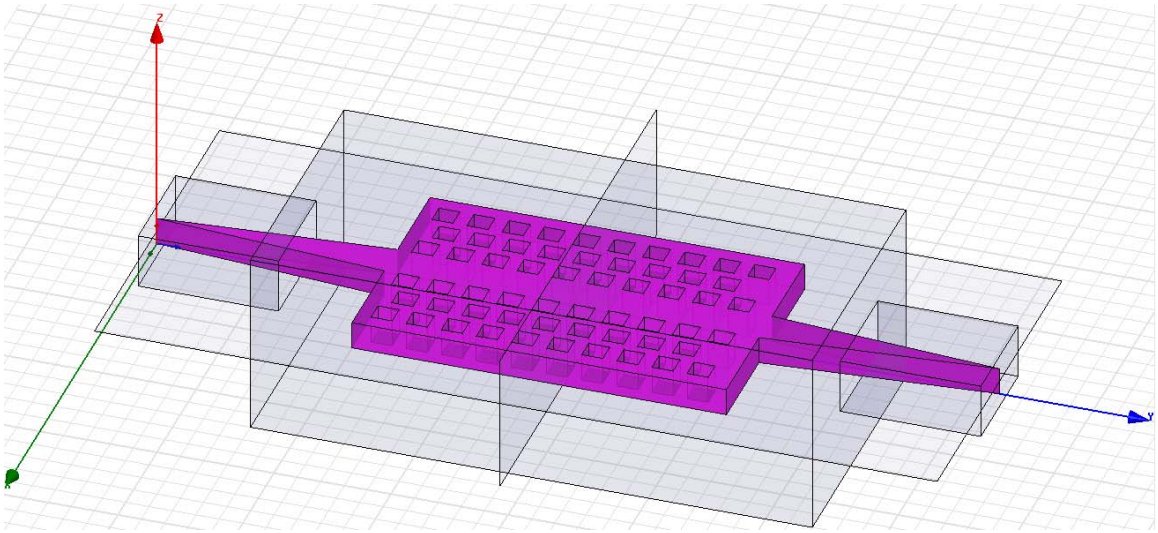

Figure 6.1 The schematic of the input metallic waveguide

Frequency Band	Waveguide Standard	Frequency Limits (GHz)	Inside Dimensions (inch)
W band	WR-10	75 to 110	0.100×0.050
F band	WR-8	90 to 140	0.080×0.040
D band	WR-6	110 to 170	0.065×0.0325
G band	WR-5	140 to 220	0.0510×0.0225
	WR-4	170 to 260	0.0430×0.0215
	WR-3	220 to 325	0.0340×0.0170
Y-band	WR-2	325 to 500	0.0200×0.0100
	WR-1.5	500 to 750	0.0150×0.0075
	WR-1	750 to 1100	0.0100×0.0050

Table 6.1Waveguide frequency bands and interior dimensions [126]

First, the structure shown in Figure 6.2(a) is simulated. It is a planar Si waveguide with no air holes. The electric field distribution at y=9 mm (y-propagation direction) and f=100 GHz is plotted in Figure 6.2 (b). The cross-section of the electric field distribution shows that the waveguide is multimode. The frequency response of the Si waveguide (Figure 6.2(a)) is plotted in Figure 6.2(c). It shows S_{11} and S_{21} versus frequency. The solid lines with circle symbol and no symbol graph S_{11} and S_{21}, respectively. At frequencies lower than 100 GHz, most of the input power has been reflected as S_{11} is stronger than S_{21}. At frequencies higher than 100 GHz, the transmitted power is more than reflected power, however, the difference is only few dB.

At the next step, the PC slab waveguide with a single defect line (Figure 6.1) is simulated. Figure 6.3(a) shows the cross-section of the electric field at 100 GHz and y=9 mm. The electric field is mostly confined in the defect line, meaning, the power transmission takes place through the defect line. The frequency response of the PC slab waveguide is plotted in Figure 6.3(b). S_{11} and S_{21} are depicted by solid line with circle symbol and plain solid line, respectively. The frequency response covers a wide range from 90 GHz to 110 GHz. The graphs show that the total transmission loss is less than 2 dB in the entire band and it becomes less than 1 dB around 100 GHz. These graphs suggest that the input and output coupling are efficient and the waveguide can be employed as a wide band low loss transmission line. The same set up can be utilized for the characterization of the polarization rotator structure. In fact, coupling losses at the input and output port can be extracted by loss measurement of several PC slab waveguide with different lengths. Thus, the coupling loss can be excluded from the propagation loss. The PC slab waveguide can be replaced with PC based polarization rotator to measure the polarization rotation efficiency.

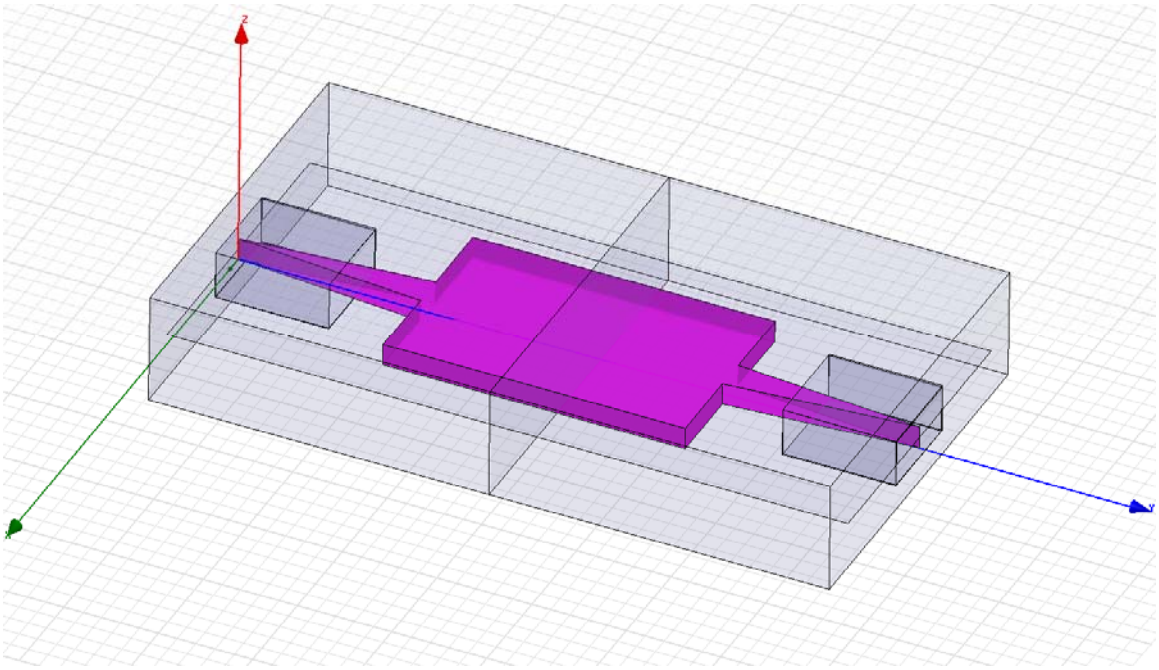

(a)

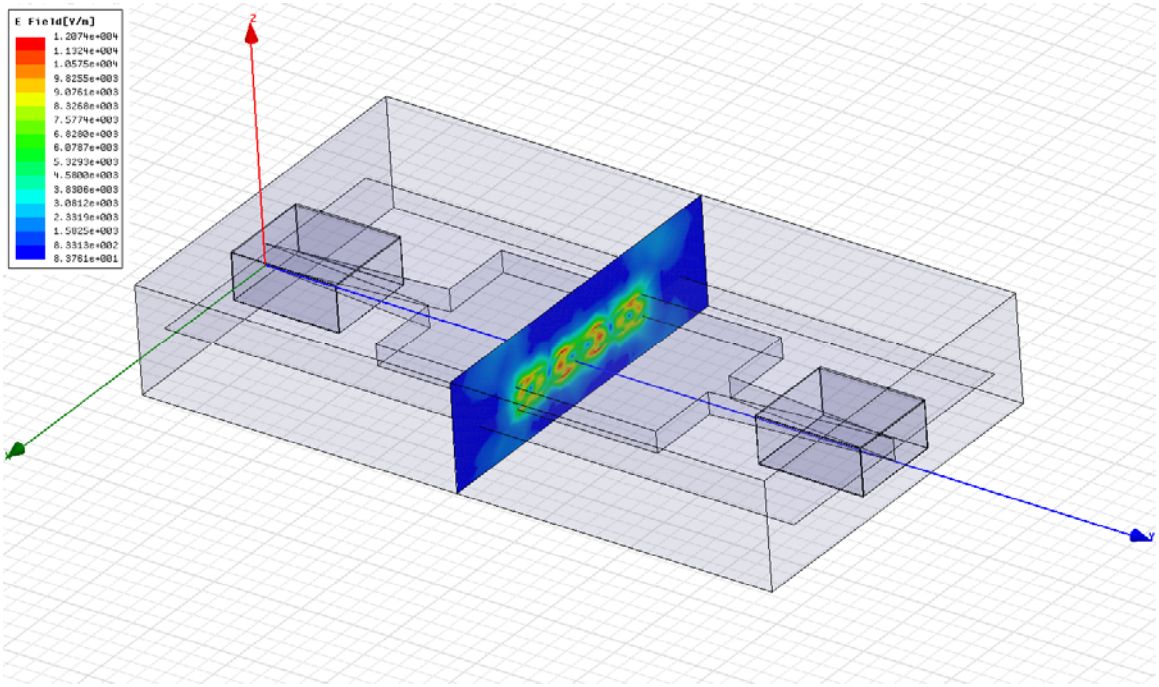
E Field[V/m]
1.2074e+004
1.1324e+004
1.0575e+004
9.8255e+003
9.0761e+003
8.3268e+003
7.5774e+003
6.8280e+003
6.0787e+003
5.3293e+003
4.5800e+003
3.8306e+003
3.0812e+003
2.3319e+003
1.5825e+003
8.3313e+002
8.3761e+001

(b)

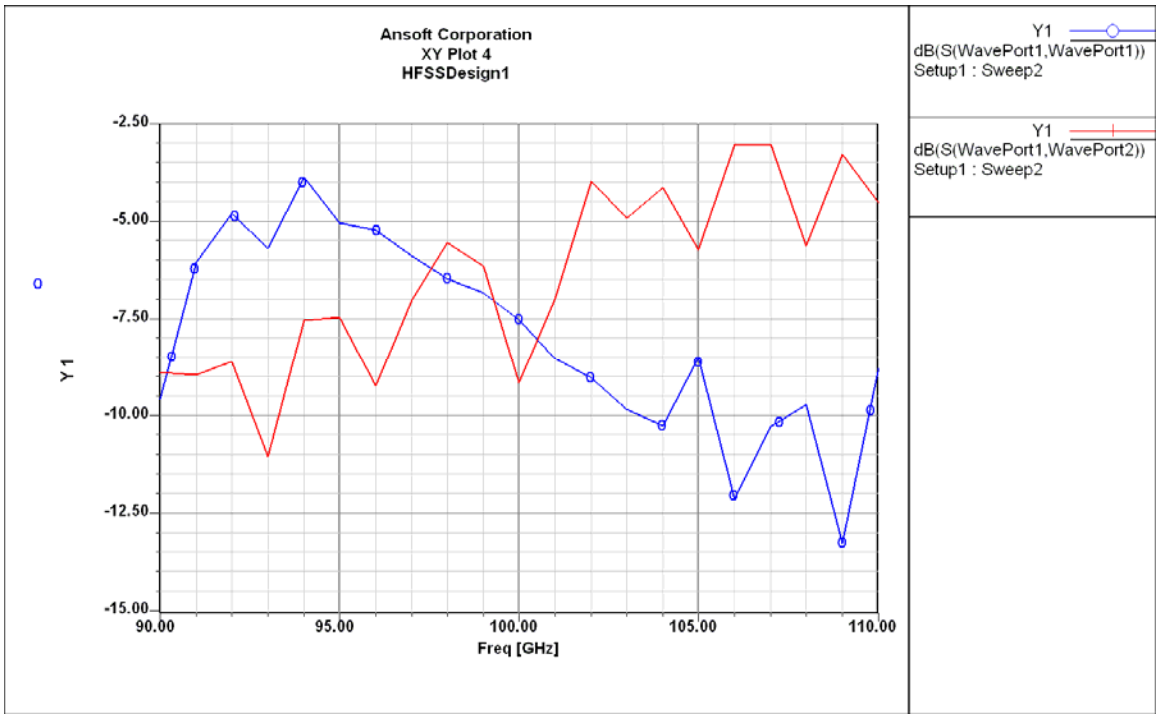

(c)

Figure 6.2 (a) the schematic of si waveguide with input and output tapers and WR waveguides for input/output coupling (b) cross-section of electric field at f=100 GHz and z=9mm (c) S_{11} (solid line with circles) and S_{21} (solid line) versus frequency.

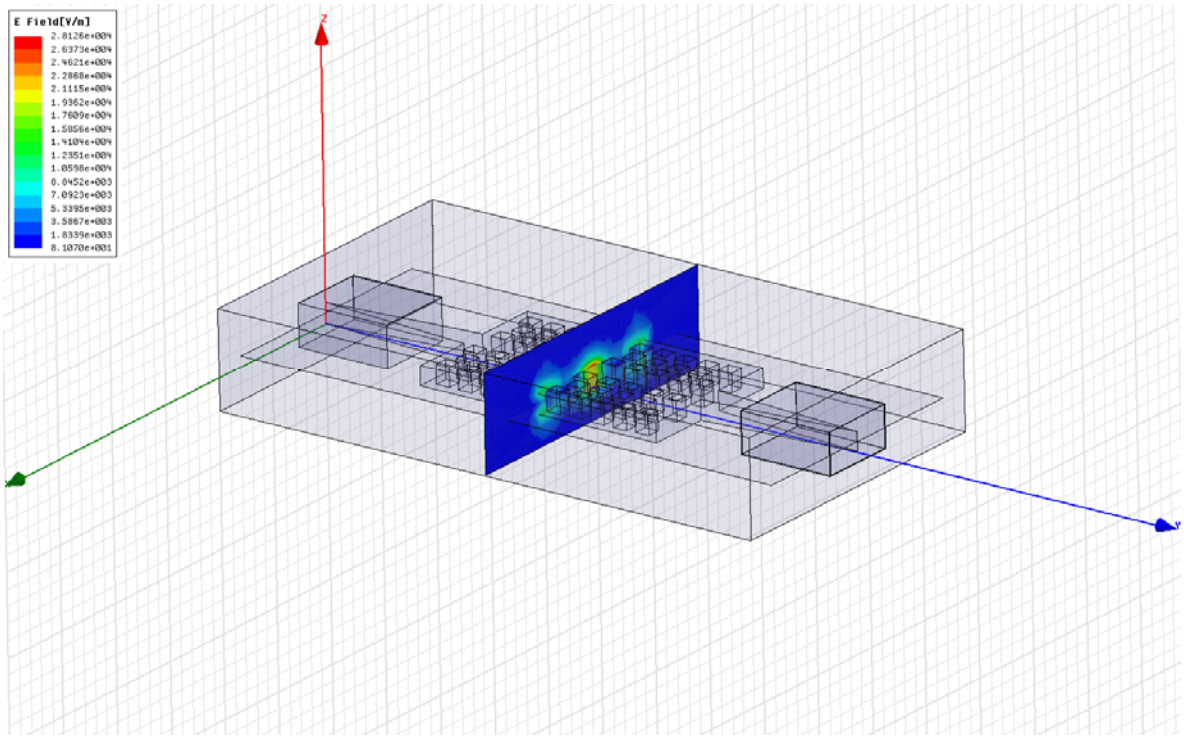

(a)

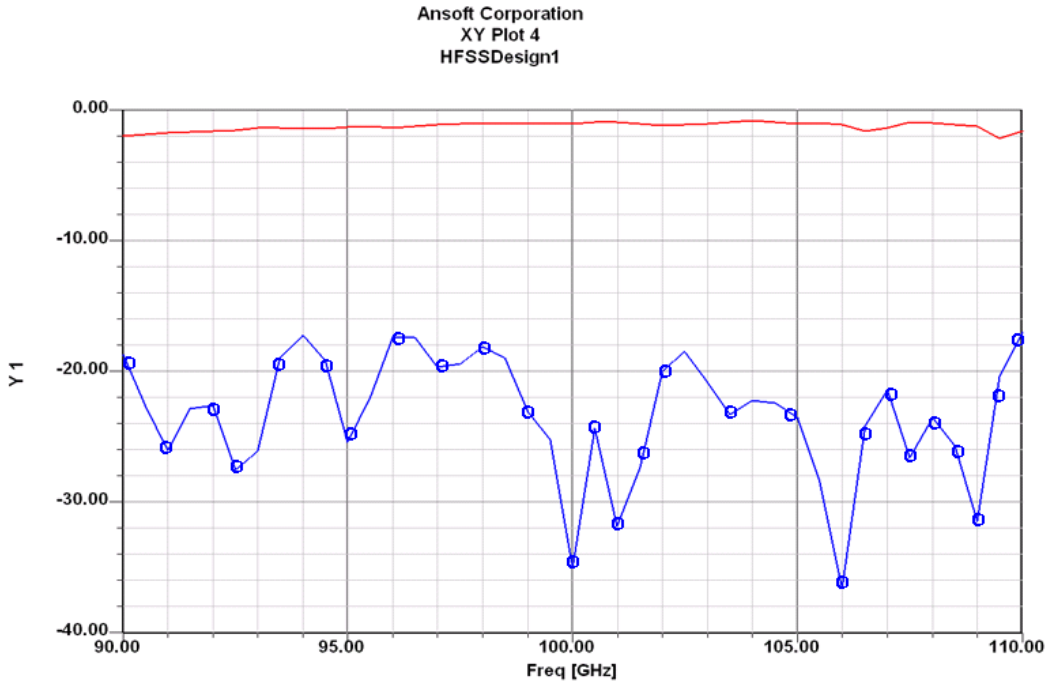

(b)

Figure 6.3 (a) The cross-section of electric field at y=9 mm at 100 GHz (b) S_{11} (solid line with circle symbols) and S_{21} (plain solid line) versus frequency, w=0.6a, t=0.8a, n_{si}=3.48, and tanδ=10^{-4}.

To exclude the coupling losses at the junctions and measure the intrinsic loss of Si, the propagation loss of several PC slab waveguide with different lengths can be measured. Scattering loss at the junctions of loaded layer is another source of propagation loss that must be taken into account. One simple way of measuring the scattering loss at the junctions is to compare the propagation loss of an asymmetric loaded PC slab waveguide with a simple PC slab waveguide with no loaded layer.

Polarization conversion efficiency is another important parameter to be measured. It is recommended to have two sets of polarization rotator structures with 90^o and 180^o rotation angel. Input of both structures is TE_{10} and the measured power at the output corresponds to TE_{10}, as well. Thus, having excluded coupling and scattering loss from junctions, the measured power at the output of 180^o polarizations rotators can be corresponded to TM wave at 90^o rotation. Having measured TE and TM wave at the output of 90^o polarization rotator structure, P.C.E. can be calculated using Equation (4.16).

In this thesis, PC based polarization controlling devices were designed and analyzed employing a rigorous numerical method, 3D-FDTD. A novel and compact PC based polarization rotator was designed and analyzed. The fabrication process of the proposed polarization rotator is compatible with planar integrated PC technology, which is one of the advantages of this device over geometrically asymmetric passive polarization rotators such as the slanted waveguide polarization rotator. Thus, this device can be integrated with other elements of the integrated circuit to control the polarization of the propagating wave. A SOI based process was developed to implement a PC based integrated on low loss SOI wafer for THz frequency application. Highly resistive silicon was used as the device layer of the SOI wafer to maintain low loss propagation for the THz wave. As such a low loss integrated waveguide can be implemented for a THz frequency band. Other elements can be integrated simply on the SOI wafer.

In final stage, the characterization setup was designed for in-house measurement. The devices are measured utilizing Agilent Millimeter-wave PNA-X network analyzed (up to 500 GHz). The input/output tapers are designed to provide with low loss coupling between input/output standard waveguide and PC slab waveguide (or other devices). The

preliminary rigorous numerical simulations of the setup are promising, and simulation results show that a low loss wideband guiding can be realized while employing a PC slab waveguide. The next step is to measure the samples, which will be accomplished in the near future.

Bibliography

[1] S. E. Miller, “Integrated Optics: an introduction”, Bell Syst. Tech. J., 48, 2059-2069, 1969.

[2] O. Wada, T. Sakurai, and T. Nakagami, “Recent progress in optoelectronic integrated circuits (OEICs),” IEEE J. Quant. Electron., QE-22, 805-823, 1986.

[3] T. L. Koch and U. Koren, “Semiconductor photonic integrated circuits,” IEEE J. Quntum Electron., QE-27, 641-653, 1991.

[4] R. Rubenstein “Photonic integration drives down the cost per bit,” Fibresystem magazine, Sep. 2008.

[5] R. Simes et al, “InP chip scale integration platform for high-performance tunable lasers,” Proc. SPIE Semiconductor Optoelectronic Devices for Lightwave Communication, Orlando, FL, Sept. 2003.

[6] R. Nagarajan et al., “Large scale photonic integrated circuits,” IEEE J. Selected Topics in Quantum Electronics, Vol. 11, No. 1, pp. 50-56, 2005

[7] R. Nagaragian et al. “400 Gbit DWDM photonic integrated circuits,” Electronics Letters, vol. 41, No. 6, 2005

[8] S. J. Spector, T. M. Lyszczarz, M. W. Geis, D. M. Lennon, J. U. Yoon, M. E. Grein, R. T. Schulein, R. Amataya, J. Birge, J. Chen, H. Byun, F. Gan, C. W. Holzwarth, J. L. Hoyt, E. P. Ippen, F. X. Kartner, A. Khilo, O. O. Olubuyide, J. S. Orcutt, M. Park, M. Perrott, M. A. Poppvic, T. Barwicz, M. Dahlem, R. J. Ram, H. I. Smith, “Integrated optical components in silicon for high speed analog-to-digital conversion,” Proceeding of SPIE, vol. 6477, pp. 64770O.1-64770O.14, 2007.

[9] H. Wong, V. Filip, C. K. Wong, P. S. Chung, “Silicon integrated photonics begins to revolutionize,” Microelectronics and reliability, vol. 47, No. 1, pp. 1-10 (2007).

[10] S. Selvarasah, R. Banyal, B. D. F. Casse, W. T. Lu, S. Sridher, and M. R. Dokmeci, “Design and implementation of silicon-based nanostructures for integrated photonic circuit applications using Deep Reactive Ion Etching (DRIE) technique,” Nanotech 2008:Micosystems, Photonics, sensors, Fluidics, Modeling, and Simulation-Technical Proceedings of the 2008 NSTI Nanotechnology Conference and Trade Show, Vol. 3, 54-57.

[11] J. P. Uyemura and B. L. Austin, “Hybrid optical-electronic logic gates in complementary metal-oxidesemiconductor very-large-scale integration,” Appl. Opt. vol. 31, No. 11, pp. 1772-1782, 1992.

[12] M. M. Ibrahim, “The gain-bandwidth of hybrid optical transistors,” IEEE J. Quantum Electronics, vol. 24, No. 11, 2227-2230 , 1988.

[13] W. R. Headley, G. T. Reed, S. Howe, A. Liu, and M, Paniccia, “Polarization-independent optical racetrack resonators using rib waveguides on silicon-on-insulator,” Appl. Phys. Lett. 85, 5523–5525, 2004.

[14] D. –X. Xu, S. Janz, and P. Cheben, “Design of polarization-insensitive ring resonators in silicon-on-insulator using MMI couplers and cladding stress engineering,” IEEE Photon. Technol. Lett. 18, 343–345, 2006.

[15] C. H. Kwan, and K. S. Chiang, “Study of polarization-dependent coupling in optical waveguide directional couplers by the effective-index method with built-in perturbation correction,” J. Lightwave Technol. 20, 1018–1026, 2002.

[16] T. Barwicz, M. R. Watts, M. A. Popovic, P. T. Rakich, L. Socci, F. X. Kärtner, E. P. Ippen and H. I. Smith, “Polarization-transparent microphotonic devices in the strong confinement limit,” Nature Photonics 1, 57 – 60, 2006.

[17] M. R. Watts, and H. A. Haus, “Integrated mode-evolution-based polarization rotators,” Opt. Lett. 30, 138–140, 2005.

[19] J. Cai, J. Jiang, and G. P. Nordin, “Ultra-short waveguide polarization converter using a sub-wavelength grating,” in Integrated Photonics Research Topical Meetings (The Optical Society of America, Washington, DC, 2004).

[20] H. El-Rafaei, D. Yevick, and T. Jones, “Slanted-rib wavgeuide InGaAsP-InP plarization converters,” IEEE J. Lightwave Technol. 22, pp. 1352-1357, 2004.

[21] M. V. Kotlyar, L. Bolla, M. Midrio, L. O Faolain, and F. Thomas, “Compact polarization converter in InP-based material,” Optics Express, vol. 13, no. 13, pp. 5040-5045, 2005.

[22] M. Loncar, D. Nedeljkovic, T. Doll, J. Vuckovic, and A. Scherer, “Waveguiding in planar photonic crystals,” Appl. Phys. Lett. 77, No. 13, 1937-1939, 2000.

[23] M. ar, T. Doll, J. Kovi, and A. Scherer, "Design and fabrication of silicon photonic crystal optical waveguides," IEEE J. Lightwave Technol. 18, No. 10, 1402.

[24] T. Zijlstra, E. van der Drift, M. J. A. de Dood, E. Snoeks, and A. Polman, "Fabrication of two-dimensional photonic crystal waveguides for 1.5 um in silicon by deep anisotropic dry etching,"J. Vac. Sci. Technol. B, vol. 15, No. 6, 2734-2739, 1999.

[25] S. McNab, N. Moll, and Y. Vlasov, "Ultra-low loss photonic integrated circuit with membrane-type photonic crystal waveguides," Optics Express, vol. 11, No. 22, 2927-2939, 2003.

[26] W. Bogaerts, R. Baets, P. Dumon, at el., "Nanophotonic waveguides in silicon-on-insulator fabricated with CMOS technology," J. of Lightw. Technol. 23, 401-421 (2005).

[27] B. Jalali, S. Yegnanarayanan, T. Yoon, T. Yoshimoto, I. Rendina, and F. Coppinger," Advances in silicon-on-insulator optoelectronics," IEEE J. of Sel. Topics in Electron. 4, 938-947, 1998.

[28] W. Bogaerts, D. Taillaert, B. Luyssaert, P. Dumon, at. al., "Basic structures for photonic integrated circuits in Silicon-on-insulator," Opt. Express 12, 1583-1591, 2004.

[29] M. Zelsmann, E. Picard, T. Charvolin, and E. Hadji, "Broadband optical characterization and modeling of photonic crystal waveguides for silicon optical interconnects," J. of Appl. Phys. 95, 1606-1608, 2004.

[30] C. Manolatou, S. G. Johnson, S. Fan, P. R. Villeneuve, H. A. Haus, and J. D. Joannopoulos, "High-density integrated optics," J. Lightwave Technol. 17, 1682-1692, 1992.

[31] D. Sadot, and E. Boimovich, "Tunable optical filters for WDM applications," IEEE Commun. Mag. 36, 50-55, 1998.

[32] Pavesi, L. & Lockwood, D. J. *Silicon Photonics* (Springer, New York, 2004).

[33] J. Dai, J. Zhang, W. Zhang, and D. Grischkowsky, "Terahertz time-domain spectroscopy characterization of the far-infrared absorption and index of refraction of high-resistivity, float-zone silicon," J. Opt. Soc. Am. B., vol. 21, No. 7, 1379-1386, 2004.

[34] P. H. Siegel, “Terahertz technology,” IEEE Transactions on microwave theory and techniques 50, 910-928, 2002.

[35] T. Baras, “On-chip detection of biomaterials: a numerical study,” J. Biol. Phys. 29, 187-194, 2003.

[36] R. Kohler, “High-performance continues-wave operation of superlattice terahertz quantum-cascade laser,” Appl. Phys. Lett. 82, 1518-1520, 2003.

[37] C. Lin, C. Chen, G. J. Schneider, P. Yao, S. Shi, A. Sharkawy, and D. W. Prather, “Wavelength scale terahertz two-dimensional photonic crystal waveguides,” Optics Express, vol. 12, no. 23, 5723-5728, 2004.

[38] E. Yablonovitch, “Photonic band-gap structures,” J. Opt. Soc. Am. B 10, 283-295, 1993.

[39] S. Y. Lin, J.G. Fleming, D. L. Hetherington, B. K. Smith, R. Biswas, K. M. Ho, M. M. Sigalas, W. Zubrzycki, S. R. Kurtz, and J. Bur, “A three-dimensional photonic crystal operating at infrared wavelengths,” Nature, vol. 394, 251-253, 1998.

[40] S. Fan, P. R. Villeneuve, R. D. Meade, and J. D. Joannopoulos, “Design of a three-dimensional crystals at submicron lengthscales,” Appl. Phys. Lett. 65 (11), 1466-1468, 1994.

[41] O. Hanaizumi, Y. Ohtera, T. Sato, and S. Kawakami, “Propagation of light beams along defects formed in a-Si/SiO2 three-dimensional photonic crystals: Fabrication and observation,” Appl. Phys. Lett. 74, no. 6, 777-779, 1999.

[42] M. Qi, E. Lidorilis, P. T. Rakich, S. G. Johnson, J. D. Joannopoulos, E. P. Ippen, and H. I. Smith, “A three-dimensional optical photonic crystal with designed point defects,” Letters to Nature, Nature 429, 538-542, 2004.

[43] I. Divliansky, and T. S. Mayer, “Fabrication of three-dimensional polymer photonic crystal structures using single diffraction element interference lithography”, Appl. Phys. Lett. 82, no. 11, 1667-1669, 2003.

[44] Ch. C. Cheng, and A. Scherer, “New fabrication techniques for high quality photonic crystals”, J. Vac. Sci. Technol. B 15, no. 6, 2764-2767, 1997.

[45] K. Sakoda, *Optical properties of Photonic crystal,* Springer, 2004.

[46] Sh. Guo and S. Albin, “Simple plane wave implementation for photonic crystal calculations”, Optics Express, vol. 11, no. 2, 167-175, 2003.

[47] L. C. Andreani and M. Agio, "Photonic bands and Gaps maps in a photonic crystal slab", IEEE J. of Quantum Elec. 38, no. 7, 891-898, 2002.

[48] J. D Joannopoulos, R D Meade, and J N Winn, *Molding the Flow of Light*, Princeton University Press, 1990.

[49] S. G. Johnson, S. Fan, P. R. Villeneuve, and J. D. Joannopoulos, "Guided modes in photonic crystal slabs", Phys. Rev. B 60, no. 8, 5751-5758, 1999.

[50] S. S. Xiao, L. F. Shen, and S. L. He, "A plane-wave expansion method based on the effective medium theory for calculating the band structure of a two-dimensional photonic crystal," Phys. Lett. A 313, pp.132-138, 2003.

[51] S. Shi, C. Chen, D. W. Prather, "Plane-wave expansion method for calculating band structure of photonic crystal slabs with perfectly matched layers," J. Opt. Soc. Am. A 21, no. 9, 1769-1775, 2004.

[52] S. S. A. Obyya, "Efficient finite-element-based time-domain beam propagation analysis of optical integrated circuits," IEEE J. Quantum Electron. 40, no. 5, 591-595, 2004.

[53] J. G. Maloney and M. P. Kesler, "Analysis of Periodic Structures" Chap. 6 in *Advances in Computational Electrodynamics: The Finite-Difference Time-Domain Method,* A. Taflove, ed., Artech House, publishers, 1998.

[54] A. Taflove and S. C. Hagness, *Computational Electrodynamics, the Finite-Difference Time-Domain Method*, 2nd ed. Norwood, MA, Artech House, 2000.

[55] K. Yee, "Numerical solution of initial boundary value problems involving Maxwell's equations in isotropic media," Antennas and Propagation, IEEE Transactions on 14, pp. 302-307, 1966.

[56] S.T. Chu, and S. K. Chaudhuri, "A finite-difference time-domain method for the design and analysis of guided-wave optical structures," J. Lightwave technol. 7, no. 12, pp. 2028-2033, 1989.

[57] I. El-Kady, "Dielectric waveguides in two-dimensional photonic bandgap materials", M J. Lightwave Technol. 17, no. 11, pp. 2042-2049, 1999.

[58] M. Loncar, *Nanophotonic devices based on planar photonic crystals*, PHD Thesis, California Institute of Technology, Pasadena, California, 2003.

[59] A. Chutinan, S. Noda, "Waveguides and waveguide bends in two-dimensional photonic crystal slabs" Phys. Rev. B, vol. 62, no. 7, pp. 4488-4492, 2000.

[60] M. Lončar, J. Vuckovic and A. Scherer, "Methods for controlling positions of guided modes of photonic-crystal waveguides", JOSA B 18, vol. 9, pp. 1362-1368, 2001.

[61] T. Baba, A. Motegi, T. Iwai, N. Fukaya, Y. Watanabe, and A. Sakai, " Light propagation characteristics of straight single-line-defect waveguides in photonic crystal slabs fabricated into a silicon-on-insulator substrate", IEEE J. of Quantum Elec. 38, no. 2, pp. 743-752, 2002.

[62] A. Adibi, Y. Xu, R. K. Lee, M. Loncar, A. Yariv, and A. Scherer, "Role of distributed Bragg reflection in photonic-crystal optical waveguides", Phys. Rev. B., 64, no. 4, pp. 1102, 2001.

[63] J. Arentoft, T. Sondergaard, M. Kristensen, A. Boltasseva, M. Thourhauge and L. Frandsen, "Low-loss silicon-on-insulator photonic crystal waveguides", Electronics Letters, vol. 38, no. 6, pp. 274-275, 2002.

[64] H. Benisty , D. Labilloy, C. Weisbuch, and etc., "Radiation losses of waveguide-based two-dimensional photonic crystals: Positive role of the substrate", Appl. Phys. Lett. 76, no. 5, pp. 532-534, 2000.

[65] S. Foteinopoulo, A. Rosenberg, M M Sigalas and C M Soukoulis, " In and out-of-plane propagation of electromagnetic waves in low index contrast two dimensional photonic crystal", J. Appl. Phys. 89, no.2, pp. 824-830, 2001.

[66] D. R. Solli, and J. M. Hickmann, "Photonic crystal based polarization control devices", J. Appl. Phys. 37, R263, 2004.

[67] L. M. Li, "Two dimensional photonic crystals: candidate for wave plates" Appl. Phys. Lett. 78, no. 22, pp. 3400-3402, 2001.

[68] D. R. Solli, C. F. McCormick, and R. Y. Chiao, "Photonic crystal polarizers and polarizing beam splitters", J. of Appl. Phys. 93, no. 12, pp. 9429-9431, 2003.

[69] T. Liu, A. R. Zakharian, M. Fallahi, J. V. Moloney, and M. Mansuripur, "Design of a compact photonic-crystal-based polarizing beam splitter" IEEE Photon. Technol. Lett. 17, no. 7, pp. 1435-1437, 2005.

[70] J. M. Hickmann, D. soli , at et., "Microwave measurements of the photonic band gap in a two-dimensional photonic crystal slab", J. Appl. Phys. 92, no. 11, pp. 6918-6920, 2002.

[71] F. Genereux, S. W. Leonard, and H. M. van Driel, "Large birefringence in two-dimensional photonic crystals", Phys. Rev. B 63, 161101, 2001.

[72] D. R. Soli, C. F. McCormick, R. Y. Chiao, and J. M. Hickmann, "Birefrengence in two-dimensional bulk photonic crystals applied to the construction of quarter waveplates", OPTICS EXPRESS, vol.11, no.2, pp. 125-133, 2003.

[73] Y. Shani, R. Alferness, T. Koch, U. Koren, M. Oron, B. I. Miller, and M. G. Young, "Polarization rotation in asymmetric periodic loaded rib waveguides," Appl. Phys. Lett. 59, pp. 1278-1280, 1991.

[74] H. Heidrich, P. Albrecht, M. Hamacherm, H. P. Nolting, H. Schroeter, and C. M. Weinert, "Passive mode converter with a periodically tilted InP/GaInAsP rib waveguide," IEEE Photon. Technol. Lett., vol. 4, no. 1, pp. 34-36 (1992).

[75] K. Mertens, B. Scholl, and H. J. Schmitt, "Strong polarization conversion in periodically loaded strip waveguide," IEEE Photon. Technol. Lett. 10, pp. 1133-1135, 1998.

[76] C. Van Dam, L. H. Spickman, F. P. G. M. Van Ham, F. H. Groen, J. J. G. M. van der Tol, I. Moerman, W. W. Pascher, M. Hamacher, H. Heidrich, C. M. Weinert, and M. K. Smit, "Novel compact polarization converters based on ultra short bend," IEEE Photon. Technol. 8, no. 10, pp. 1346-1348, 1996.

[77] W. W. Lui, K. Magari, N. Yoshimoto, S. Oku, T. Hirono, K. Yokoyama, and W. P. Huang, "Modeling and design of bending waveguide based semiconductor polarization rotators," IEEE Photon Technol. Lett. 9, no. 10, pp. 1379-1381, 1997.

[78] W. W. Lui, C. L. Xu, T. Hirono, K. Yokoyama, and W. P. Huang, "Full-vectorial wave propagation in semiconductor optical bending waveguides and equivalent straight waveguides," IEEE J. Lightwave Technol.16, no. 5, pp. 910-914, 1998.

[79] W. W. Lui, T. Hirono, K. Yokomaya, and W. P. Huang, "Polarization rotator in semiconductor bending waveguides: A coupled-mode theory formulation," IEEE J. Lightwave Technol. 16, no. 5, pp. 929-936, 1998.

[80] W. Huang and Z. M. Mao, "Polarization rotation in periodic loaded rib waveguides," IEEE J. Lightwave Technol. 10, 1825-1831, 1992.

[81]S. S. A. Obayya, B. M. A. Rahman, and H. A. El-Mikati, "Vector beam propagation analysis of polarization conversion in periodically loaded waveguides," IEEE Photon. Technol. Lett. 12, 1346-1348, 2000.

[82] V. P. Tzolov, and M. Fontaine "A passive polarization converter free of longitudinally-periodic structures," Optics Communications, vol. 27, pp. 7-13, 1996.

[83] J. Z. Huang, R. Scarmozzino, G. Nagy, M. J. Steel, and R. M. Osgood, Jr., "Realization of a compact and single-mode optical passive polarization conveter," IEEE Photon. Technol. Lett. 12, no. 3, pp. 317-319, 2000.

[84] B. M. A. Rahman, S. S. A. Obayya, N. Somasiri, M. Rajarajan, K. T. V. Grattan, and H. A. El-Mikathi, " Design and characterization of compact single-section passive polarization rotator," IEEE J. Lightwave Technol. 19, no. 4, pp. 512-519 , 2001.

[85] H. El-Refaei and D. Yevick, "An optimized InGaAsP/InP polarization converter employing asymmetric rib waveguides," IEEE J. Lightwave Technol. 21, no. 6, pp. 1544-1548, 2003.

[86] P. S. Chan, H. K. Tsang, and C. Shu, "Mode conversion and birefringence adjustment by focused-ion-beam etching for slanted rib waveguide walls," Opt. Lett. 28, no. 21, pp. 2109-2111, 2003.

[87] H. Deng, "Design and characterization of silicon-on-insulator passive polarization converter with finite-element analysis," Ph.D Thesis, University of Waterloo, 2005.

[88] Z. Wang, D. Dai, "Ultrasmall Si-nanowire-based polarization rotator," J. Opt. Soc. Am. B, vol. 25, no. 5, pp. 747-753, 2008.

[89] M. Mrozowski, Guided electromagnetic waves: properties and analysis, England: Research Studies Press Ltd./ John Wiley & Sons Inc., 1997.

[90] A. W. Snyder and J. D. Love, Optical Waveguide Theory, London: Chapman & Hall, 1983.

[91] O. Painter, J. Vuckovic, and A. Scherer, "Defect modes of a two-dimensional photonic crystal in an optically thin dielectric slab," Vol. 16, no. 2, pp. 275-285, 1999.

[92] T. Baba, N. Fukaya, and J. Yonekura, "Observation of light propagation in pghotonic crystal waveguides with bends," Electronics Letter, vol. 35, no. 8, pp. 654-655, 1999.

[93] M. R. Watts, H. A. Haus, and E. P. Ippen, "Integrated mode-evolution-based polarization splitter," Opt. Lett. 30, pp. 967–969.

[94] Y. Cui, Q. Wu, E. Schonbrun, M. Tinker, J. B. Lee, and W. Park, "Silicon-based 2-D slab photonic crystal TM polarizer at telecommunication wavelength," IEEE Photon. Technol. Lett. 20, no. 8, pp. 641-643.

[95] H. Benisty, C. Weisbuch, at el, "Optical and confinement properties of two-dimensional photonic crystal", J. Lightwave Technol. 17, pp. 2063, 1999.

[96] T. Tamir, *Integrated Optics*, Berlin: Springer-Verlag, 1975.

[97] K. Bayat, S. K. Chaudhuri, S. Safavi-Naeini, "Polarization and thickness dependent guiding in the photonic crystal slab waveguide," Opt. Express, vol. 15, pp. 8391-8400, 2007.

[98] A. Jafarpour, Ch. M. Reinke, A. Adibi, Y. Xu, and R. K. Lee, "A new method for the calculation of the dispersion of nonperiodic photonic crystal waveguides", IEEE J. of Quantum Electron. 40, no. 8, pp. 1060-1067, 2004.

[99] T. Baba, "Slow light in photonic crystals," Nature Photonics 2, pp. 465-473, 2008.

[100] Y. A. Vlasov, M. O'Boyle, H. F. Hamann, and S. J. McNab, "Active control of slow light on a chip with photonic crystal waveguides," Nature 438, pp. 65-69, 2005.

[101] T. Baba, T. Kawasaki, H. Sasaki, J. Adachi, and D. Mori, "Large delay-bandwidth product and delay tunning of slow light pulse in photonic crystal coupled waveguide," Opt. Express, vol. 16, pp. 9245-9253, 2008.

[102] M. Soljacic, and J. D. Joannopoulos, "Enhancement of nonlinear effects using photonic crystals," Nature Mater, vol. 3, pp. 211-219, 2004.

[103] M. Soljacic et al. "Nonlinear photonic crystal microdevices for optical integration," Opt. Lett. 28, pp. 637-639, 2003.

[104] J. B. Khurgin, "Adiabatically tunable optical delay lines and their performance limitations," Opt. Lett. 30, pp. 2778-2780, 2005.

[105] Q. Xu, P. Dong, and M. Lipson, "Breaking the delay-bandwidth limit in a photonic structure," Nature Phys., vol. 3, pp. 406-410, 2007.

[106] J. P. Hugonin, P. Lalanne, T. P. White, and T. F. Krauss, "Coupling into slow-mode photonic crystal waveguides," Opt. Lett. 32, no. 18, pp. 2638-2640, 2007.

[107] P. Pottier, M. Gnan, and R. M. De La Rue, "Efficient coupling into slow-light photonic crystal channel guides using photonic crystal tapers," Opt. Express, vol. 15, no. 11, pp. 6569-6575, 2007.

[108] P. Velha, J. P. Hugonin, and P. Lalanne, "Compact and efficient injection of light into band-edge slow-modes," Opt. Express, vol. 15, no. 10, pp. 6102-6112, 2007.

[109] S. Khorasani, *An introduction to optics of photonic crystals*, In Persian, Sharif University of Technology, 2006.

[110] J. H. Wu, A. Q. Liu, L. K. Ang, and T. H. Cheng, "Complex photonic band diagrams for finite-size photonic crystals with arbitrary defects," J. Appl. Phys. 101, pp. 053101(1-8), 2007.

[111] W. P. Haung, S. T. Chu, and S. K. chaudhuri, "Scalar coupled-mode theory with vector correction," IEEE J. Quantum Electron. 28, 184-193, 1992.

[112] S. Olivier, H. Benisty, C. Weisbuch, C. J. M. Smith, T. F. Krauss, and R. Houdre, "Coupled-mode theory and propagation losses in photonic crystal waveguides," Optics Express, vol. 11, no. 13, pp. 1490-1496, 2003.

[113] G. –L. Bona, R. Germann, and B. J. Offrein, "SiON high-refractive-index waveguide and planar lightwave circuits," IBM Journal of Research and Development, vol. 47, no. 2/3, 2003.

[114] R. Germann, H. W. M. Salemink, R. Beyeler, G. L. Bona, F. Horst, I. Massarek, and B. J. Offrein, "Silicon oxinitride layers for optical waveguide applications," *J. Electrochem. Society,* vol. 147, no. 6, pp. 2237-2241, 2000.

[115] M. A. McCord, M. J. Rooks, "2", SPIE Handbook of Microlithography, Micromachining and Microfabrication, 2002.

[116] J. H. Liebe, G. A. Hufford, and M. G. Cotton, "Propagation modeling of moist air and suspended wafer/ice particles at frequencies below 1000 GHz," In AGARD, Atmospheric Propagation Effects Through Natural and Man-Made Obscurants for Visible to MM-Wave Radiation (N94-30495 08-32).

[117] G. Gallot, S. P. Jaminson, R. W. McGowan, and D. Grischkowsky, J. Opt. Soc. Am. B, vol. 17, pp. 851, 2000.

[118] J. A. Harrington, R. George, and P. Pedersen, "Hollow polycarbonate waveguides with inner Cu coatings for delivery of terahertz radiation," Opt. Express, vol. 12, no. 21, pp. 5263-5268, 2004.

[119] T. Ito, Y. Matsuura, M, Miyagi, H. Minamide, and H. Ito, "Flexible terahertz fiber optics with low bend-induced losses," J. Opt. Soc. Am. B 24, no. 5, pp. 1230-1235, 2007.

[120] E. Perret, N. Zerounian, S. David, F. Aniel, "Complex permittivity characterization of benzocyclobutene for terahertz applications," Microelectronic engineering, vol. 85, No. 11, pp. 2276-2281, 2008.

[121] N. Jukam and M. S. Sherwin, "Two-dimensional terahertz photonic crystals fabricated by deep reactive ion etching in Si," Appl. Phys. Lett. 83, No. 1, pp. 21-23, 2003.

[122] Y. Zhao, and D. R. Grischkowsky, "2-D terahertz metallic photonic crystals in parallel-plate waveguides," IEEE Trans. On Microwave and Technol, vol. 55, no. 4, pp. 656-663 (2007).

[123] S. G. Johnson, P. Bienstman, M. A. Skorobogati, M. Ibanescu, E. Lidorikis, and J. D. Joannopoulos, "Adiabatic theorem and continuous coupled-mode theory for efficient taper transitions in photonic crystals," Phys. Rev. E **66**, 066608 (2002).

[124] M. Palamaru, and Ph. Lalanne, "Photonic crystal waveguides: out-of-plane losses and adiabatic modal conversion," Appl. Phys. Lett. 78, no. 11, pp. 1466-1468, 2001.

[125] R. P. Zaccaria, P. Verma, S. Kawaguchi, S. Shoji, and S. Kawata, "Manipulating full photonic band gap in two dimensional birefringent photnic crystals," Optics Express, vol. 16, no. 19, 14812-14820 (2008)

[126] http://www.microwaves101.com/encyclopedia/waveguidedimensions.cfm